ANL-HEP-TR-01-035

X-BAND DIELECTRIC LOADED RF DRIVEN ACCELERATOR STRUCTURES:

THEORETICAL AND EXPERTIMENTAL INVESTIGATIONS

BY

PENG ZOU

Submitted in partial fulfillment of the
requirements for the degree of
Doctor of Philosophy in Electrical Engineering
in the Graduate College of the
Illinois Institute of Technology

Approved _____
Adviser

Chicago, Illinois
July 2001

ACKNOWLEDGEMENT

I am greatly honored to write this dissertation as a tribute to the great efforts many people have devoted to the research program, X-Band Dielectric Loaded Accelerator Structures. I could not have accomplished this dissertation without the help of many friends, colleagues and my family.

I wish to thank the teachers who helped shape my scientific perspective and research style. My advisor, Professor Thomas Wong, introduced me into the area of electromagnetics, and has been a mentor for me for all these years. I am deeply grateful to Dr. Wei Gai, the leader of this research program in Argonne National Laboratory, for his inspiring guidance and strong encouragement when I am carrying out the research in his group. It has been a pleasure to work with all the people of the accelerator R&D group. I have been receiving the expert support from Dr. Liling Xiao and Dr. Xiang Sun. I also have to express my gratitude to Dr. Manuel Conde, Dr. John Power, Dr. Paul Schoessow, and Mr. Richard Konecny for their active involvement into this program. This research program is supported by US Department of Energy, High Energy Physics Division, Advanced Technology Branch, under the contract No. W-31-109-ENG-38, and is conducted at the Accelerator R&D Group of High Energy Physics Division of Argonne National Laboratory.

This dissertation is dedicated to my parents and my wife. I feel deeply indebted to their consistent support that walked me through this journey. Finally, my endless love goes to my wife, Jing.

TABLE OF CONTENTS

LIST OF TABLES

LIST OF FIGURES

LIST OF SYMBOLS

Symbol	Definition
a_0	field attenuation parameter per unit length in the traveling-wave accelerator
b_n	phase constant of the space harmonic of index n in the periodic structure
e	permittivity of material; dielectric constant of material
e_0	permittivity of free space
e_r	relative permittivity, dielectric constant
f	phase
l	wavelength
t_0	total power attenuation parameter of the traveling-wave accelerator
w	angular frequency
s	conductivity
m	permeability of material
m_0	permeability of free space
DW	energy gain of a given charged particle in accelerator
a	inner radius of dielectric-lined circular waveguide; iris radius of iris-loaded periodic structure; iris radius of hybrid dielectric-iris-loaded periodic structure
a_n	amplitude of the space harmonic of index n

Symbol	Definition
b	outer radius of dielectric-lined circular waveguide; iris radius of iris-loaded periodic structure; iris radius of hybrid dielectric-iris-loaded periodic structure
c	speed of light in the free space
k_0	wave number of TEM wave in free space
k_1	cutoff wave number of waveguide mode in the vacuum region of the dielectric-lined circular waveguide
k_2	cutoff wave number of waveguide mode in the dielectric region of the dielectric-lined circular waveguide
k_z	propagation constant of RF wave, phase constant
l	length
q	charge
r	location in r-direction in cylindrical coordinates; shunt impedance per unit length in traveling-wave accelerator
r_s	shunt impedance of a standing-wave accelerator
$r¢$	effective shunt impedance of a standing-wave accelerator
t	time
tand_l	loss tangent of dielectric
v_g	group velocity of RF wave
v_p	phase velocity of RF wave
z	location in z-direction in cylindrical coordinates; location along wave propagation
E	electric field magnitude

Symbol	Definition
E_0	acceleration gradient at the entrance of a traveling-wave accelerator
E_a	peak axial longitudinal electric field amplitude, accelerating field amplitude, acceleration gradient
E_s	peak surface electric field amplitude
$\vec{E}_t$	transverse electric field
E_z	longitudinal electric field magnitude
$\vec{E}_z$	longitudinal electric field
$E_{z,SW}$	longitudinal electric field in the standing-wave accelerator
$E_{z,TW}$	longitudinal electric field in the traveling-wave accelerator
H	magnetic field magnitude
H_z	longitudinal magnetic field intensity
$\vec{H}_z$	longitudinal magnetic field
$\vec{H}_t$	transverse magnetic field
P_0	input power
$P_{dielectric}$	power dissipation in the dielectric
P_{diss}	power dissipation in the structure
P_w	power flow in the traveling-wave structure
P_{wall}	power dissipation in the conducting wall, Ohmic loss
Q	quality factor

Symbol	Definition
R_s	surface resistivity
T	transit time factor
U	time average stored energy per unit length
V	volume
Z	shunt impedance per unit length of a standing-wave accelerator
ZT^2	effective shunt impedance per unit length of a standing-wave accelerator

CHAPTER I

INTRODUCTION

The current worldwide efforts in research and development of particle accelerators concentrate on seeking an affordable high-gradient accelerator technology for the future supercolliders [1]*. It has been recognized for some time that dielectric loaded accelerating structures are attractive candidates for the next generation of very-high-energy accelerators, because they possess several distinct advantages over conventional metallic iris-loaded accelerating structures. This thesis reports the research results of two classes of dielectric-loaded accelerating structures. One is based on a dielectric-lined circular waveguide, and the other is a novel hybrid dielectric-iris-loaded structure. For better explanation of background of such research programs, it is important to briefly visit some basics of accelerator technology and the history of particle accelerators.

1.1 Accelerator Basics

A particle accelerator delivers energy to a charged-particle beam by the application of an electric field. The early particle accelerators were electrostatic accelerators in which the beam gains energy from a constant electric field. Each particle acquires an energy equal to the product of its electric charge times the potential drop across the accelerating channel. A major limitation of electrostatic accelerators is that the maximum energy obtainable cannot exceed the product of the charge times the potential difference that can be maintained, and in practice this potential difference is limited by electric breakdown to no more than a few tens of megavolts. The accelerators using radio-frequency (RF) electromagnetic wave bypass this limitation by applying a harmonic time-varying electric field to the beam,

---

* Corresponding to references in the Bibliography

which is localized into bunches such that the bunches always arrive when the field has the correct polarity for acceleration. The time variation of the field removes the restriction that the fixed potential drop limits the energy gain. For acceleration, the beam particles must be properly phased with respect to the fields, and for sustained energy gain they must maintain synchronism with those fields [2]. All modern particle accelerators use RF waves for acceleration.

1.2 Supercolliders

Without doubt, particle accelerators are among the important applications of high-power microwaves. A particle accelerator provides particle beams of high quality and high energy for a collider. The collision of two beams of sufficient high energy in a collider can resolve the internal structure of the nucleus and of its constituent subnuclear particles. For that reason, colliders have become the useful tools for learning about the world of subatomic particles. Measurements made using the beams from an electron linear accelerator have given us our present picture of the proton, which is made of pointlike particles called quarks.

The ongoing searching for the elementary particles that are the underlying basis of all matter has led to the design of supercolliders such as the proton-proton Superconducting Super Collider (SSC), whose construction was canceled in the United States [3]. However, the criticisms of the SSC did not question the universally acknowledged importance of the planned basic research in elementary particle physics. The SSC project was shut down because of its high construction cost that $11 billion or more was beyond what the country could afford to spend on a basic physics experiment. Therefore, the pursuit of advanced

knowledge in elementary particle physics will require those advances in particle accelerator technology that can significantly lower the cost of supercollider class experiments.

Physicists delve into the internal structure of the smaller particles that make up each proton and neutron: quarks and the gluons that bind them together. The ongoing exploration studies the matter in an unprecedentedly small distance scale, down to 10^{-19} meter. Thus, supercolliders are indispensable high-energy probes for such study. When two of the quarks collide head-on with energy as high as 2 trillion electron volts (TeV) or more, physicists believe that such collision will reveal many secrets in the deeper heart of matter—perhaps an exotic particle known as the Higgs boson, perhaps evidence of a miraculous effect called supersymmetry, or perhaps something unexpected that will lead to a large amendment of theoretical particle physics [4].

Advances in the technology of microwave amplifiers would allow for the construction of affordable electron-position colliders beginning at collision energy of 0.5 TeV and eventually extending to 5 TeV. It is generally agreed that a center-of-mass collision energy of 0.5 TeV is required to produce the physics output desired from a next-generation colliding beam machine [1]. A number of active programs are in progress around the world to carry out the research and development necessary for the realization of 0.5-TeV (center-of-mass energy) electron-positron linear collider. The research and development of new particle accelerators is certainly the major part of these supercollider research programs. The details of these research programs, especially the chosen accelerator technology, will be visited later in this chapter. There are so many topics that should be

included in the subject of colliders. However, our interest here will be limited to accelerators that produce colliding beams of electrons and positrons.

1.3 Why Linear Accelerators?

Considering the orbits of particle beams, there are two categories of particle accelerators: linear accelerators and circular accelerators. Circular accelerators are used for colliding beam storage rings, while linear accelerators are used for linear colliders.

The largest circular accelerator in operation is used in the LEP (Large Electron-Positron) machine located at CERN (European Center for Nuclear Research) in Geneva, Switzerland. It has a circumference of 27 km and is currently being operated at energy of about 50 GeV per beam. However, it is in the process of being upgraded to energy of about 100 GeV per beam (LEP-II) [5]. In such a circular accelerator, the circulating electrons or positrons continually lose energy by synchrotron radiation. The energy loss per particle due to synchrotron radiation varies directly as the fourth power of the beam energy, and inversely as the machine radius. This energy loss must be made up for by the action of RF accelerating cavities. In the case of LEP collider, the energy loss per turn is 1,860 MeV per electron at 90 GeV, and the radiated beam power is about 6 MW per beam for a circulating current of 3 mA. Superconducting RF cavities at a frequency of 350 MHz are being installed to provide the necessary accelerating voltage with acceptable RF system losses (cavity wall losses plus refrigeration power). Even so, the total wall-plug power needed to supply the RF system (including refrigerator) will be about 40 MW.

If collisions at energy greater than 90 GeV per beam are desired, one might consider scaling a LEP-type circular collider to a higher energy. A simple calculation will show that the total cost of such a scaled circular collider is minimized if the costs associated with the machine circumference and the costs associated with the RF power that must be provided are kept approximately equal. The circumference, the RF power, and the total cost of the machine will then scale as the square of the energy. To achieve center-of-mass collision energy of 500 GeV, an optimally scaled circular collider would have a circumference greater than 200 km, an input ac power (wall-plug power) for the RF system on the order of several hundred megawatts, and a total cost of at least ten billion dollars. Each of these quantities—circumference, cost, and ac power for the RF system—would be about eight times that for the present LEP collider.

On the contrary, in a linear collider, the length, the cost, and RF power requirement all scale roughly linearly with energy, because the straight-line trajectory of linear accelerator avoids power losses caused by synchrotron radiation [2]. In addition, the capability of providing strong focusing of linear accelerators produces high-quality and high-intensity beams. Therefore, linear accelerators are the preferred choices for the next-generation supercolliders.

With the advent of radar magnetrons giving high peak powers for pulsed short wavelength, the traveling-wave linear accelerator first worked in 1946 [6]. The world's first linear collider has already been built and is in operation at the Stanford Linear Accelerator Center (SLAC) at Stanford, California [7]. In the SLAC linear collider (SLC), both the electron and positron beams are accelerated in the 50-GeV SLAC S-band linear

accelerator (LINAC). Although the energy of the SLC is currently about the same as that of the LEP circular collider, the SLC is capable of producing unique physics because it is able to accelerate and collide polarized electrons, whereas it is very difficult to maintain polarized beams in a large storage ring-based collider. Of equal importance, the SLC is providing experience in producing, accelerating and colliding bunches of electrons and positrons with transverse dimensions on the order of 1 micron at the collision point.

In the circular storage ring, RF accelerating cavities can be a very short part of the total circumference, because particle beams pass through the accelerating section many times to be accelerated until the equilibrium between the energy gain and the energy losses from synchrotron radiation and wall losses is reached. Therefore, the accelerating gradient of those RF accelerating cavites is not the most important parameter compared to the wall losses of them. On the contrary, particle beams pass through the accelerating cavities only once in the linear accelerators. To achieve as high as possible acceleration gradient, which is the maximum axial longitudinal electric field in the acceleration structures, is the most important consideration besides minimizing RF losses of the cavities, when we design linear accelerators.

1.4 Worldwide Research and Development Programs on Linear Colliders

Table 1.1 lists the major programs active at the present time that are directed toward the development of future linear colliders. Our interest here is the research and development of linear accelerators in these collider programs.

Table 1.1 Major R&D Programs for the Supercollider

Program and Location	RF frequency and RF Power Source	Design Gradient Loaded/Unloaded	Test Facility
TESLA DESY Laboratory Hamburg, Germany	1.3-GHz klystrons (long pulse)	25 MV/m (superconducting accelerating cavities)	TESLA test facility (TTF)
NLC SLAC, Stanford, California, USA	11.4-GHz klystrons	55/75 MV/m	Final focus test beam (FFTB) NLC test accelerator (NLCTA)
JLC KEK Laboratory Tsukuba, Japan	11.4-GHz klystrons	28/60 MV/m	Accelerator test facility (ATF)
CLIC CERN Laboratory Geneva, Switzerland	30-GHz drive beam	80 MV/m	CLIC test facility (CTF)

The first entry in Table 1.1 is the TESLA (TeV Superconducting Linear Accelerator) program, and is based on the use of superconducting accelerating cavities at 1.3 GHz [8]. A superconducting cavity is in essence an RF pulse compressor, storing energy over a relatively long time period (on the order of a millisecond) from an RF pulse with a relatively low peak power. The major technical challenge for a superconducting linear collider is to achieve the designed accelerating gradient with an adequate cavity Q at an acceptable cost per meter of structure. The TESLA design calls for an acceleration gradient of 25 MV/m at $Q_0 \geq 5\times10^9$. Gradients of this order have been achieved in single test cavities at 1.3 GHz, and the substantial progress has been made to obtain such gradient in a nine-cell cavity. A vigorous worldwide research and development program on superconducting cavities is leading to improved cavity construction, surface treatment, and processing techniques, with the expectation for still higher accelerating gradients.

The second and third entries in Table 1.1 are the NLC (Next Linear Collider) and the JLC (Japan Linear Collider) research and development programs. They are directed toward an X-band collider with an initial unloaded accelerating gradient of 75 MV/m [9, 10]. Both NLC and JLC programs are based on scaling the current S-band iris-loaded linear accelerator technology to X-band. The current challenge of these two programs is that both types of structures cannot achieve an acceleration gradient greater than 50 MV/m without arcing damage at irises. The causes of such arcing damage have not been fully clarified, but one most likely reason is that the strong surface electric field at the iris exceeds the RF breakdown limit when the acceleration gradient is up to the 50 MV/m [11].

The CLIC (CERN Linear Collider) [12] project is devoted to research and development on a different type of linear collider based on the two-beam accelerator concept. In the CLIC design, 350-MHz superconducting cavities (similar to the LEP-II cavities) are used to accelerate a high-current, 5-GeV LINAC beam consisting of trains of bunches in which the spacing between the bunches in each train is the RF wavelength at 30 GHz. These bunch trains pass through a low-impedance transfer structure, where they induce about 40 MW of peak RF power for a pulse duration of 12 ns. This power is then transferred through a waveguide to the main linac. The energy extracted from the driving beam by the transfer structures is made up periodically by additional superconducting cavities. Such a two-beam accelerator avoids the need for high-frequency, high-peak-power RF sources. It is conceptually much like a transformer: a high-current, low-energy beam runs parallel to a low-current, high-energy beam and periodically transfer energy to it. The ratio of the accelerating gradient in the main linac to that of the drive linac corresponds to the turns ratio of the transformers. The technology of the CLIC two-beam accelerator is very demanding, and it is generally agreed that it is directed more toward a very-high-energy, high-gradient linear collider, rather than toward a next-generation 500-GeV center-of-mass machine. At present, the availability of high-frequency and high-peak-power RF sources is still an important factor determining the future success of these research and development programs on linear colliders.

From the wide range in the proposed operating frequencies (1.3 to 30 GHz) and gradients (20 to 100 MV/m) of the major linear collider research and development programs, it is clear that a sharply focused consensus does not at present exist on how to

design and build a 500-GeV linear collider. The choice of RF frequency for a linear collider underlies some basic differences in design philosophy. The low-frequency colliders (TESLA) have a larger beam size, a higher beam power, and looser tolerances on alignment and orbit control. The TESLA design at 1.3 GHz has the largest tolerances and also a very large bunch separation (allowing more time between collisions for the detectors to resolve particle tracks and to sort out the desired physics from background noise). However, it is based on superconducting RF cavity technology, which is not as well proven as the technology of conventional copper structures. The higher frequency collider design (10 to 30 GHz) have smaller beams, lower beam power, tighter tolerances, and higher accelerating gradients. The higher frequency machines can more readily be expanded to 1 TeV without becoming unfeasibly long. Perhaps the most important role of higher frequency and higher gradient is the reduction in the length of the machine. For example, the active length of a 5-TeV linear accelerator at X-band, at an accelerating gradient of 75 MV/m, would be about 70 km. Constructing a linear accelerator of this length is not entirely out of question, and it would certainly be better and more affordable to be able to get 5 TeV in a shorter length if at all possible. The future supercollider certainly needs a linear accelerator at a much higher frequency and a higher acceleration gradient. Higher operating frequency does not only mean shorter wavelength—more compact accelerating structure, but higher RF breakdown limit. The RF breakdown limit determines the maximum accelerating gradient that can be obtained and used in the given structure. For many years, the accelerator community has relied on the Kilpatrick criteria to predict RF breakdown limits of conventional copper structures as a function of frequency [13, 14]. For a higher operating frequency, a higher breakdown limit can be expected. This is one of

the reasons for us to dedicate our effort to develop X-band or higher frequency band accelerating structures. Some experimental results showed the RF breakdown limit of conventional copper disk-loaded accelerating structure, which is based on the Kilpatrick criterion, can be greatly exceeded [15, 16]. However, these are only empirical formula, while further research is needed to clarify underlying mechanisms.

1.5 Advanced Accelerator Concepts

The linear accelerators for these major R&D programs on colliders, which are listed in Table 1.1, are based on the conventional copper accelerating structures. However, the achievable maximum gradient is limited by the breakdown limit of such copper structures and the availability of high power RF sources. In addition, the fabrication of X-band and higher frequency band conventional iris-loaded structure is a major engineering challenge. If the limitation of the conventional accelerator technology can be exceeded, a tremendous reduction of cost can be expected for the supercollider. Besides the programs described above, a lot of more advanced accelerator concepts, other than the regime of conventional metal disk-loaded accelerating structures, are currently being investigated. Research programs on advanced accelerator concepts try to seek the solution of very high-energy and affordable linear accelerators in very diverse regimes. Major research areas of advanced accelerator concepts are laser and plasma acceleration [17], inverse free electron laser acceleration [18], dielectric wake-field acceleration [19-23], and externally powered dielectric loaded accelerators [24, 25]. Some experiments on these advanced accelerator concepts have shown that much higher acceleration gradients have been achieved in very short distance, but the research work on these concepts is still in the very early stage [26].

This thesis is based on the theoretical and experimental studies on externally powered dielectric loaded accelerating structures. As mentioned before, future very high-energy linear accelerators are expected to operate at X-band or higher frequency bands. This investigation, on dielectric loaded acceleration structures, will focus on X-band structures.

1.6 Dielectric Loaded Acceleration Structures

The proposed use of RF driven dielectric based structures for particle acceleration can be traced to the early 1950's [27]. To accelerate charged particles, the speed of propagation of electromagnetic waves must synchronize with the velocity of particles, which is always less than the speed of light. However, phase velocities of electromagnetic waves in empty waveguides have the speed of light as the lower bound. Therefore, electromagnetic waves must be slowed down from their normal speeds in empty waveguides to facilitate acceleration. This slowing may be accomplished by loading waveguides with metal disks as being done in all metallic waveguide linear accelerators. Partially loading waveguides with dielectric materials is another method to realize slow-wave structures. One widely studied dielectric loaded waveguide for accelerators is a dielectric-lined circular waveguide, shown in Figure 1.1. The center opening of such a waveguide is the channel for particles passing through. Some previous studies have examined the use of dielectric loaded circular waveguides as accelerating structures [24, 28]. The advantages of using accelerating structures based on dielectric-lined circular waveguides are summarized as follows:

— Simplicity of fabrication – the device is little more than a tube of dielectric surrounded by a conducting cylinder. This may be a great advantage for high

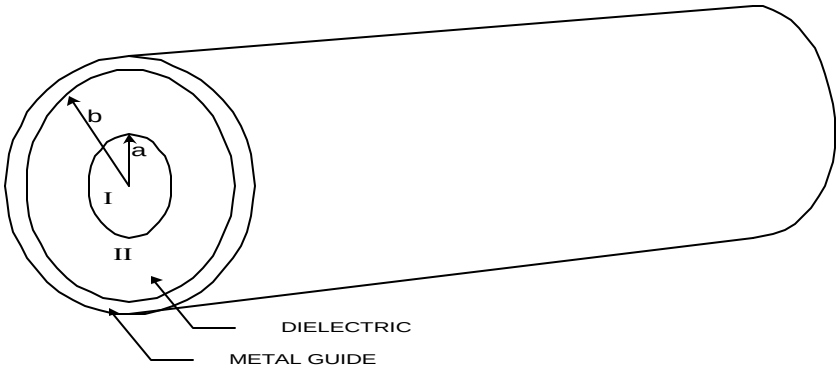

Figure 1.1 Dielectric-lined Circular Waveguide. Region I is vacuum, and region II is the dielectric ceramic.

frequency (10 GHz) structures over the conventional structures where extremely tight fabrication tolerances are required.

- Comparable shunt impedance with the conventional metal disk-loaded structure – for the given power flow, the maximum accelerating field that can be established in the dielectric loaded structure is close to that of the conventional metal disk-loaded acceleration structure.
- No dark current – because there in no free electrons in the dielectric ceramic, field emission that is the major cause of dark current will not happen under high electric field intensity.
- Simple reduction of coupled bunch effects – it has been demonstrated experimentally that it is relatively straightforward to build deflection damping into dielectric structure so that very large attenuation (≈250 dB/m) of all but TM_{0n} modes can be obtained [29, 30].
- Acceleration field is the maximum field in the structure – unlike the conventional disk loaded acceleration structure, whose peak electric field at the edge of iris is about twice the maximum axial electric field (acceleration gradient), the axial acceleration field of the dielectric lined waveguide is the maximum field in the structure.

On the other hand, there are some potential problems of applying dielectric loaded structures to particle acceleration, such as:

- Dielectric breakdown
- Joule heating

— Absorption gases in the dielectric materials

— Dimensional tolerances.

At the present, little information on these problems is available. Whether they are fatal or not should be answered through experiments conducted at high RF power level. This was one major reason to design and construct an X-band traveling-wave accelerating structure using dielectric-lined circular waveguide in the current research program.

The losses of dielectric materials available in the past were high, and they were easy to breakdown under high electric field. These problems made dielectric loaded structures unattractive for particle accelerators. The recent development of high dielectric constant (ε ~ 20 - 40), low loss dielectric materials (Q~ 10,000 - 40,000) brings serious consideration of dielectric structures as acceleration devices [31].

1.7 Overview of Research Programs on Dielectric Based Accelerators

Since the late 1980's, dielectric loaded accelerating structures have been investigated extensively and intensely. The major research sites conducting these research programs are the Argonne Wakefield Accelerator (AWA) facility at Argonne National Laboratory, and the Yale Beam Physics Laboratory of Yale University. Important experiments demonstrating the principles of dielectric based accelerators in the recent years are listed in Table 1.2. Most research efforts concentrated on dielectric wakefield acceleration. When a relativistic beam travels through a slow wave structure, it loses energy by producing electromagnetic waves as Cerenkov radiation [32]. The electromagnetic waves produced as Cerenkov radiation propagate at the same velocity as the beam, and follow it. Thus, such electromagnetic waves are known as wakefields. The idea behind these research

Table 1.2 Important Experiments on Dielectric Based Accelerating Structures

Location	Experiment
AATF Argonne National Laboratory	Demonstration of wakefield effects in dielectric structures [33].
AWA Argonne National Laboratory	1. AWA initial dielectric wakefield experiment [21]. 2. The transverse mode suppressor for dielectric wakefield accelerator [29, 30]. 3. Rf power generation and coupling measurements for the dielectric wakefield step-up transformer [34]. 4. High gradient dielectric wakefield device measurements [20]. 5. Measurements of wakefields in a multimode, dielectric wakefield accelerator driven by a train of electron bunches [35]. 6. Construction and testing of an 11.4 GHz dielectric loaded traveling-wave accelerating structure [25]. 7. Two beam acceleration in the dielectric step-up transformer [36].
Yale Beam Physics Laboratory Yale University	1. Microwave Inverse Cerenkov Accelerator [19]. 2. Stimulated dielectric wakefield accelerator [22].

programs is to utilize wakefields to accelerate particle beams, because high power RF sources are expensive to be built or unavailable at X-band and higher frequency bands. Several key experiments have demonstrated the principles of dielectric wakefield acceleration at the AATF facility and the AWA facility of Argonne National Laboratory, and at the Yale Beam Physics Laboratory of Yale University. The experiments have obtained the expected wakefield power at 2.86 GHz, 7.8 GHz, 10 GHz, and 15.6 GHz, respectively. The dielectric wakefield acceleration scheme used in these experiments is the collinear dielectric wakefield acceleration. The concept of such scheme is shown in Figure 1.2. In collinear dielectric wakefield acceleration, a low-intensity witness beam trailing behind a sequence of high-intensity but low-energy drive beams can be accelerated by the RF waves produced as Cerenkov radiation, if the witness beam is synchronized at the right phase. Adjusting the spacing of drive beam bunches leads to the high accelerating gradient that is resulted from the superposition of the wakefields caused by drive beam bunches.

It is well known that one major constraint of collinear wakefield acceleration is that the transformer ratio cannot exceed 2 [23]. In other words, the energy gain of a witness beam bunch cannot be larger than twice of the energy loss of one drive beam bunch, even though the acceleration field is the superposition of the wakefields of more than two drive beam bunches. Equivalently, the maximum acceleration gradient is always less than twice of the maximum axial wakefield amplitude of one drive beam bunch.

The AWA step-up transformer was proposed to overcome this constraint. The proposed design of such transformer is similar to the design of CLIC described in the previous section. Such scheme is to extract RF power from a relatively large diameter

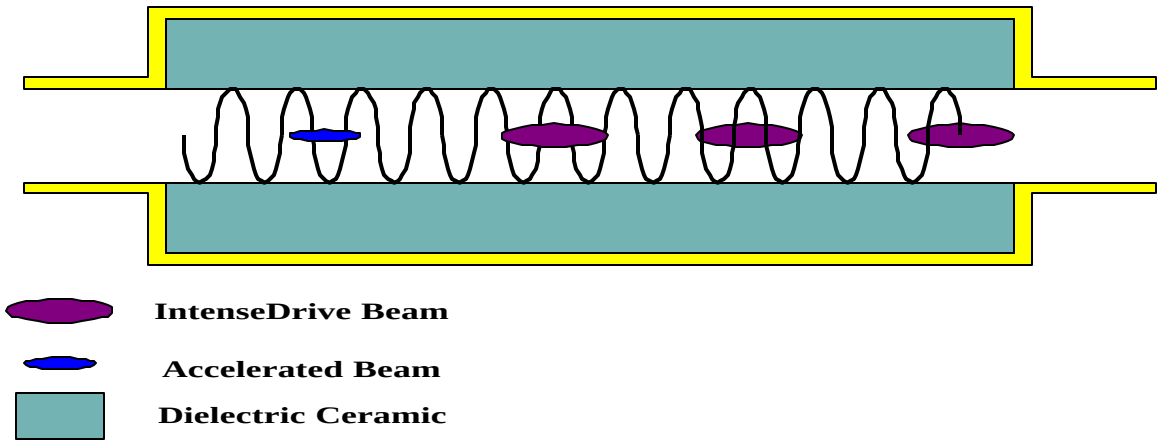

Figure 1.2 Schematic Drawing of Collinear Dielectric Wakefield Acceleration

dielectric-lined waveguide (stage I) in which high intensity drive beam bunches pass through and lose energy by Cerenkov radiation. The RF pulses are then coupled out and fed into a small-diameter dielectric-lined waveguide (stage II) where less-intensity witness beam bunches can be accelerated by the greatly enhanced axial electric field. Field enhancement results both from a lower group velocity in stage II than in stage I (longitudinal compression), and from geometrical effects made possible by the use of the smaller dielectric-lined waveguide (transverse compression). In simple words, the accelerating gradient established in the stage II is proportional to the number of RF pulses produced as Cerenkov radiation in stage I. Even though the amplitude of the axial wakefield of one drive beam may be small, such superposition will theoretically result in a significantly high accelerating gradient in stage II. The schematic drawing of the step-up transformer is given in Figure 1.3.

However, the fundamental questions about dielectric based acceleration structures, which were mentioned above, were not answered in the previous experiments. Because of the constraint of the transformer ratio and the limited intensity of drive beam bunches, the acceleration gradient established in the collinear dielectric accelerating structure did not reach the level that is necessary to explore the basic issues such as dielectric breakdown limit, Joule heating, and vacuum properties under high RF power. Furthermore, important techniques like the wave coupling scheme were not studied in collinear wakefield accelerating structures. Apparently, efficient coupling is essential for the step-up transformer to extract the wakefield produced in stage I and transfer it into stage II.

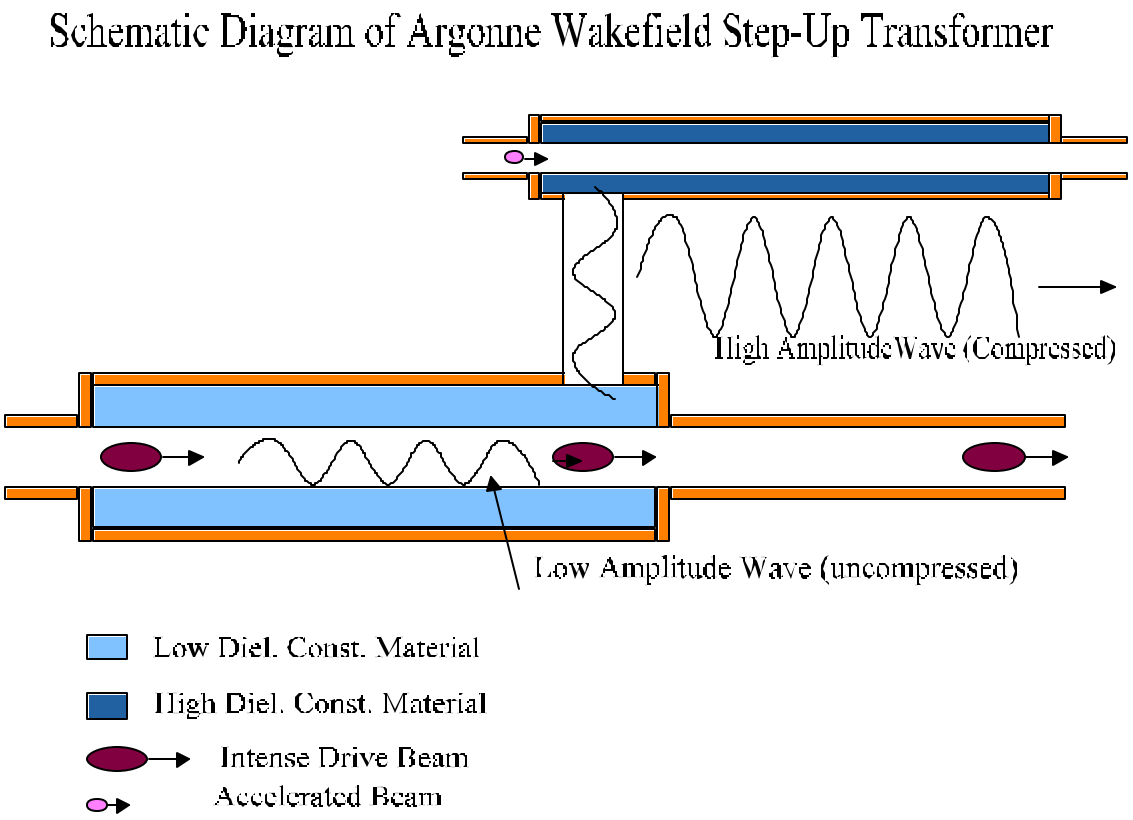

Figure 1.3 Schematic Drawing of AWA Wakefield Step-up Transformer Acceleration

The externally powered dielectric loaded accelerating structure was proposed to study the fundamental questions and techniques for dielectric loaded accelerators [24]. Some important progress has been achieved in the theoretical studies and engineering development [25]. The knowledge gained has been successfully applied to the development of step-up transformer. The experiments on the AWA stetp-up transformer were conducted in May 2000 [36], and the proposed experiments will test the 100 MV/m acceleration gradient after upgrading the facility [37].

1.8 Hybrid Dielectric-iris-loaded Periodic Acceleration Structures

One concern of conventional iris-loaded accelerating structures is the high ratio of peak surface electric field to peak axial electric field ($E_s/E_a \geq 2$) [38-40]. Such high ratio of electric fields may become a limitation for realizing technologies for very high gradient accelerators. We present a scheme that uses a hybrid dielectric and iris loaded periodic structure to reduce the ratio of peak surface electric field to acceleration gradient ($E_s/E_a \sim 1$), while the shunt impedance per unit length r (defined in pp. 37) and the quality factor Q do not diminish very much. The analysis based on MAFIA [41] simulations of such structures shows that we can lower the peak surface electric field close to the accelerating gradient with maintaining high acceleration efficiency that is measured by r/Q. Detail analysis and numerical examples of X-band hybrid accelerating structures are described. The peak surface electric field in conventional disk-loaded accelerating structure occurs at the irises and is at least twice the axial peak electric field. The high ratio of peak surface electric field to peak axial electric field is the constraint for NLC structure to achieve very high accelerating gradient close to the surface breakdown limit. One advantage of dielectric-

lined circular waveguides is that the peak surface electric field is very small. Figure 2.14 shows this property of a dielectric-lined circular waveguide. However, an acceleration structure based on such kind of waveguide has relatively lower *Q*.

We proposed a new kind of structure loading with both dielectric ceramic and irises to utilize the advantages of such two classes of structures. This novel accelerating structure may be able to reach the balance between the advantages of pure dielectric-loaded structures and conventional iris-loaded structures. Numerical studies on this class of structures have been carried out, and will be presented later. The analysis on dielectric-iris-loaded structures shows that it is a possible candidate to implement high gradient accelerator with a smaller ratio of E_s/E_a, relatively high *Q*, and shunt impedance.

1.9 Traveling-wave and Standing-wave Acceleration Structures

Acceleration structures can be designed for standing-wave operation or traveling-wave operation. A conventional iris-loaded standing-wave structure has to operate at π-mode in order to get the highest shunt impedance, a figure of merit for accelerators. Operation at the π-mode, without excitation of neighboring modes, requires the mode bandwidth be smaller than the frequency separation to the next mode. However, for iris-loaded structures, the mode separation in frequency domain decreases with increasing the number of cells. Thus standing-wave structures are not suitable for long accelerators. The π-mode operation also means increased sensitivity to frequency deviations and dimensional tolerances and a cell-to-cell phase deviation to compensate for the losses [42]. Consequently, the parts of a standing-wave accelerating structure are more expensive to fabricate because of sensitivity to tolerances. For achieving the same acceleration gradient,

an iris-loaded standing-wave accelerator empirically costs 20 percent more than an iris-loaded traveling-wave accelerator in construction. This may be also true for the hybrid dielectric-iris-loaded acceleration structure we proposed. Nevertheless, the mode separation between TM_{01m} modes is not a concern for standing-wave structures based on pure dielectric-lined waveguides, because they are just one-cell resonators, unlike multi-cell resonators in iris-loaded structures. However, the HEM-like resonance modes could be easily excited. Thus such hybrid modes may be the new challenge. These problems are beyond this thesis and should be investigated in further research.

Another reason for choosing traveling-wave operation is the availability of high power and high frequency circulators. A high power circulator must be used to isolate the RF source from power reflected from the standing-wave cavity. However, such high power circulators are not available due to potential arcing damages from the enhanced fields at X-band and higher frequency bands. The RF sources developed for NLC structures are capable of delivering pulses with 100 MW peak power at 11.4 GHz [43]. So far, there is no X-band circulator able to cope with such high RF power. Because the dielectric loaded accelerating structure we developed is dedicated for the high power experiments using the SLAC X-band klystrons, a traveling-wave structure is the only choice to minimize the reflected RF power at the input port.

Standing-wave structures also cause higher average heat dissipation than traveling-wave structures, where the filling time is shorter and the leftover RF power is taken out after the beam passage. This difference may be important, as the tiny size of the structures

at X-band and higher frequency bands imposes a limit on the cooling arrangement. This is one more reason for choosing traveling-wave acceleration structures.

As mentioned above, to build an X-band accelerating structure based on dielectric-lined circular waveguides for high power testing, the traveling-wave structure is the only choice we have. Meanwhile, high efficient coupling must be achieved between the dielectric loaded accelerating structure and the input and output waveguides to prevent deterioration of the performance of the device and to avoid arcing damage of the RF sources, namely the SLAC X-band klystrons. The method to overcome this engineering challenge will be discussed in Chapter 2.

1.10 Organization of the Thesis

The analysis of accelerating structures based on dielectric-lined circular waveguides will be presented in Chapter 2. The design of an 11.4 GHz externally powered dielectric-loaded traveling-wave accelerating structure will also be described. One important engineering task in implementing such accelerating structure is the achievement of efficient wave coupling. This will be discussed in the later part of Chapter 2.

The fabrication, bench measurement, vacuum testing, and high power testing of the structure will be described in Chapter 3. The major purpose of constructing such an X-band traveling-wave acceleration structure is to experimentally seek the fundamental knowledge of using dielectric loaded structure in particle acceleration.

Chapter 4 is focused on the efficient coupling scheme we arrived at. The MAFIA simulations of such coupling structure are presented, and the possible causes of inaccuracy

will be discussed. The results of the AWA step-up transformer experiment will be analyzed to show that such coupling scheme is useful to similar dielectric-loaded accelerating structures, and the accelerating mode can be correctly excited using this configuration.

A new direction of using dielectric in accelerating structures will be discussed in Chapter 5. A novel hybrid dielectric-iris-loaded accelerating structure is introduced to reduce the peak surface electric field, which is thought to be the cause of arcing damage and detuning of NLC-style structures in high power testing. Calculations will show that this kind of new structure is capable of achieving a lower peak surface electric field, while the acceleration performance will not be degraded. Chapter 6 is the conclusion of this thesis. Besides the summary of the current research program, some further research topics that should be investigated in the future study of dielectric-loaded acceleration structures are discussed.

CHAPTER II

DESIGN STUDIES OF ACCELERATORS USING DIELECTRIC-LINED CIRCULAR WAVEGUIDES

2.1 Dielectric-lined Circular Waveguides Basics

A dielectric-lined circular waveguide has a very simple geometry. It is merely a dielectric cylinder with inner radius a, outer radius b and surrounded by a conducting wall. The schematic drawing of such a waveguide is shown in Figure 2.1. As shown in Figure 2.1, region I is vacuum, and region II is dielectric filling. Such simple geometry makes dielectric-lined waveguides the valuable candidates for X-band and higher frequency band acceleration structures, because it is expensive and difficult to precisely fabricate conventional iris-loaded copper structures. The characteristics of such dielectric-lined waveguides will be discussed in the following.

It is well known that the transverse electric field E_t and magnetic intensity H_t in a waveguide can always be expressed in terms of the longitudinal components E_z and H_z

$$\begin{aligned}\left[\frac{\partial^2}{\partial z^2}-me\frac{\partial^2}{\partial t^2}\right]\vec{E_t} &= -jwm\nabla_t\times\vec{a_z}H_z+\nabla_t\frac{\partial}{\partial z}E_z\\ \left[\frac{\partial^2}{\partial z^2}-me\frac{\partial^2}{\partial t^2}\right]\vec{H_t} &= jwe\nabla_t\times\vec{a_z}E_z+\nabla_t\frac{\partial}{\partial z}H_z\end{aligned} \tag{2.1}$$

The longitudinal components have the following relations.

$$\begin{aligned}\left[\nabla^2-me\frac{\partial^2}{\partial t^2}\right]\overrightarrow{E_z} &= 0\\ \left[\nabla^2-me\frac{\partial^2}{\partial t^2}\right]\vec{H_z} &= 0\end{aligned} \tag{2.2}$$

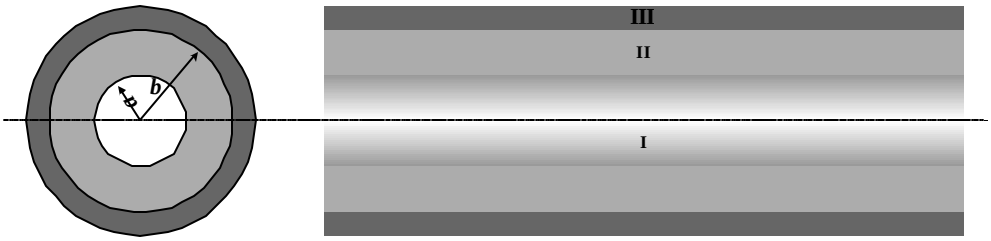

Figure 2.1 The Schematic Drawing of a Dielectric-lined Circular Waveguide. Region I is vacuum, region II is ceramic with dielectric constant of e_r, and region III is copper.

The boundary conditions of dielectric-lined circular waveguides at the interface between dielectric and vacuum, and on the conducting wall are

$$\begin{aligned} &E_{1t}(r=a) = E_{2t}(r=a) \\ &H_{1t}(r=a) = H_{2t}(r=a) \\ &E_{2t}(r=b) = 0 \end{aligned} \tag{2.3}$$

where E_{1t} and E_{2t} are the tangential electric field components in the vacuum region and dielectric region, respectively. Similarly, H_{1t} and H_{2t} are the tangential magnetic field components in such two different regions, respectively.

Applying these boundary conditions, the general solution of equation (2.2) can be expressed as

$$\begin{aligned} E_z &= \begin{cases} B_1 J_n(k_1 r)\cos(nf)e^{j(wt-k_z z)} & 0 \le r < a \\ B_2[J_n(k_2 r) - \dfrac{J_n(k_2 b)}{Y_n(k_2 b)} Y_n(k_2 r)]\cos(nf)e^{j(wt-k_z z)} & a \le r \le b \end{cases} \\ H_z &= \begin{cases} A_1 J_n(k_1 r)\sin(nf)e^{j(wt-k_z z)} & 0 \le r < a \\ A_2[J_n(k_2 r) - \dfrac{J_n'(k_2 b)}{Y_n'(k_2 b)} Y_n(k_2 r)]\sin(nf)e^{j(wt-k_z z)} & a \le r \le b \end{cases} \end{aligned} \tag{2.4}$$

where B_1, B_2, A_1 and A_2 are the field amplitudes in the region I (vacuum) and II (dielectric) respectively and are related by boundary conditions, and

$$\begin{aligned} k_1 &= w\sqrt{\frac{1}{c^2} - \frac{1}{v_p{}^2}} \\ k_2 &= w\sqrt{\frac{e_r}{c^2} - \frac{1}{v_p{}^2}} \\ k_z{}^2 &= k_0{}^2 - k_1{}^2 = e_r k_0{}^2 - k_2{}^2 \\ k_0{}^2 &= w^2 m_0 e_0 \end{aligned} \tag{2.5}$$

where v_p is the phase velocity of the wave traveling inside the tube, c is the speed of light in free space, k_1 and k_2 are the cutoff wave number in region I and II, respectively. The quantity k_z in Equation (2.5) is the wave propagation constant, assuming waves propagate along z axis. The quantity a is the radius of vacuum region (the opening for beam passing through), and b is the outer radius of dielectric (or the radius of such waveguide).

Using equations in (2.1), the components of transverse electric field can be written as

$$E_f = \begin{cases} \left[\frac{jwm_0}{k_1} A_1 J_n'(k_1 r) + \frac{jk_z n}{{k_1}^2 r} B_1 J_n(k_1 r)\right] \sin(nf) e^{j(wt-k_z z)} & 0 \le r < a \\ \left[\frac{jwm_0}{k_2} A_2 G_{nn}'(k_2 r) + \frac{jk_z n}{{k_2}^2 r} B_2 F_{nn}(k_2 r)\right] \sin(nf) e^{j(wt-k_z z)} & a < r \le b \end{cases}$$

$$E_r = \begin{cases} \left[-\frac{jwm_0 n}{{k_1}^2 r} A_1 J_n(k_1 r) - \frac{jk_z}{k_1} B_1 J_n'(k_1 r)\right] \cos(nf) e^{j(wt-k_z z)} & 0 \le r < a \\ \left[-\frac{jwm_0 n}{{k_2}^2 r} A_2 G_{nn}(k_2 r) - \frac{jk_z}{k_2} B_2 F_{nn}'(k_2 r)\right] \cos(nf) e^{j(wt-k_z z)} & a < r \le b \end{cases} \quad (2.6)$$

And the magnetic field can be expressed as

$$H_f = \begin{cases} \left[-\frac{jwe_0}{k_1} B_1 J_n'(k_1 r) - \frac{jk_z n}{{k_1}^2 r} A_1 J_n(k_1 r)\right] \cos(nf) e^{j(wt-k_z z)} & 0 \le r < a \\ \left[-\frac{jwe_r e_0}{k_2} B_2 F_{nn}'(k_2 r) - \frac{jk_z n}{{k_2}^2 r} A_2 G_{nn}(k_2 r)\right] \cos(nf) e^{j(wt-k_z z)} & a < r \le b \end{cases}$$

$$H_r = \begin{cases} \left[-\frac{jwe_0 n}{{k_1}^2 r} B_1 J_n(k_1 r) - \frac{jk_z}{k_1} A_1 J_n'(k_1 r)\right] \sin(nf) e^{j(wt-k_z z)} & 0 \le r < a \\ \left[-\frac{jwe_r e_0 n}{{k_2}^2 r} B_2 F_{nn}(k_2 r) - \frac{jk_z}{k_2} A_2 G_{nn}'(k_2 r)\right] \sin(nf) e^{j(wt-k_z z)} & a < r \le b \end{cases} \quad (2.7)$$

In the above equations, the following functions are defined for compactness in representation:

$$
\begin{aligned}
F_{nn}(k_2 r) &= J_n(k_2 r) - \frac{J_n(k_2 b)}{Y_n(k_2 b)} Y_n(k_2 r) \\
G_{nn}(k_2 r) &= J_n(k_2 r) - \frac{J_n'(k_2 b)}{Y_n'(k_2 b)} Y_n(k_2 r) \\
F_{nn}'(k_2 r) &= J_n'(k_2 r) - \frac{J_n(k_2 b)}{Y_n(k_2 b)} Y_n'(k_2 r) \\
G_{nn}'(k_2 r) &= J_n'(k_2 r) - \frac{J_n'(k_2 b)}{Y_n'(k_2 b)} Y_n'(k_2 r)
\end{aligned}
\tag{2.8}
$$

Equations (2.4), (2.6) and (2.7) are the general expressions of the electric and magnetic field components for all waveguide modes in the dielectric-lined waveguide. Using the boundary conditions at $r=a$ (E_z, E_f, H_f, and H_z continuous), one can reach the following system of equations:

$$
\begin{bmatrix}
\frac{wm_0}{k_1} J_n'(k_1 a) \frac{G_{nn}(k_2 a)}{J_n(k_1 a)} - \frac{wm_0}{k_2} G_{nn}'(k_2 a) & \frac{k_z n}{{k_1}^2 a} F_{nn}(k_2 a) - \frac{k_z n}{{k_2}^2 a} F_{nn}(k_2 a) \\
\frac{k_z n}{{k_1}^2 a} G_{nn}(k_2 a) - \frac{k_z n}{{k_2}^2 a} G_{nn}(k_2 a) & \frac{we_0}{k_1} J_n'(k_1 a) \frac{F_{nn}(k_2 a)}{J_n(k_1 a)} - \frac{we_r e_0}{k_2} F_{nn}'(k_2 a)
\end{bmatrix}
\begin{bmatrix} A_2 \\ B_2 \end{bmatrix} = \begin{bmatrix} 0 \\ 0 \end{bmatrix}
\tag{2.9}
$$

To have non-trivia solutions of this homogeneous equation, there must be

$$
\begin{vmatrix}
\frac{wm_0}{k_1} J_n'(k_1 a) \frac{G_{nn}(k_2 a)}{J_n(k_1 a)} - \frac{wm_0}{k_2} G_{nn}'(k_2 a) & \frac{bn}{{k_1}^2 a} F_{nn}(k_2 a) - \frac{bn}{{k_2}^2 a} F_{nn}(k_2 a) \\
\frac{bn}{{k_1}^2 a} G_{nn}(k_2 a) - \frac{bn}{{k_2}^2 a} G_{nn}(k_2 a) & \frac{we_0}{k_1} J_n'(k_1 a) \frac{F_{nn}(k_2 a)}{J_n(k_1 a)} - \frac{we_r e_0}{k_2} F_{nn}'(k_2 a)
\end{vmatrix} = 0
\tag{2.10}
$$

Thus the general dispersion relation for any waveguide mode inside the dielectric-lined waveguides can be obtained from Equation (2.10), leading to

$$\left[\frac{m_0}{k_1 a}\frac{J_n'(k_1 a)}{J_n(k_1 a)}-\frac{m_0}{k_2 a}\frac{G_{nn}'(k_2 a)}{G_{nn}(k_2 a)}\right]\left[\frac{e_0}{k_1 a}\frac{J_n'(k_1 a)}{J_n(k_1 a)}-\frac{e_r e_0}{k_2 a}\frac{F_{nn}'(k_2 a)}{F_{nn}(k_2 a)}\right]$$
$$=\frac{(k_z nw)^2}{(k_1 k_2 a)^4}(m_0 e_r e_0 - m_0 e_0)^2 \tag{2.11}$$

One of the solutions is TM_{01} mode. This mode has the following field components:

$$E_z=\begin{cases} B_1 J_0(k_1 r)e^{j(wt-k_z z)} & 0\le r<a \\ B_2\left[J_0(k_2 r)-\dfrac{J_0(k_2 b)}{Y_0(k_2 b)}Y_0(k_2 r)\right]e^{j(wt-k_z z)} & a\le r\le b \end{cases}$$
$$E_r=\begin{cases} -\dfrac{jk_z}{k_1}B_1 J_0'(k_1 r)e^{j(wt-k_z z)} & 0\le r<a \\ -\dfrac{jk_z}{k_2}B_2 F_{00}'(k_2 r)e^{j(wt-k_z z)} & a<r\le b \end{cases} \tag{2.12}$$
$$H_f=\begin{cases} -\dfrac{jwe_0}{k_1}B_1 J_0'(k_1 r)e^{j(wt-k_z z)} & 0\le r<a \\ -\dfrac{jwe_r e_0}{k_2}B_2 F_{00}'(k_2 r)e^{j(wt-k_z z)} & a<r\le b \end{cases}$$

And the dispersion relation of the TM_{01} mode is expressed as

$$\left[\frac{e_0}{k_1 a}\frac{J_0'(k_1 a)}{J_0(k_1 a)}-\frac{e_r e_0}{k_2 a}\frac{F_{00}'(k_2 a)}{F_{00}(k_2 a)}\right]=0 \tag{2.13}$$

To accelerate particle beams, the phase velocity v_p of the TM_{01} mode in such dielectric-lined circular waveguide must be synchronized with the beam velocity, and v_p should be the speed of light to accelerate relativistic particle beams. Meanwhile, the inner radius a is chosen based on the requirements of beam dynamics. Thus, the outer radius b should be adjusted accordingly to achieve the desired v_p. The geometric parameters a and b are not independent of each other for the given dielectric constant. The inner radius a is usually chosen as the governing parameter.

The deflecting modes in dielectric-lined circular waveguides are the HEM_{nm} modes. The lowest deflecting mode is the HEM_{11} mode, and it is the most harmful mode for acceleration [44, 45]. If the transverse electric force is too strong, the deflecting mode can cause beam break-up [46]. From Equation (2.11), we can have the dispersion relation for HEM_{1m} modes as the following

$$\left[\frac{m_0}{k_1 a}\frac{J_1'(k_1 a)}{J_1(k_1 a)}-\frac{m_0}{k_2 a}\frac{G_{11}'(k_2 a)}{G_{11}(k_2 a)}\right]\left[\frac{e_0}{k_1 a}\frac{J_1'(k_1 a)}{J_1(k_1 a)}-\frac{e_r e_0}{k_2 a}\frac{F_{11}'(k_2 a)}{F_{11}(k_2 a)}\right] = \frac{(k_z w)^2}{(k_1 k_2 a)^4}(m_0 e_r e_0 - m_0 e_0)^2 \tag{2.14}$$

Figure 2.2 shows the dispersion curves of phase velocity versus frequency for TM_{01} and HEM_{11} modes in a dielectric-lined circular waveguide with a=2.96 mm, b=4.53 mm, and e_r=20. Figure 2.3 gives the operating frequency of the TM_{01} mode and the HEM_{11} mode as a function of the propagation constant k_z, respectively. When k_z=0, the corresponding frequency is the cutoff frequency of such mode. It is shown in Figure 2.3 that the cutoff frequency of HEM_{11} mode is lower than that of TM_{01} mode. The intersections of such two dispersion curves with the speed of light line indicate that the propagation constant of HEM_{11} mode is less than that of TM_{01} mode, at the location where these two modes have the same phase velocity as the speed of light c. Thus the amplitude of the transverse wakefields caused by particle beams passing through such dielectric-lined waveguide is smaller than that of the longitudinal wakefield [45], because all the wakefield modes have the same phase velocity. This is very important for preventing Beam Break UP (BBU), and it is one advantage of using dielectric-lined circular waveguides as accelerators.

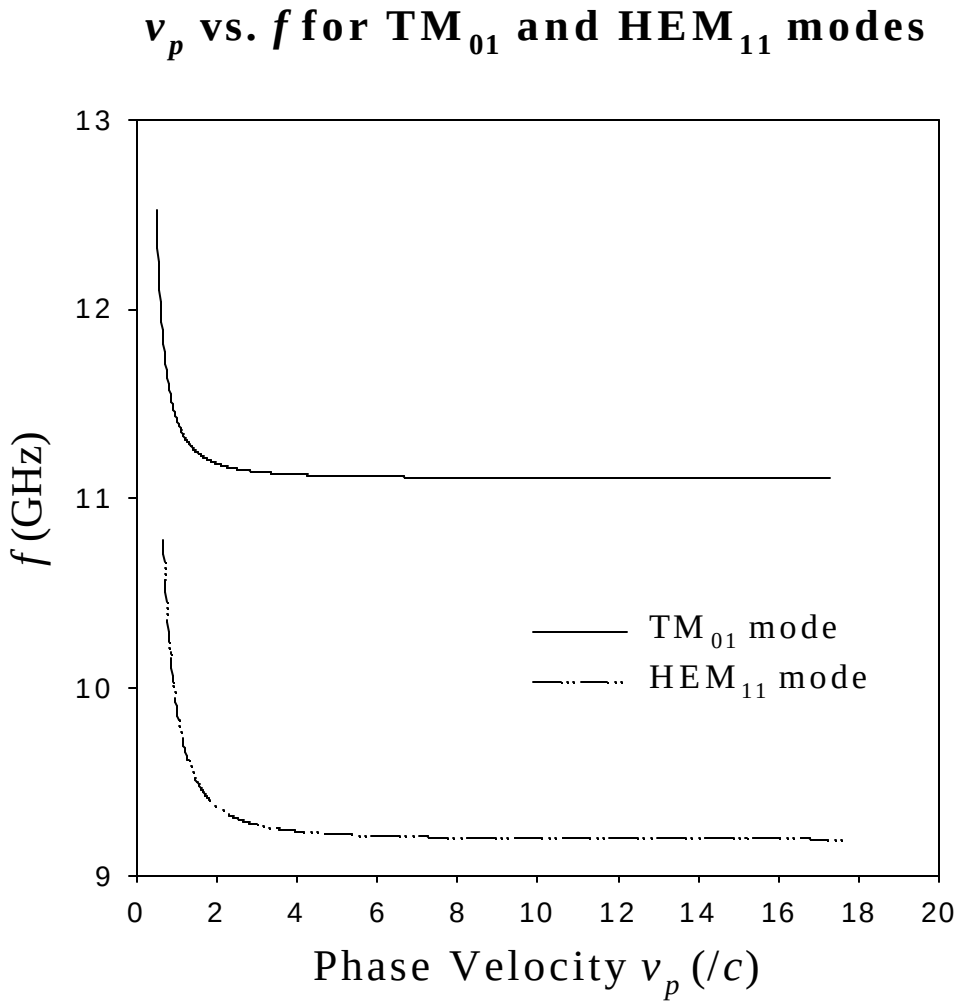

Figure 2.2 The Phase Velocities of the TM_{01} Mode and the HEM_{11} Mode versus Frequency in the Dielectric-lined Circular Waveguide Shown in Figure 2.1 with a=2.96 mm, b=4.53 mm, and e_r=20

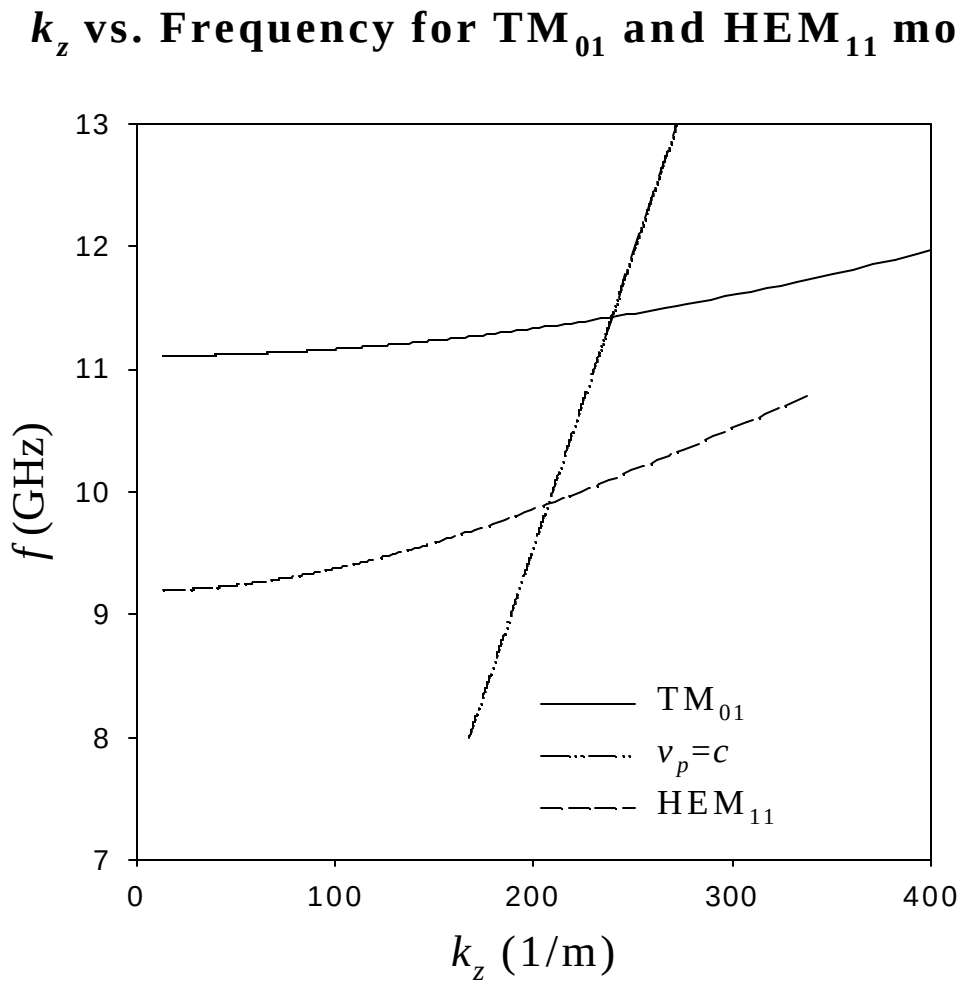

Figure 2.3 The Propagation Constants of the TM_{01} Mode and the HEM_{11} Mode versus Frequency in the Dielectric-lined Circular Waveguide Shown in Figure 2.1 with a=2.96 mm, b=4.53 mm, and e_r=20

However, the flip side of this characteristic is that this class of waveguide is able to support multiple propagating modes at the operating frequency for particle acceleration. Therefore, energy loss from mode conversion in such kind of waveguide is the engineering concerns. This problem is similar to using TE_{01} mode in an empty circular waveguide that can support multiple propagating modes at the operating frequency [47-50]. The thorough investigation on mode conversion in dielectric-lined circular waveguides is beyond the scope of this thesis, but it needs further studies.

Figure 2.4 shows the family of curves of phase velocity v_p versus frequency for the TM_{01} mode, when various dielectric constants are chosen, and the beam aperture radius a is fixed. Figure 2.5 shows the family of curves of phase velocity versus frequency for the HEM_{11} mode. Two sets of dispersion curves of the TM_{01} mode and the HEM_{11} mode are shown in Figure 2.6 and Figure 2.7, respectively. For a fixed beam opening size, the cutoff frequencies of both TM_{01} and HEM_{11} modes are lowered as the dielectric constant is decreased. Because the larger outer radius has to be chosen for the ceramic with the lower dielectric constant to synchronize the phase velocity of TM_{01} mode with beam velocity, the transverse dimension of such dielectric-lined circular waveguide is increased. Thus, the cutoff frequencies of waveguide modes are lowered.

Calculations with various beam opening radius have been carried out. Figure 2.8 and 2.9 show the frequencies of TM_{01} mode and HEM_{11} mode as functions of the phase velocities. The propagation constants versus the frequencies for the TM_{01} and the HEM_{11} modes are shown in Figure 2.10 and 2.11.

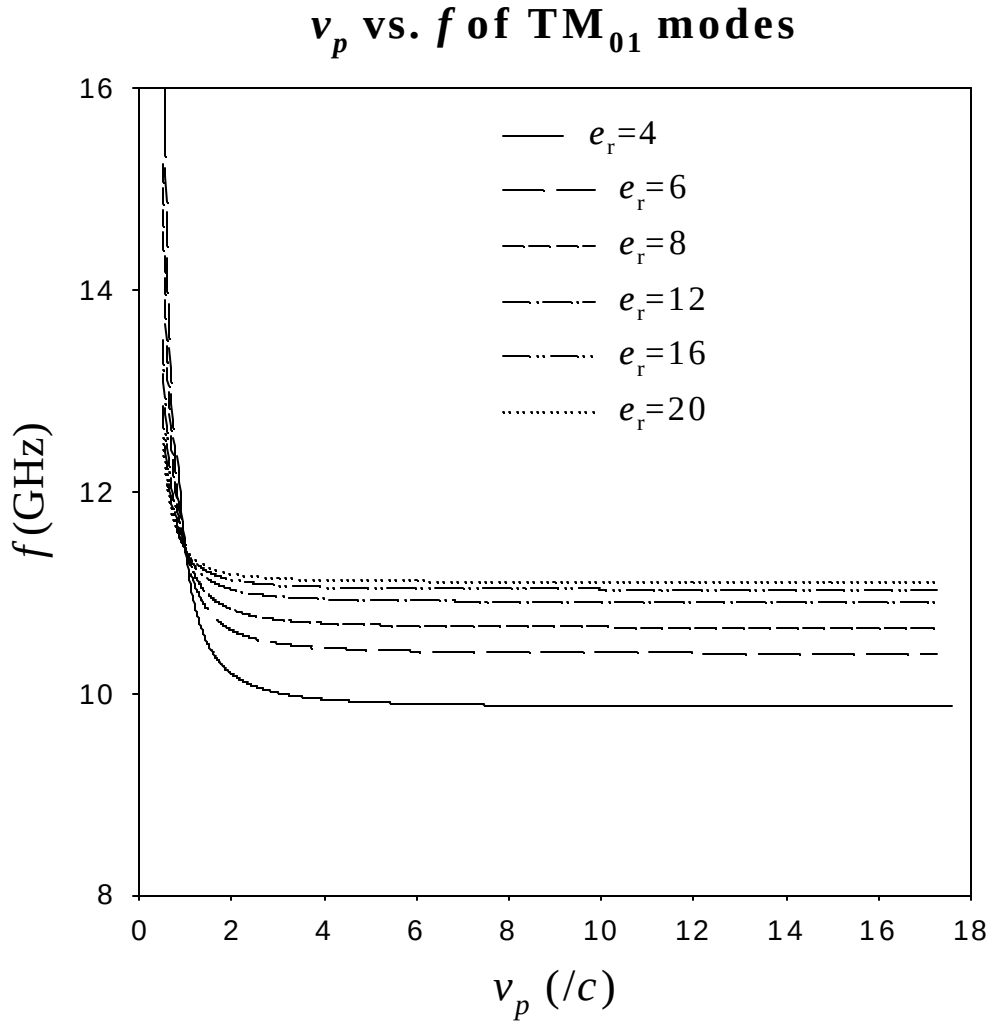

Figure 2.4 The Phase Velocities of the TM_{01} Mode versus Frequency in the Dielectric-lined Circular Waveguide Shown in Figure 2.1 with a=2.96 mm, and Various e_r. The outer radius b of these waveguides should be adjusted accordingly.

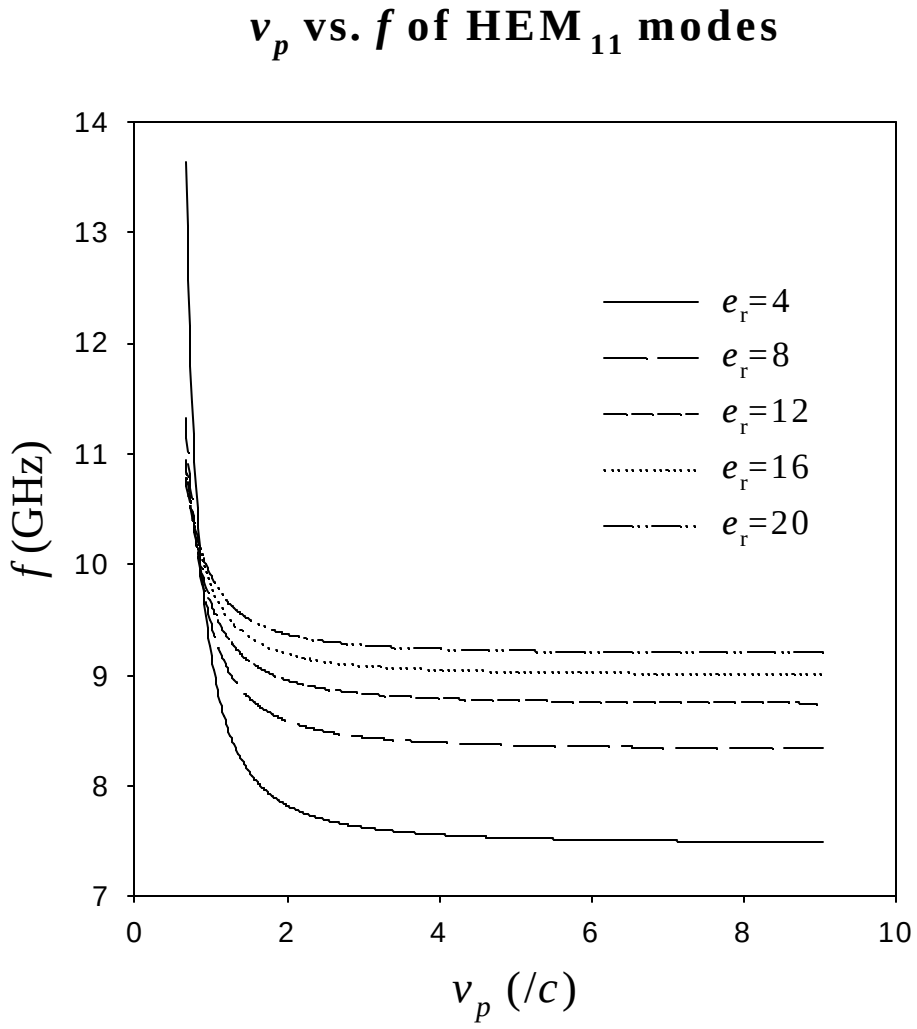

Figure 2.5 The Phase Velocity of the HEM_{11} Mode versus Frequency in the Dielectric-lined Circular Waveguide Shown in Figure 2.1 with a=2.96 mm, and Various e_r. The outer radius b of these waveguides should be adjusted accordingly to synchronize the phase velocity of TM_{01} mode with the velocity of relativistic particle beams.

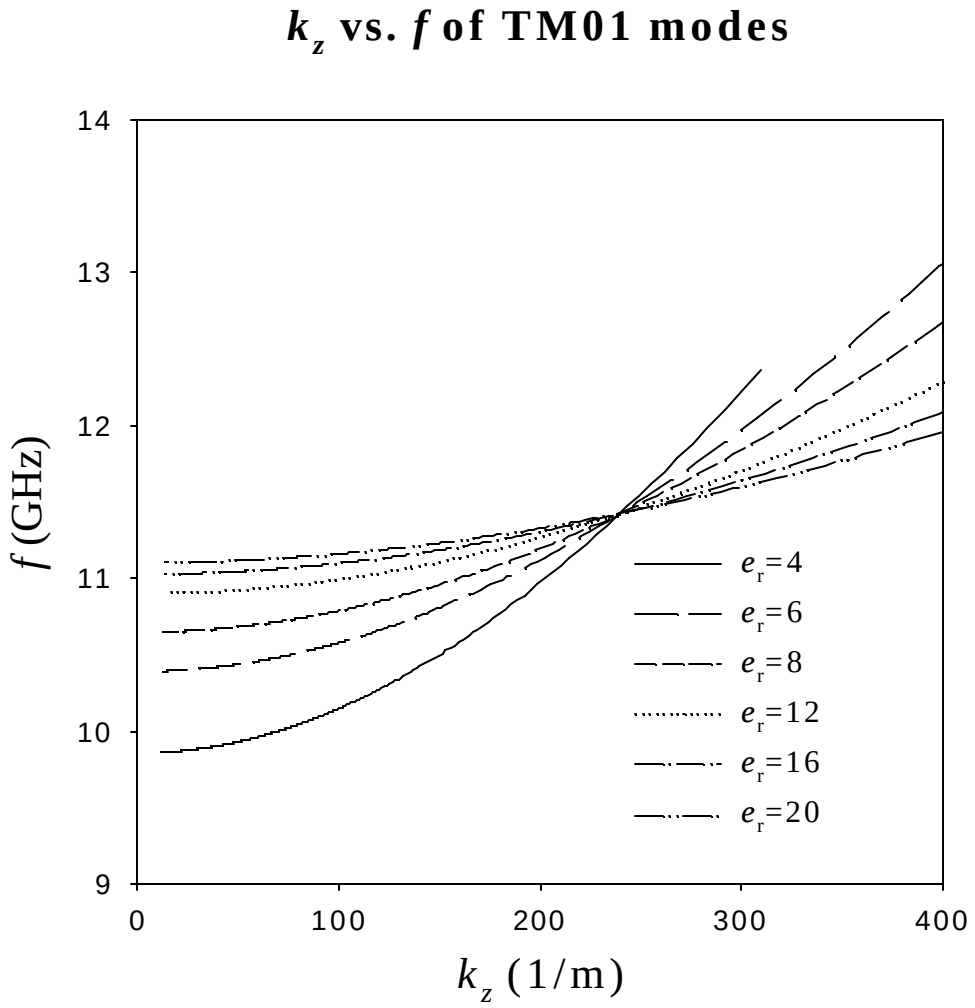

Figure 2.6 The Propagation Constant of the TM_{01} Mode versus Frequency in the Dielectric-lined Circular Waveguide Shown in Figure 2.1 with a=2.96 mm, and Various e_r. The outer radius b of these waveguides should be adjusted accordingly to synchronize the phase velocity of TM_{01} mode with the velocity of relativistic particle beams.

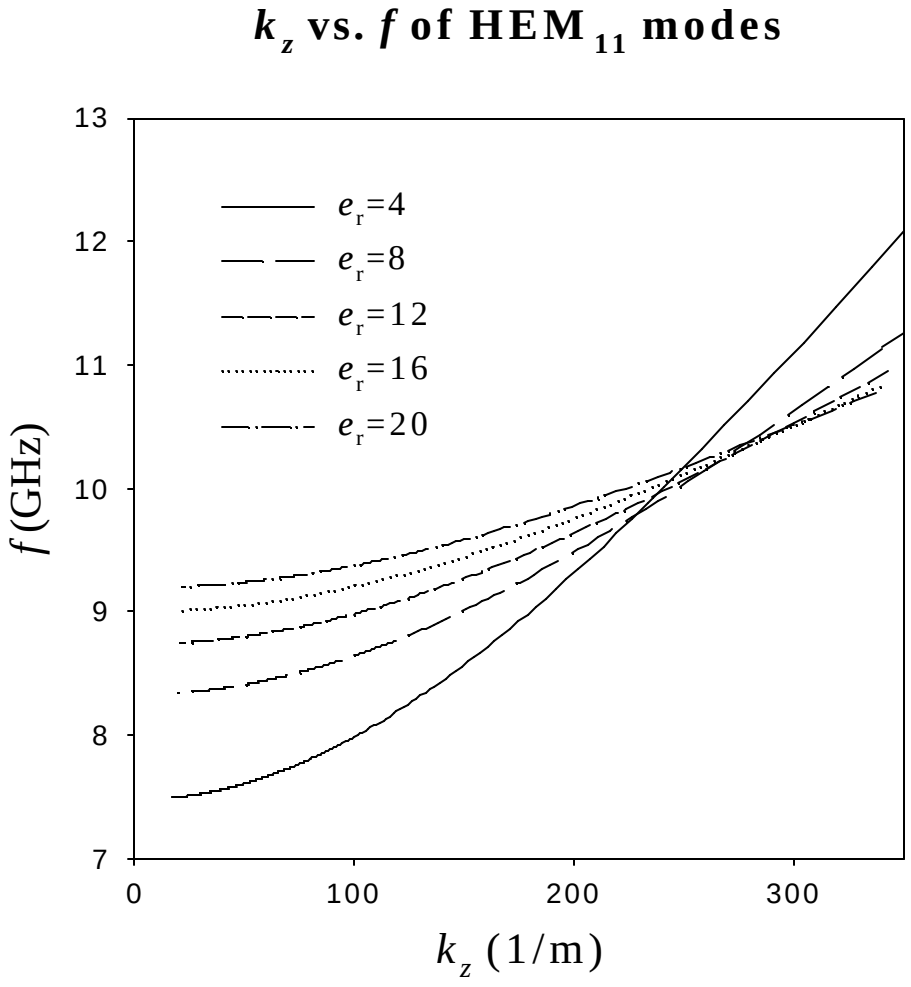

Figure 2.7 The Propagation Constant of the HEM_{11} Mode versus Frequency in the Dielectric-lined Circular Waveguide Shown in Figure 2.1 with a=2.96 mm, and Various e_r. The outer radius b of these waveguides should be adjusted accordingly to synchronize the phase velocity of the TM_{01} mode with the velocity of relativistic particle beams.

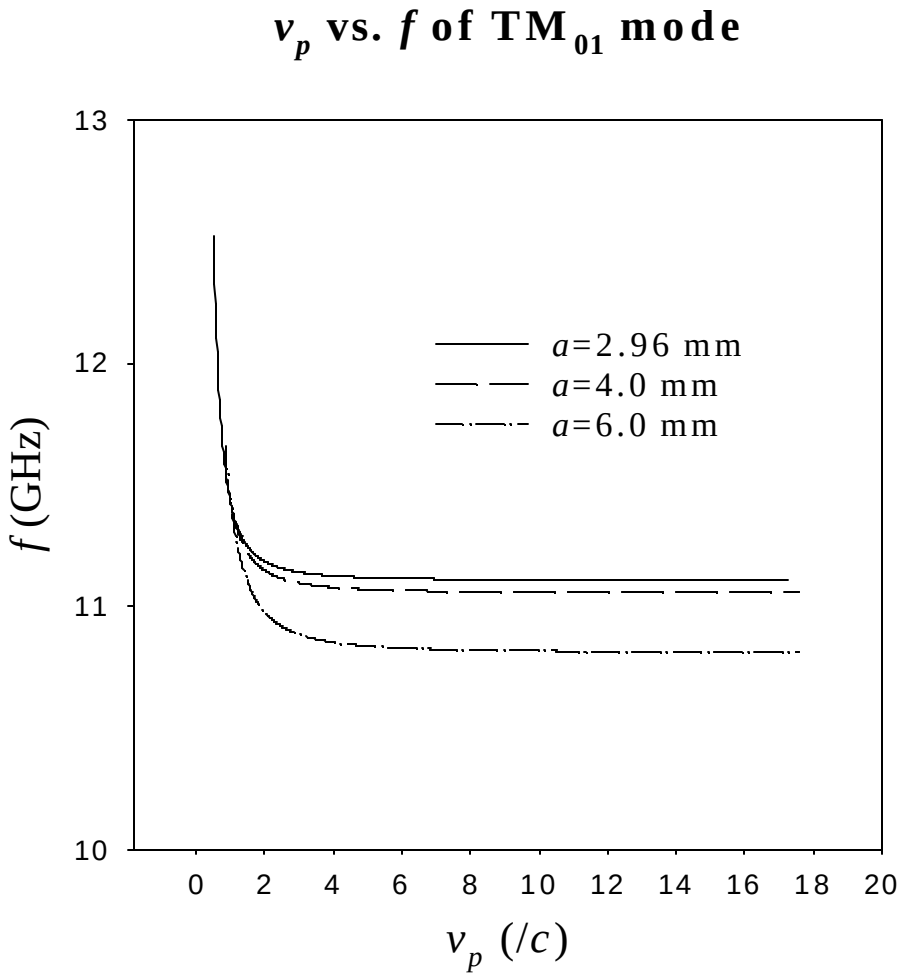

Figure 2.8 The Phase Velocity of the TM_{01} Mode versus Frequency in the Dielectric-lined Circular Waveguide Shown in Figure 2.1 with e_r=20, and the Various Beam Aperture Radius a. The outer radius b of these waveguides should be adjusted accordingly to synchronize the phase velocity of TM_{01} mode with the velocity of relativistic particle beams.

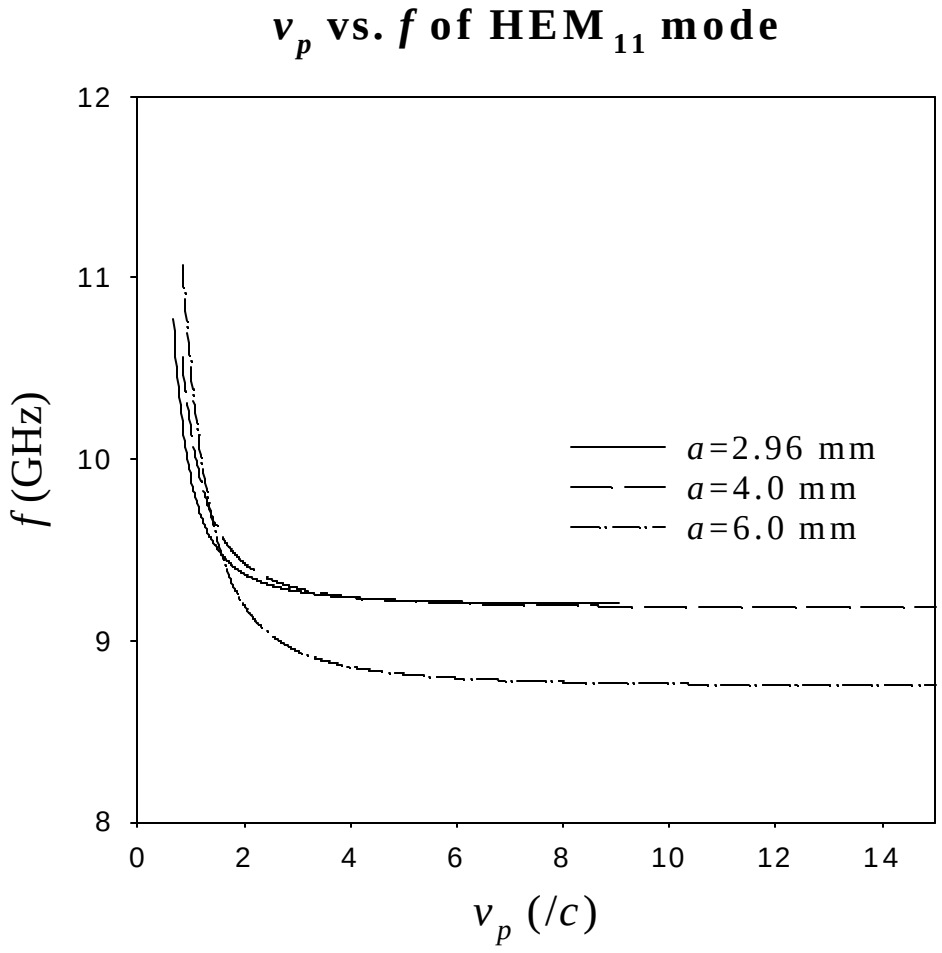

Figure 2.9 The Phase Velocity of the HEM_{11} Mode versus Frequency in the Dielectric-lined Circular Waveguide Shown in Figure 2.1 with e_r=20, and the Various Beam Aperture radius a. The outer radius b of these waveguides should be adjusted accordingly to synchronize the phase velocity of TM_{01} mode with the velocity of relativistic particle beams.

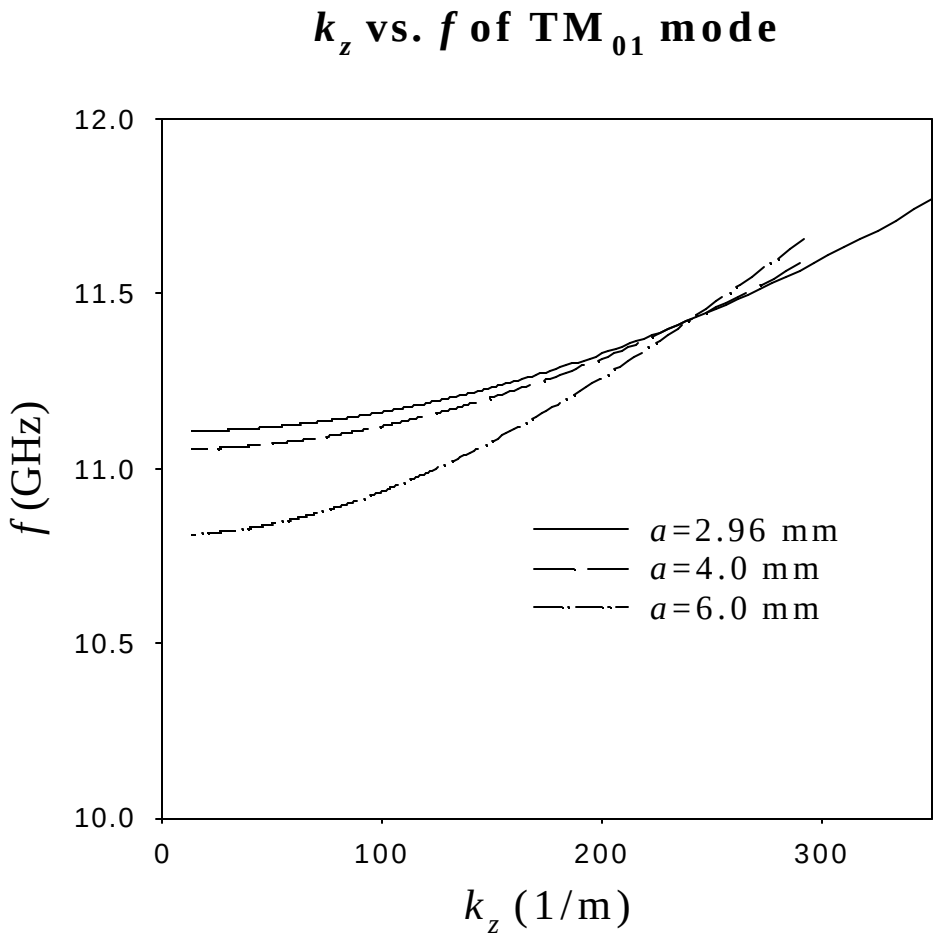

Figure 2.10 The Propagation Constant of the TM_{01} Mode versus Frequency in the Dielectric-lined Circular Waveguide Shown in Figure 2.1 with e_r=20, and the Various Beam Aperture Radius a. The outer radius b of these waveguides should be adjusted accordingly to synchronize the phase velocity of TM_{01} mode with the velocity of relativistic particle beams.

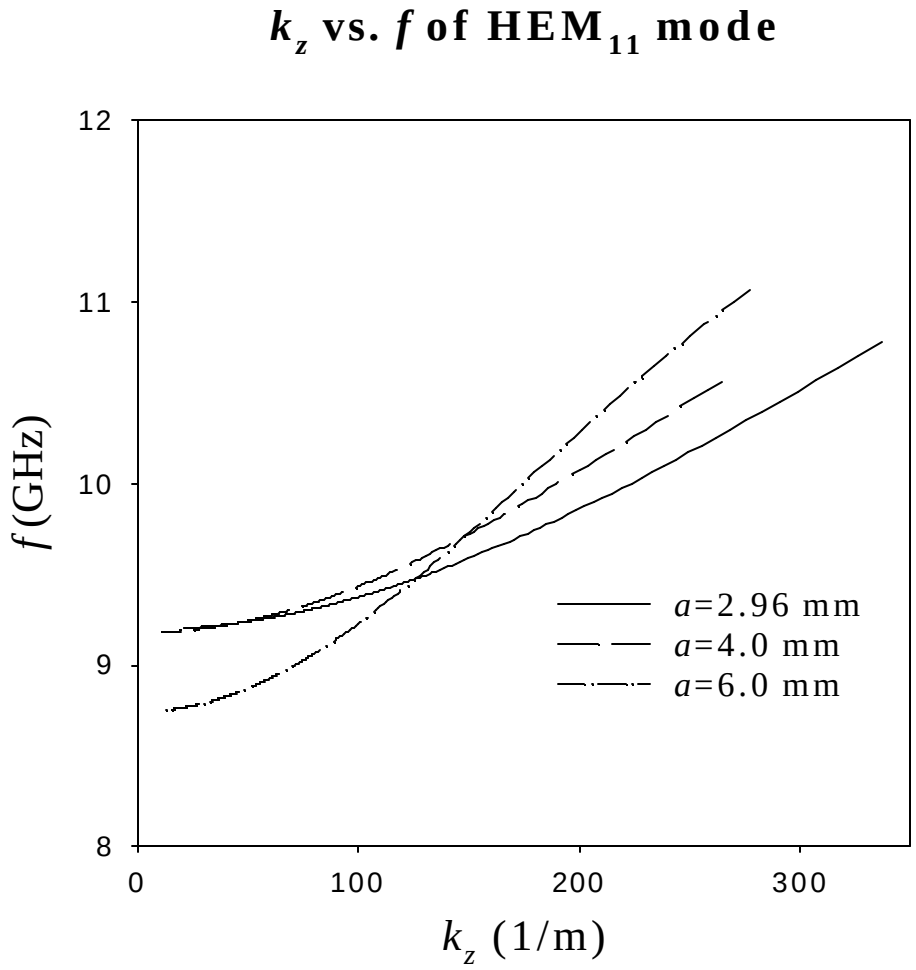

Figure 2.11 The Propagation Constant of the HEM_{11} Mode versus Frequency in the Dielectric-lined Circular Waveguide Shown in Figure 2.1 with e_r=20, and the Various Beam Aperture Radius a. The outer radius b of these waveguides should be adjusted accordingly to synchronize the phase velocity of TM_{01} mode with the velocity of relativistic particle beams.

The dispersion relations of the TM_{01} and the HEM_{11} modes have been discussed in previous sections. For particle acceleration, we are also interested in the field patterns of waveguide modes in such dielectric-lined waveguides, especially the accelerating TM_{01} mode. The electric fields of TM_{01} mode expressed in Equation (2.12) have very interesting characteristics. When the phase velocity of the TM_{01} wave is equal to c, the longitudinal electric field E_z is constant in vacuum region. This implies that there are no focusing and de-focusing forces for a relativistic particle traveling inside the vacuum region. This is critical for emittance preservation in the linear accelerators. Figure 2.12 shows the amplitude of E_z along the transverse radius at z=0. The vector electric field pattern plot that is obtained from MAFIA simulation at v_p=c is given in Figure 2.13. The constant longitudinal electric fields in the vacuum region can be easily identified at the transverse cross-sections where the transverse electric fields are zero. The distribution of the amplitudes of electric fields is shown in the contour plot and surface plot of Figure 2.14. Because of the cylindrical symmetry, only half part of the longitudinal cross section is drawn in Figure 2.14. We can see that the peak electric field of the TM_{01} mode occurs at the axis, when the phase velocity synchronizes with the velocity of relativistic particles. This is one distinct advantage of the dielectric-lined circular waveguides as accelerating structures. The distribution of the magnetic field amplitude is shown in Figure 2.15. The enhanced magnetic fields are concentrated in the dielectric region, and the peak magnetic field occurs on the wall. Meanwhile, the dielectric filling causes the enhanced surface magnetic field. It results in more power dissipation in dielectric loaded structures than in pure copper based structures.

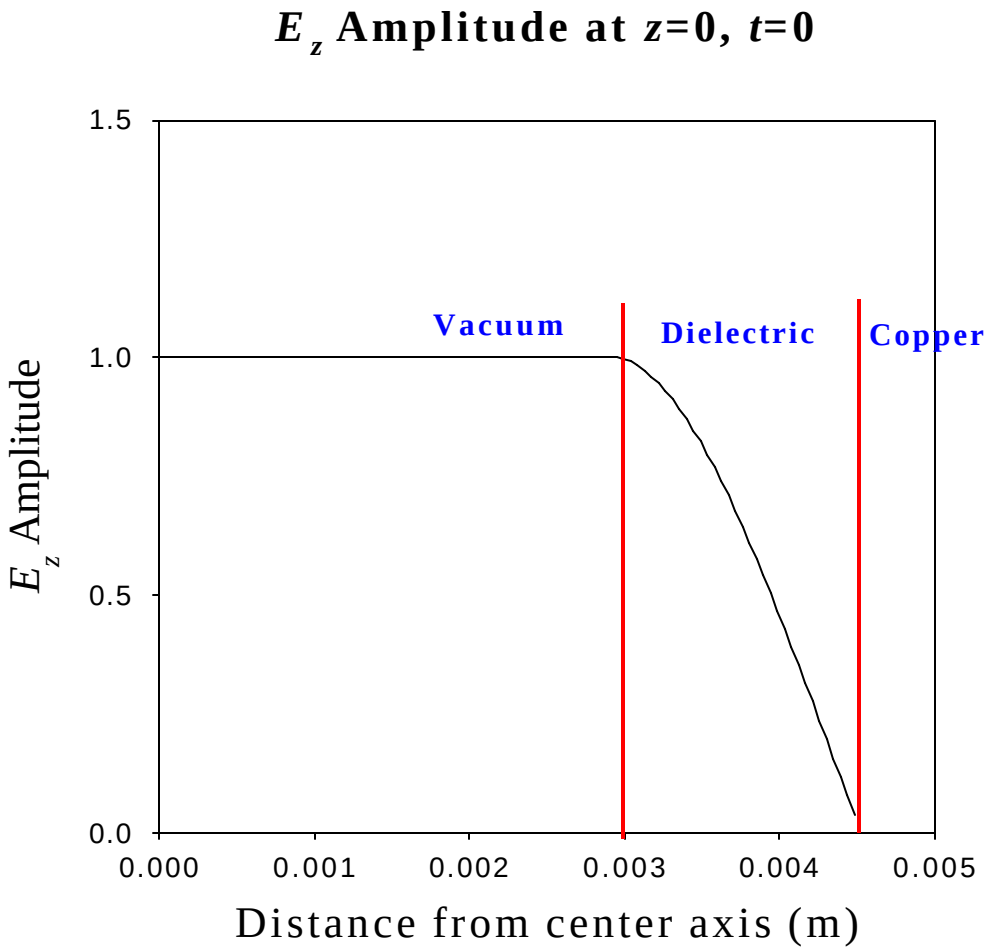

Figure 2.12 The Amplitude of E_z of the TM_{01} Mode along the Transverse Radius of the Dielectric-lined Circular Waveguide as Shown in Figure 2.1 with a=2.96 mm, e_r=20, and b=4.53 mm. The phase velocity of the TM_{01} wave is equal to c.

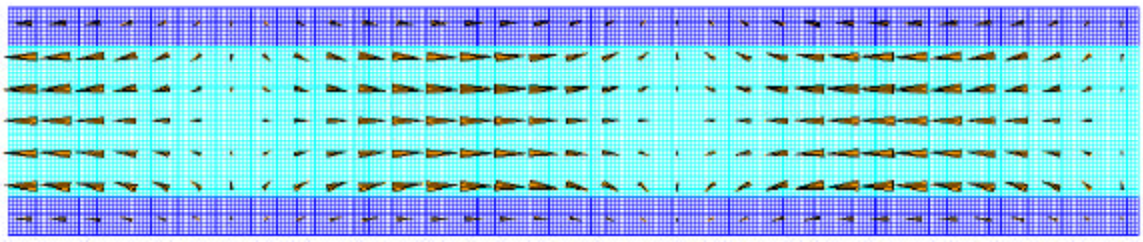

Figure 2.13 The Vector Electric Field Plot of the TM_{01} Wave in the Dielectric-lined Circular Waveguide Whose Geometric Parameters and Dielectric Constant are Given in Figure 2.12. The phase velocity of the TM_{01} wave is approximately equal to c.

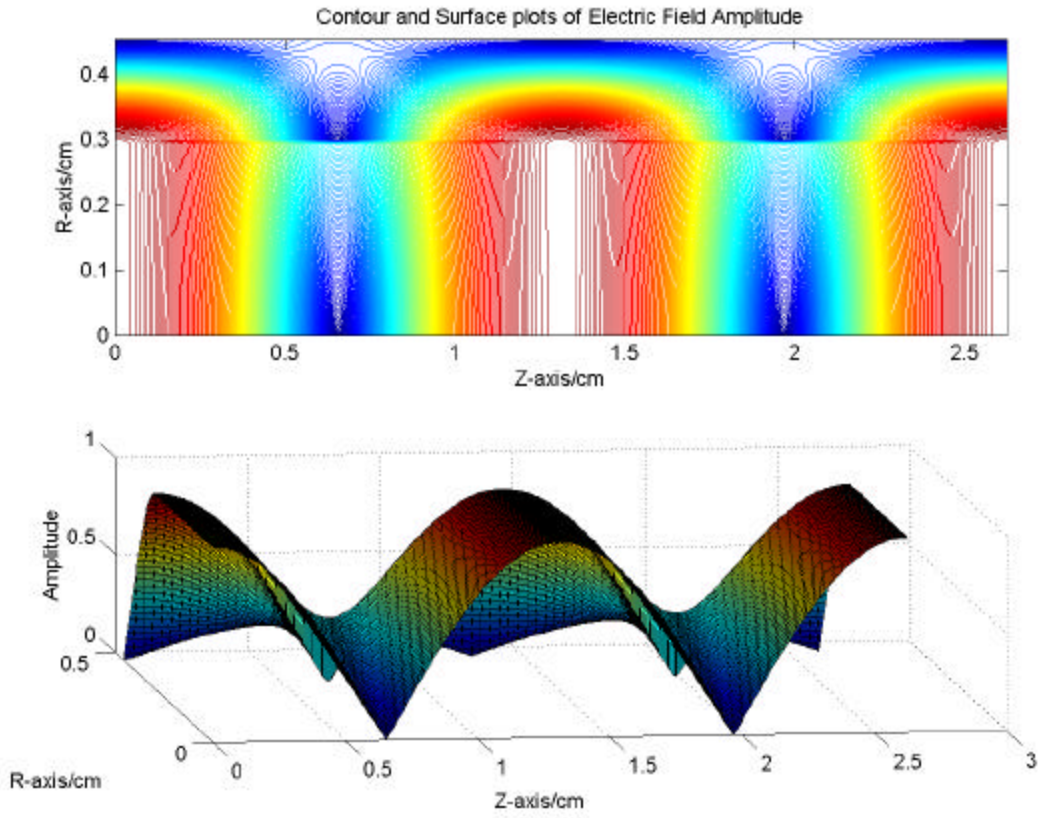

Figure 2.14 The Contour and Surface Plots of Electric Field Amplitude of the TM_{01} Wave in the Dielectric-lined Circular Waveguide Whose Geometric Parameters and Dielectric Constant are Given in Figure 2.12. The phase velocity of the TM_{01} wave is equal to *c*. The peak electric field occurs at the axis. In these plots, dark red indicates the highest amplitude.

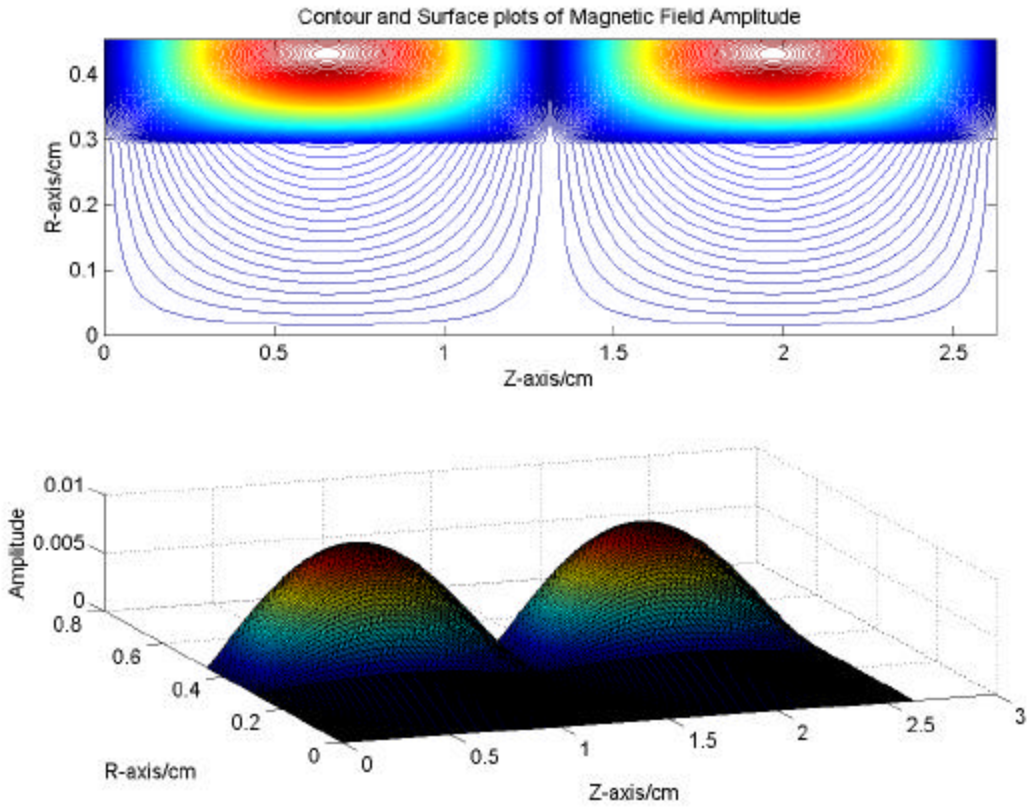

Figure 2.15 The Contour and Surface Plots of Magnetic Field Amplitude of the TM_{01} wave in the Dielectric-lined Circular Waveguide Whose Geometric Parameters and Dielectric Constant are Given in Figure 2.12. The phase velocity of TM_{01} wave is equal to *c*. The peak magnetic field occurs at the wall. In these plots, dark red indicates the highest amplitude.

The time average power dissipation per unit length P_{diss} and the time average stored energy per unit length U in the dielectric-lined circular waveguide are two important properties of such structures. P_{diss} consists of the power dissipated on the wall and in the dielectric, and can be expressed as

$$P_{diss} = \frac{R_s}{2}\int_S \left|H_\perp\right|^2_{r=b} ds + \frac{1}{2}\int_{\substack{Dielectric\\UnitLength}} we_r e_0 \tan d_l E^2 dV \tag{2.15}$$

where S is the surface area of the wall of unit length, R_s is the surface resistance of copper per unit length, $H_\perp(r=b)$ is the transverse magnetic field on the wall, and $\tan d_l$ is the loss tangent of the dielectric material. The surface resistivity R_s is defined as

$$R_s = \sqrt{\frac{m_0 w}{2s}} \tag{2.16}$$

where s is the conductivity of copper. In Equation (2.15), $we_r e_0 \tan d_l$ is an equivalent conductance of dielectric, thus the second part of such equation is the average power dissipation in dielectric material per period per unit length.

The average stored energy per period and per unit length is also composed of energy stored in vacuum region and that in dielectric region, and is expressed as

$$U = \frac{1}{4}\int_{\substack{Vacuum\\UnitLength}} \left(e_0 E^2 + m_0 H^2\right) dV + \frac{1}{4}\int_{\substack{Dielectric\\UnitLength}} \left(e_r e_0 E^2 + m_0 H^2\right) dV \tag{2.17}$$

The calculations of the power dissipation and stored energy per unit are important to obtain other parameters. In the following section we need briefly visit some important accelerator parameters.

2.2 RF Parameters of Traveling-wave Accelerators

To discuss the design of dielectric loaded accelerating structures, it is helpful to introduce some commonly used figures of merit for accelerating structures. Important considerations in dealing with design issues need to be addressed as well. Furthermore, the new accelerator technology based on dielectric loaded structure can be merited quantitatively.

Let us consider an electromagnetic wave propagating along the +z direction in a waveguide, with the electric field along the axis is given by

$$E_z(z,t) = E(z)\cos\left[wt - \int_0^z dk_z(z) + f\right] \tag{2.18}$$

where the wave number k_z is expressed in terms of the phase velocity v_p by $k_z(z) = w/v_p(z)$. For efficient particle acceleration, the phase velocity of the wave must be closely matched to the beam velocity. If we consider a particle of charge q moving along $+z$ direction, whose velocity $v(z)$ at each instant of time equals the phase velocity of the traveling wave, the particle arrives at position z at time $t(z) = \int_0^z dz / v(z)$, and the electric force on the particle is given by $F_z = qE(z)\cos f$. This particle is referred to as a synchronous particle, and the phase f is the synchronous phase. The phase f is zero if the particle arrives at the origin when the field is at a crest. It is negative if the particle arrives at the origin earlier

than the crest, and positive if it arrives later. The acceleration using the electromagnetic wave defined by Equation (2.18) is the traveling-wave acceleration. We need introduce some important accelerator parameters of such traveling-wave accelerating structure.

There are several figures of merit that are commonly used to characterize accelerating structures. Some of these depend on the power that is dissipated because of electrical resistance in the walls. The well-known quality factor of an accelerating structure is one of them. It is defined in terms of the time average power loss P_{diss} per unit length as

$$Q = \frac{wU}{P_{diss}} = \frac{wU}{P_{wall} + P_{dielectric}} \tag{2.19}$$

where U is the average stored energy per unit length, and P_{wall} and $P_{dielectric}$ are the power dissipation per unit length in the wall and dielectric, respectively. For X-band or higher frequency band structures, the power dissipation in the wall is much more than that in the dielectric, because of the largely increased skin effect. Equation (2.19) is equivalent to the following definition

$$\frac{1}{Q} = \frac{P_{wall} + P_{dielectric}}{wU} = \frac{1}{Q_{wall}} + \frac{1}{Q_{dielectric}} \tag{2.20}$$

where Q_{wall} and $Q_{dielectric}$ are the quality factors determined by wall loss and dielectric loss, respectively. For a circular waveguide partially loaded a thin layer of very low loss dielectric ceramic, $Q_{dielectric}$ is much greater than Q_{wall} in X-band or higher frequency band. Thus we can approximately have $Q \approx Q_{wall}$.

It is convenient to introduce some important relationships between the peak axial longitudinal electric field amplitude E_a (known as acceleration gradient), the stored energy per unit length U, and the traveling wave power flow P_w. The traveling-wave power of TM_{01} mode is obtained by integrating the Poynting vector over the transverse cross section and is

$$P_w = \frac{1}{2}\oint_s E_r H_f \, ds \tag{2.21}$$

The power dissipation per unit length in the structure is $-dP_w/dz$. The quality factor Q can also be expressed as

$$Q = \frac{wU}{-dP_w/dz} \tag{2.22}$$

The shunt impedance per unit length, a figure of merit that is independent of the excitation level of the acceleration structure and measures the effectiveness of producing an axial accelerating field amplitude for a given power dissipated, is defined by [51]

$$r = \frac{E_a^{\,2}}{-dP_w/dz} \tag{2.23}$$

The group velocity is another important parameter of traveling-wave accelerators. The definition of group velocity in a waveguide is expressed as

$$v_g = \frac{dw}{dk_z} \tag{2.24}$$

where k_z is the wave number of $+z$ direction, the wave propagating direction. For practical cases where the dispersion is not too large, the energy velocity is equal to the group

velocity. Thus the group velocity of a traveling wave can be calculated from the energy velocity $v_g = P_w/U$, where P_w the traveling-wave power and U is the time average stored energy per unit length. For a given z, we have:

$$v_g = \frac{\frac{1}{2}\int \mathrm{Re}(\vec{E}_r \times \vec{H}_f^{\,*})ds}{\int_{\substack{unit\\length}} \left(\frac{eE^2}{4} + \frac{mH^2}{4} \right) dV} \tag{2.25}$$

Eliminating U from the expression of the quality factor Q using $P_w = v_g U$ yields a differential equation for traveling-wave power,

$$\frac{dP_w}{dz} = -\frac{wP_w}{Qv_g} \tag{2.26}$$

We define the field attenuation per unit length as

$$a_0 = \frac{w}{2Qv_g} \tag{2.27}$$

So, Equation (2.26) becomes

$$\frac{dP_w}{dz} = -2a_0 P_w \tag{2.28}$$

The simplest case of an iris-loaded traveling-wave structure with uniform cell geometry independent of z and identical parameters for each cell, including Q, v_g, r, and a_0, is first considered. This is constant-impedance structure in the literature. A traveling-wave structure based on a uniform dielectric-lined circular waveguide is clearly a constant-impedance acceleration structure. For such a structure, the attenuation per unit length is constant, so the solution to Equation (2.28) is

$$P_w(z) = P_0 e^{-2\alpha_0 z} \tag{2.29}$$

where P_0 is the input RF power. This equation shows that the wave power is exponentially decaying. We can obtain a similar expression for the accelerating field amplitude. It is straightforward to show that the accelerating field and the traveling-wave power are related by

$$E_a^{\ 2} = \frac{wrP_w}{Qv_g} \tag{2.30}$$

And from Equation (2.28), we can have

$$\frac{dE_a}{dz} = -\frac{wE_a}{2Qv_g} = -\alpha_0 E_a \tag{2.31}$$

The solution of the above equation is

$$E_a(z) = E_0 e^{-\alpha_0 z} \tag{2.32}$$

where E_0 is the accelerating field amplitude at the beginning of the accelerating tank. At the end of a tank of length L, we have

$$\begin{aligned} P_w(L) &= P_0 e^{-2\tau_0} \\ E_a(L) &= E_0 e^{-\tau_0} \\ \tau_0 &= \alpha_0 L = \frac{wL}{2Qv_g} \end{aligned} \tag{2.33}$$

where τ_0 is the total power-attenuation parameter for that tank.

In an accelerating structure we are really more interested in maximizing the particle energy gain per unit power dissipation. The energy gain of an arbitrary synchronous particle with charge q riding at a phase ϕ relative to the crest of the wave is given by

$$\Delta W = q\cos f\int_0^L E_a(z)dz = qE_0\frac{1-e^{-t_0}}{t_0}\cos f \tag{2.34}$$

Using the relation between the input power P_0 and input field E_0 evaluated at z=0, we can show that $E_0^{\ 2} = 2ra_0P_0$, which leads to

$$\Delta W = q\sqrt{2rP_0L}\frac{1-e^{-t_0}}{\sqrt{t_0}}\cos f \tag{2.35}$$

If the input power and shunt impedance are fixed, the energy gain over a tank of length L depends on the total attenuation parameter t_0. From the above equations, we can see that the total attenuation parameter can be controlled by choosing the group velocity. If the value of t_0 is to be chosen to maximize the energy gain DW in the length L, it is found that the maximum occurs when $t_0 = (e^{t_0}-1)/2$, which has the solution as $t_0 \approx 1.26$, and Equation (2.35) yields for the maximum energy gain per tank for the optimized t_0 [51]

$$\Delta W_{\max} = 0.903q\sqrt{2rP_0L}\cos f \tag{2.36}$$

Clearly, if a particle is riding at the crest of the wave, when ϕ=0, it experiences the maximum axial electric field and obtains the maximum energy gain.

The choice of the group velocity v_g is an important issue in accelerator design [51]. If v_g is too small, the attenuation of the wave will be too great, and the field in the latter part of the structure will be very small. In this case, most of the power, which is traveling relatively slowly through the structure, is dissipated in the walls of the structure, resulting in a poor transfer of power to the particle beam. If v_g is too large, the initial accelerating field throughout the structure is also too small for efficient energy transfer to the beam. In

this case, most of the beam power passes rapidly through the structure and is delivered to the external load. However, the group velocity v_g, shunt impedance per unit length r, and Q are all functions of the geometry of the structure. For a good accelerator, the group velocity should be less than 10 percent of the speed of light [10].

Besides choosing the optimum group velocity, one of the main objectives in accelerating cavity design is to choose the geometry to maximize shunt impedance per unit length. This is equivalent to maximizing the energy gain in a given length for a given power loss.

Another useful figure of merit is the ratio of shunt impedance per unit length to Q, often called r over Q,

$$\frac{r}{Q} = \frac{E_a^{\,2}}{wU} \tag{2.37}$$

The quantity r/Q measures the efficiency of acceleration per unit stored energy at a given frequency. The accelerating field amplitude E_a in the above equation is the peak axial electric field amplitude. As we know, the electric field amplitude is exponentially damped as the wave propagates. E_a and U are both functions of z. At the entrance of an acceleration tank, E_a is E_0. This parameter is useful, because it is a function only of the cavity geometry and is independent of the surface properties that determine the power losses.

With these accelerator parameters, we can discuss how the structural parameters of a dielectric-lined circular waveguide affect the performance of the accelerator. Furthermore,

the design of an accelerator using a dielectric-lined circular waveguide can be considered as well.

Acceleration structure design generally requires electromagnetic field-solver codes that solve Maxwell's equations numerically for the boundary conditions specified. The parameters of the accelerator's characteristics can be obtained from the numerical solutions of field components of such structure. In our design procedures, we were benefited from several tools including field-solving codes we wrote in MathCAD [52], and MAFIA [41], a commercial electromagnetic field solver. The design of hybrid dielectric-iris-loaded structure, discussed later, was completely supported by the latter. To design a dielectric-loaded accelerating structure based on a dielectric-lined circular waveguide, we calculated the waveguide modes in such structure using a field-solving code written in MathCAD. The RF parameters introduced in the above were computed for models of X-band dielectric loaded acceleration structures with chosen geometric parameters and dielectric materials.

As discussed before, the group velocity of the TM_{01} mode is an important specification in the accelerator design. Equation (2.24) and (2.25) can be used to obtain the group velocity of the TM_{01} in the given structure. The plots in Figure 2.16 show the group velocity v_g of the TM_{01} mode as a function of the dielectric constant of ceramic, when the beam aperture radius a is fixed. From Figure 2.16, we can see that v_g decreases as the dielectric constant increases, for the given beam aperture radius. Another conclusion we can arrive at based on Figure 2.16 is that for the given dielectric material, the group velocity of the TM_{01} mode increases as the beam aperture radius increases. The constraint on choosing the beam aperture size is caused by the considerations of beam dynamics in

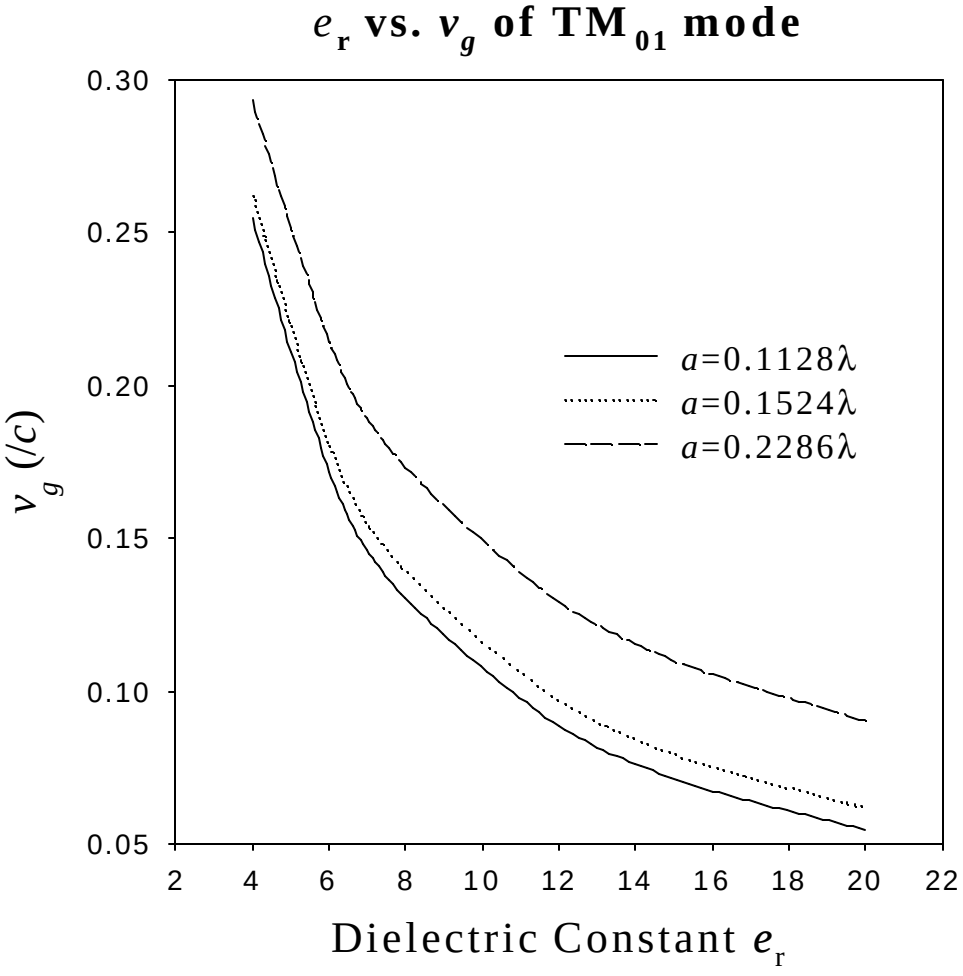

Figure 2.16 The Group Velocity v_g of the TM_{01} Mode as a Function of Dielectric Constant e_r with the Various Beam Aperture Radius a. The wavelength l=26.242 mm. For a given beam aperture radius and dielectric constant, the outer radius b should be adjusted accordingly to have the phase velocity of TM_{01} mode equal to the speed of light c.

such class of acceleration structures. Therefore, an optimization procedure should be applied to determine the geometry and dielectric constant of ceramic for such acceleration structure based on a dielectric-lined circular waveguide. However, our interest here will be limited the influence of the structure parameters on the RF parameters of the dielectric loaded acceleration structure.

Figure 2.17 shows the variation in the outer radius b of the dielectric filling as ε_r is varied for a given inner radius a to achieve the phase velocity of the TM_{01} mode equal to the speed of light c. It underscores that one of the three structure parameters a, b, and ε_r, shown in Figure 2.1, is dependent on the others.

The quality factor Q as a function of the dielectric constant of the ceramic and the beam aperture radius is shown in Figure 2.18. One interesting character here is that the quality factor is almost determined only by the dielectric constant of the ceramic. The beam aperture size shows very weak effects on the Q of dielectric loaded acceleration structure. It is clear that a higher value of dielectric constant results in a lower Q for a given beam aperture size. It is caused by the enhanced surface magnetic fields leading to an increase in the power dissipation on the wall. At the same time, the higher dielectric constant also means smaller group velocity. To achieve a group velocity less than $0.1c$, the quality factor of such dielectric loaded structure degrades substantially. This is one drawback of using a dielectric-lined circular waveguide as an accelerator. On the contrary, the quality factors of pure metallic iris-loaded accelerating structures are almost constant over a range of group velocities of the TM_{01} mode.

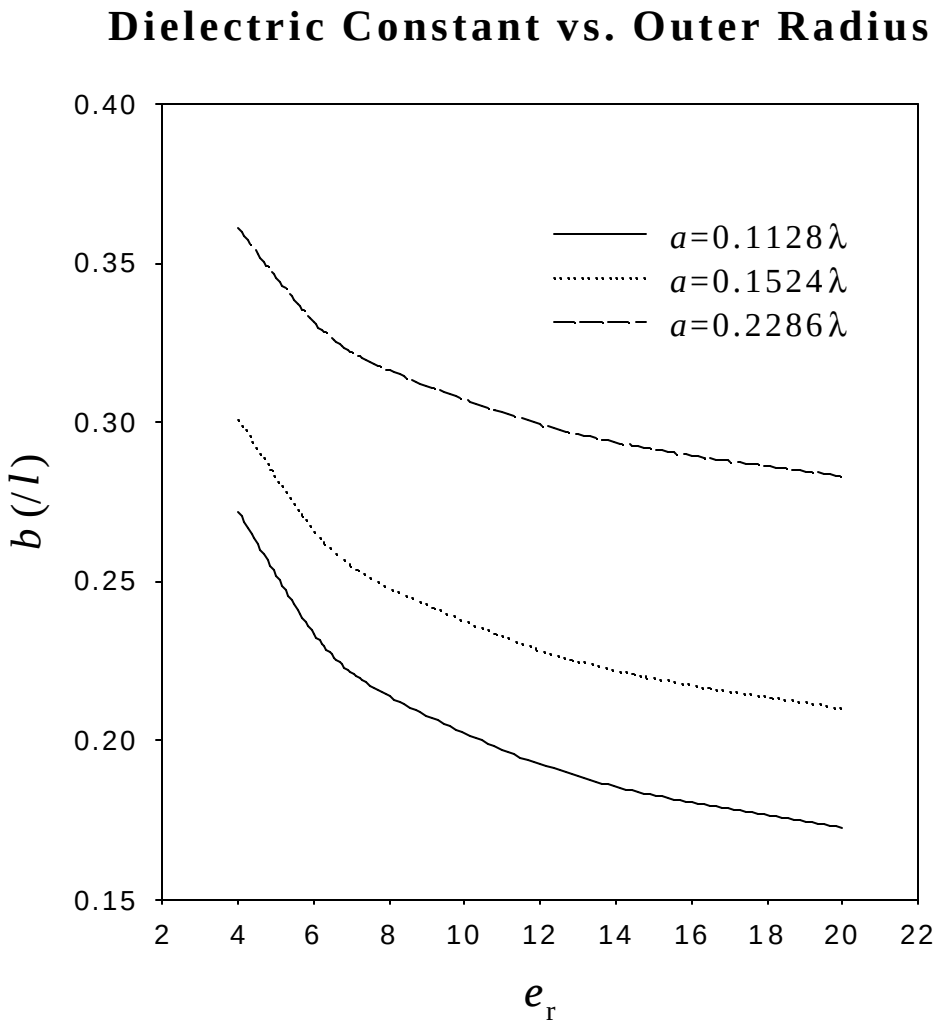

Figure 2.17 The Outer Radius b of the Dielectric-lined Waveguide Varies as a Function of the Dielectric Constant e_r with the Various Beam Aperture Radius a. The wavelength l=26.242 mm. For given beam aperture radius and the dielectric constant, the outer radius b must be adjusted accordingly to have the phase velocity of the TM_{01} mode equal to the speed of light c.

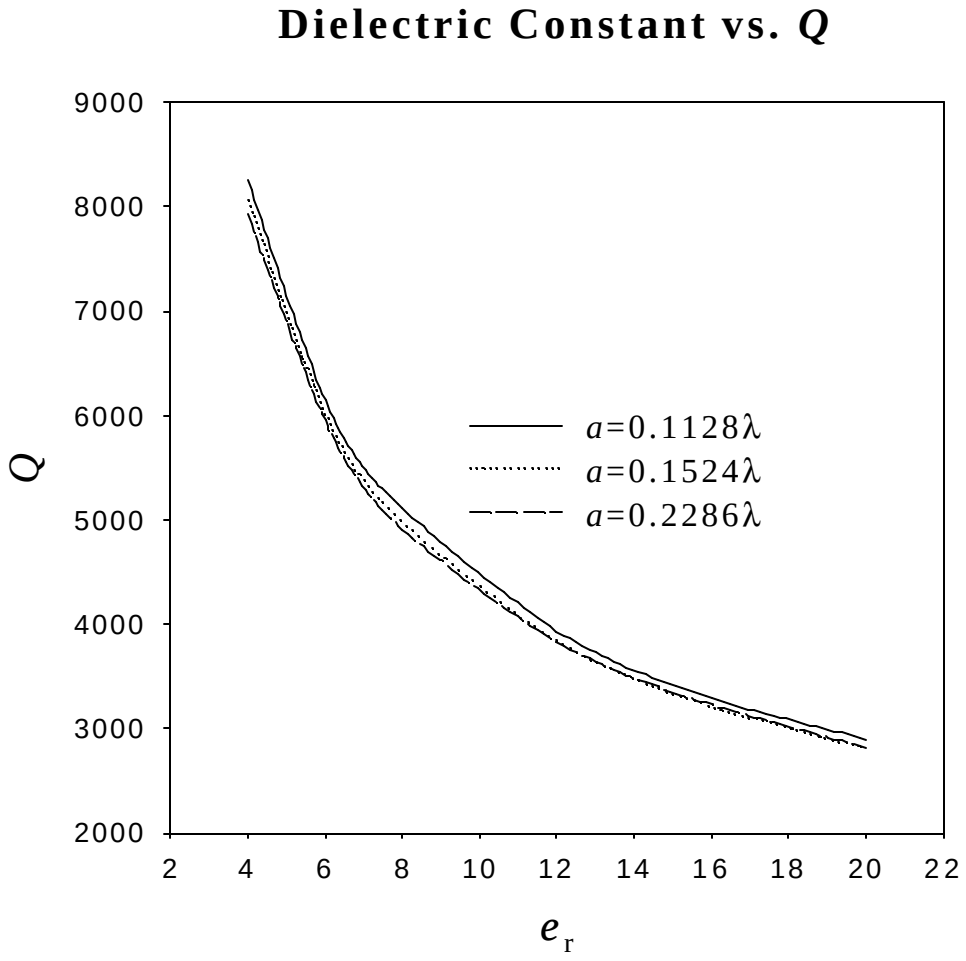

Figure 2.18 The Dielectric Constant versus the Quality Factor Q of the Dielectric Loaded Acceleration Structure, with the Various Beam Aperture Radius a. Here the wavelength l=26.242 mm. For a given beam aperture radius and a dielectric constant, the outer radius b must be adjusted accordingly to have the phase velocity of the TM_{01} mode equal to the speed of light c.

The shunt impedance per unit length r indicates the acceleration effectiveness to per unit power dissipation. From Equation (2.23) and (2.26), we can have r expressed as

$$r = \frac{E_a{}^2 Q v_g}{w P_w} \tag{2.38}$$

Figure 2.19 shows the shunt impedance per unit length as a function of the dielectric constant of the ceramic and the beam aperture radius. The shunt impedance decreases as the dielectric constant increases, as a result of higher power dissipation. Moreover, the smaller the beam hole, the higher shunt impedance. The shunt impedances of these dielectric-loaded accelerating structures are comparable to those of metallic iris-loaded structures. One example of X-band metallic iris-loaded accelerating structure has been described in chapter 5.

The curves in Figure 2.20 show how r/Q varies as the function of the dielectric constant and the beam hole radius. The figure shows that r/Q decreases as increasing dielectric constant, which is equivalent to reducing the value of the group velocity. The compensation for the degraded Q is the enhanced r/Q, considering the typical values of r/Q of metallic iris-loaded accelerating structures. In other words, the dielectric loaded accelerating structures have better acceleration efficiency per unit energy stored. It should be emphasized that both r and r/Q are functions of v_g. Thus the comparison with conventional metallic accelerating structures should be made when two classes of structures have the same group velocity of the TM_{01} wave.

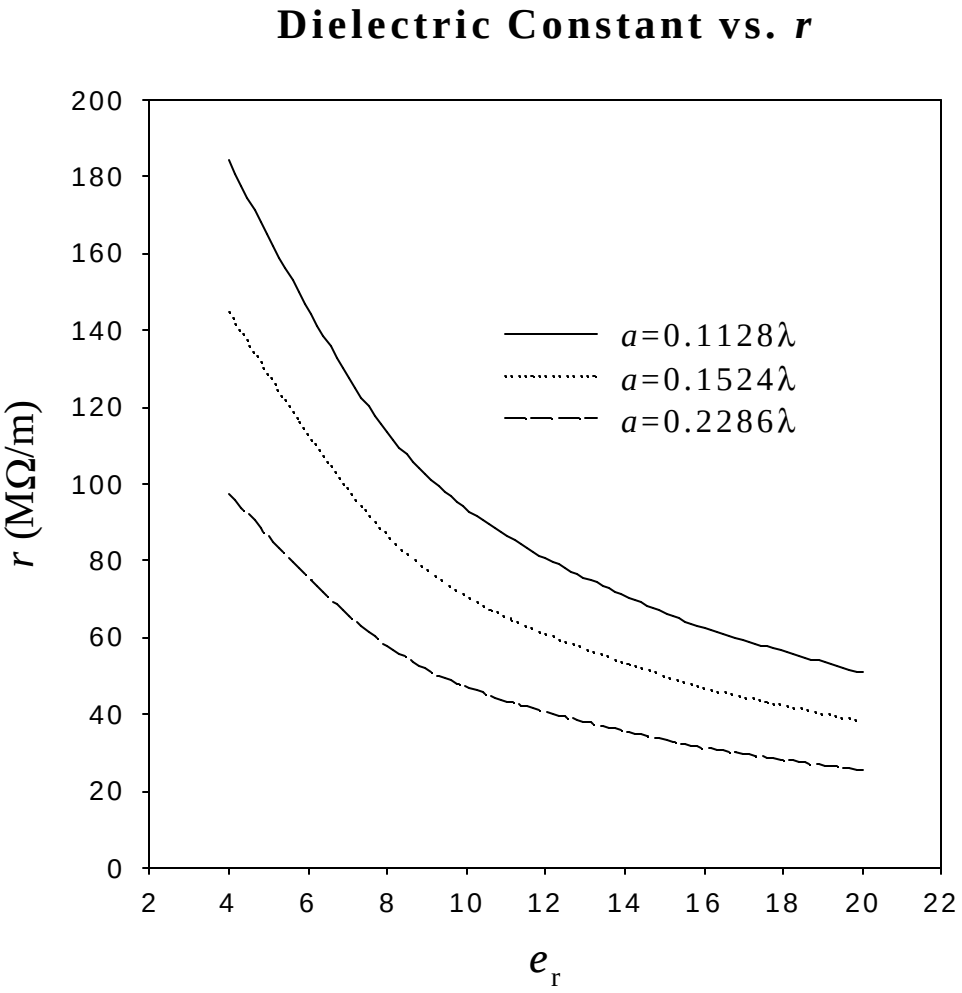

Figure 2.19 The Dielectric Constant versus the Shunt Impedance per Unit Length of the Dielectric Loaded Acceleration Structure, with the Various Beam Aperture Radius a. Here the wavelength l=26.242 mm. For a given beam aperture radius and a dielectric constant, the outer radius b must be adjusted accordingly to have the phase velocity of TM_{01} mode equal to the speed of light c.

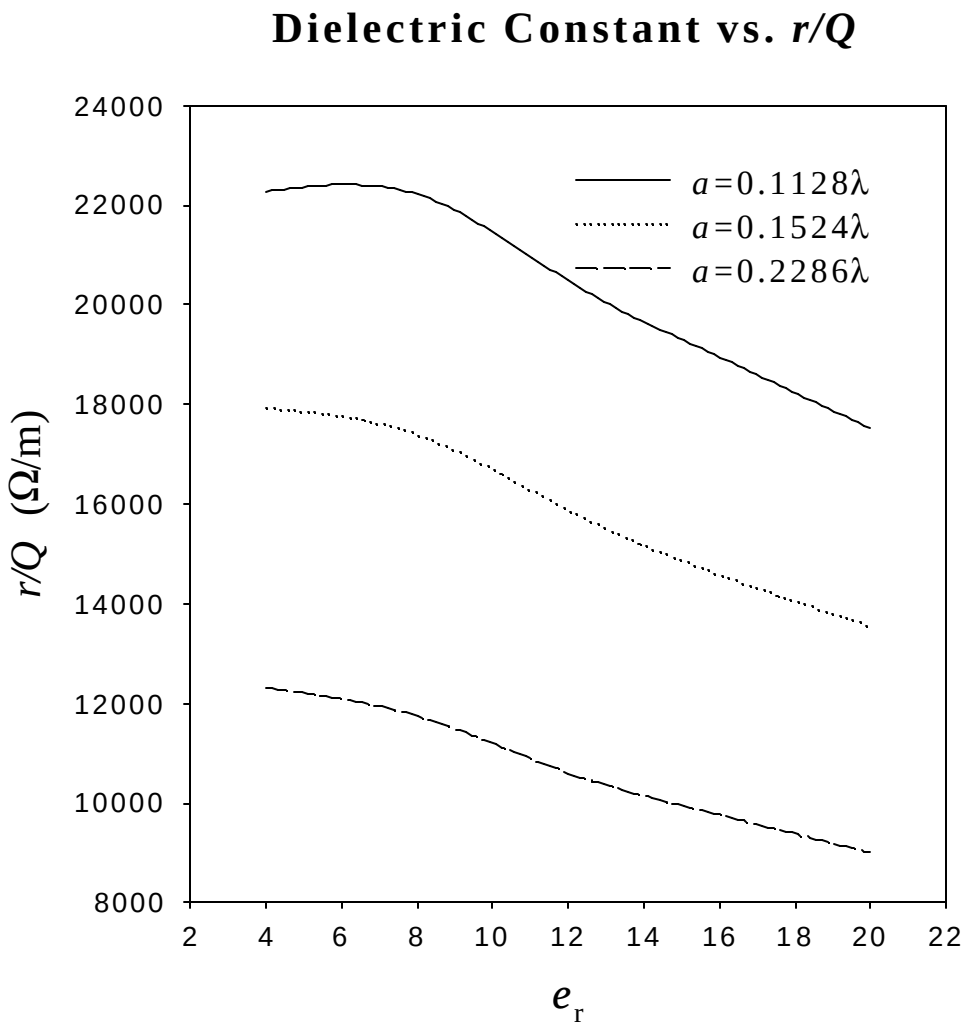

Figure 2.20 The Dielectric Constant versus *r/Q* of the Dielectric Loaded Acceleration Structure with the Various Beam Aperture Radius *a*. Here the wavelength l=26.242 mm. For given beam hole radius and dielectric constant, the outer radius *b* must be adjusted accordingly to have the phase velocity of the TM_{01} mode equal to the speed of light *c*.

2.3 Design a Dielectric Loaded Accelerator

The advantages and disadvantages of accelerating structure based on dielectric-lined circular waveguides have been discussed in the previous sections. However, the following fundamental issues have to be investigated before a very high gradient dielectric-loaded accelerator can be realized:

— Dielectric breakdown: Because the amplitude of the peak surface electric field in the dielectric-lined circular waveguides is very small, the constraint of the achievable acceleration gradient is the dielectric breakdown limit. The breakdown limits of low loss dielectric ceramics to a large extent are still unknown, especially when the ceramics are subject to a very high power RF pulse, in ultra-high vacuum, and at X-band or higher frequency bands. If such limit can reach about 70MV/m, it will certainly make a dielectric loaded accelerating structure a potential alternative to conventional metallic structures for the next generation linear collider.

— Joule heating: The heating caused by the power dissipation increases the temperature of the ceramic. Because the accelerating structure will be operated with very high RF power, the temperature is expected to be extremely high. It is still largely unknown how much the dielectric properties of the ceramic change at such high temperatures. Data on heating effects on the ceramic are scarse, since it is difficult to create the environment required for such measurement in normal laboratory conditions.

— Accumulation of surface charges on the dielectric: When particle beams pass through the beam hole, a small portion of the particles may hit the dielectric wall. If these charged particles accumulate on the surface of the dielectric, the strong transverse forces caused by them can result in beam break up.

— Absorption of gases in the dielectric: A dielectric ceramic is to a certain extent a porous material. If a small amount of gas is trapped in such dielectric, the dielectric loaded structure may not be able to achieve the ultra-high vacuum, which is necessary for high power testing. Whether the dielectric loaded structure is capable of supporting ultra-high vacuum environment is an important aspect. Moreover, how the vacuum properties vary under high power RF is also needed investigation.

— Dimensional tolerances: The sensitivities of the desired accelerator parameters to the variation of geometric parameters determine how tight the tolerances should be required in fabrication. The experimental investigation should be carried out to study this issue.

Therefore, experimental investigations on such dielectric loaded accelerating structures are necessary to answer these fundamental questions. One X-band accelerating structure using a dielectric-lined waveguide has been developed as the first step of conducting such high power experiments. The TM_{01} mode's group velocity of the developed structure was expected in the neighborhood of 0.05*c*, which is a typical value of the group velocity in the NLC structure design. Table 2.1 shows the geometric parameters and accelerator parameters of the dielectric loaded accelerating structure. The high power

experiment of the X-band dielectric loaded accelerating structure was originally planned at Stanford Linear Accelerator Center (SLAC), Stanford University, California, because SLAC's X-band klystron was the only suitable RF source at that time. As mentioned earlier, since X-band high power circulators or isolators are not available to handle the reflected RF power from the accelerating structure to the RF source, the testing accelerating structure must use the traveling-wave operation. The schematic drawing of a traveling-wave accelerating structure based on dielectric-lined waveguide is shown in Figure 2.21. The RF power is coupled in from the input port, and taken out from the output port. For a given RF power, the reflection at the input port must be minimized to protect the RF source from arcing damage, and to have as much as possible RF power fed in the accelerating structure. The latter is very important for the overall acceleration efficiency in term of the total power needed. Therefore, the efficient coupling between the input or output waveguide and the dielectric-lined accelerating structure is essential.

Table 2.1 The Parameters Of The Designed Dielectric Loaded Traveling-wave Acceleration Structure

Frequency	***a* (mm)**	***b* (mm)**	e_r	***r* (M**W **/m)**	***Q***	***r/Q* (**W **/m)**	v_g **(*c*)**
11.424 GHz	2.96	4.53	20	50.8	2903.8	17495.6	0.054

However, how to achieve such efficient coupling was proved as one major engineering challenge in the construction of such testing X-band dielectric loaded accelerating structure. The X-band SLAC klystron uses the standard WR-90 rectangular waveguide as the output waveguide, whose inner dimension is about 23mm wide. In the meanwhile, the inner diameter of the dielectric-lined waveguide that satisfies the requirements on group

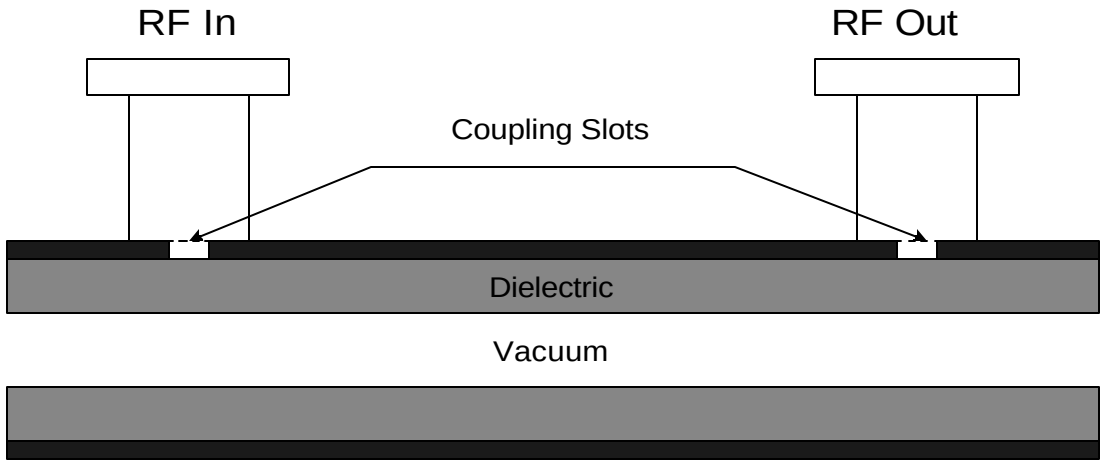

Figure 2.21 The Schematic Drawing of an Externally Powered Traveling-wave Dielectric Loaded Accelerator

velocity and other accelerator parameters is about 9 mm. Figure 2.22 illustrates, to scale, such large difference between the two waveguide dimensions. The consequence of such configuration is that the coupling slot cannot be opened large enough to achieve the desired efficient coupling. From the standpoint of equivalent circuit, the coupling between the input waveguide and the traveling-wave accelerating structure is indeed the impedance matching of two different waveguides with different waveguide modes, respectively [53]. Nevertheless, the classic impedance matching techniques, such as single-stub and double-stub methods, are difficult to be applied in accelerators, because accelerating structures must be able to handle ultra-high vacuum, and this makes tunable implementations very difficult and expensive. At the same time, such configurations can have very strong surface electric field at the tuning stubs, which are susceptible to arcing damage under high RF power. Thus other schemes should be studies. After intense experimental studies, one new configuration, which is a combination of a side coupled iris and a tapered ceramic section near the coupling iris, has been developed. The principle behind such scheme is that tapered waveguide sections are good impedance transformers between two different transmission lines. More than 90 percent power coupling between the input waveguide and the designed X-band dielectric accelerating structure was demonstrated in the bench measurement using such coupling scheme [25]. The coupling configuration is illustrated in Figure 2.23.

The wave coupling technique employed here should be studied thoroughly for the development of dielectric loaded accelerators. However, to analytically study the coupling problem of such a complicated waveguide junction is very difficult. Furthermore, there is

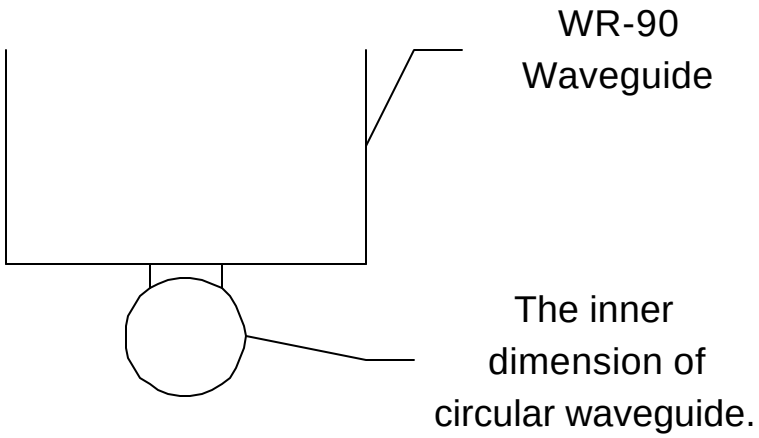

Figure 2.22 The In-scale Drawing of the Cross-section of the Junction between WR-90 Waveguide and the Dielectric-lined Circular Waveguide Whose Geometric Parameters are Shown in Table 2.1

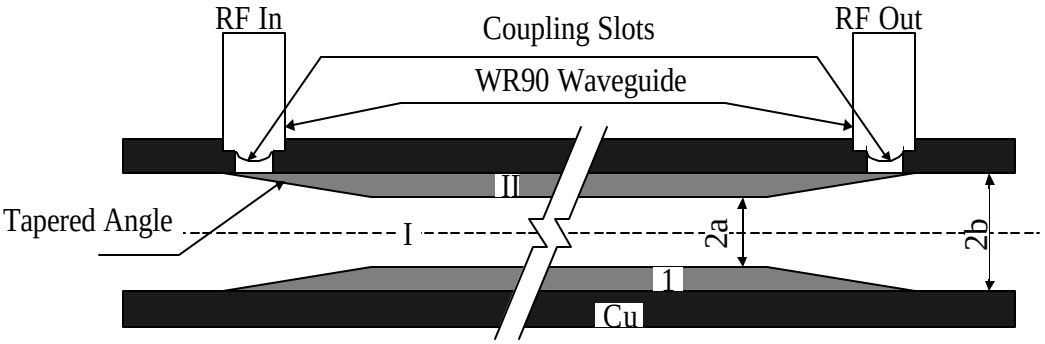

Figure 2.23 The Schematic Drawing of a Traveling-wave Dielectric Loaded Accelerator and the Efficient Coupling Configuration. Region I is vacuum, region II is dielectric.

not a general method that can be applied for all types of waveguide junctions. A simple analysis of such coupling configuration will be discussed in Chapter 4. Some MAFIA simulation results of such waveguide junction with actual geometric parameters are also presented. As mentioned earlier, the dielectric-lined waveguide used for such accelerating structure is able to support multiple propagating waveguide modes. Whether the desired TM_{01} mode is excited as the dominant mode using such coupling technique will be substantiated by the experimental results of the AWA step-up transformer [36]. In the next chapter, the fabrication, bench measurement and ultra-high vacuum testing of the X-band dielectric loaded accelerating structure will be introduced.

CHAPTER III

FABRICATION AND TESTING OF THE X-BAND DIELECTRIC LOADED ACCELERATING STRUCTURE

3.1 Fabrication and Bench Testing

The properties of traveling-wave accelerating structures based on dielectric-lined waveguides have been discussed in the previous chapter. However, several fundamental issues concerning dielectric loaded acceleration structures must be investigated through experiments conducted with very high RF power in ultra-high vacuum conditions. The design for a dielectric loaded traveling-wave acceleration structure at 11.4GHz was presented in Table 2.1. The dielectric loaded accelerating structure has comparable group velocity and shunt impedance with the NLC structures [9, 10] that are based on conventional metallic iris-loaded structures. In addition to the determination of the geometric parameters, the engineering challenges in realizing an efficient RF power coupling of the testing structure were also discussed. The coupling scheme developed by the Argonne group was shown in Figure 2.23.

The parameters of the prototype accelerating structure constructed with 25 cm long ceramic are listed in Table 3.1. The ceramic dielectric is a compound of Mg-Ti oxide, which has nominal dielectric constant of 20. This material can be readily obtained from commercial vendors [31].

The RF coupling scheme employed is similar to the side-coupled method in conventional iris-loaded accelerating structures. Impedance matching through the coupling aperture is more difficult in the high dielectric constant case because the inner diameter of

Table 3.1 Dimensions and Physical Properties of the 11.4 GHz Dielectric Accelerator

Coefficient	Value
Material	MgTi
Dielectric Constant ε	20
Taper Angle	8°
Loss Tangent δ	10^{-4}
Inner Radius a	0.296 cm
Outer Radius b	0.453 cm
Frequency of the TM_{01} Mode (with $v_p = c$)	11.424 GHz
Frequency of the HEM_{11} Mode (with $v_p = c$)	9.96 GHz
Group Velocity v_g	0.054 c
Attenuation	4 dB/m
Power Required (10 MV/m gradient)	2.6 MW

the dielectric waveguide becomes much smaller than the inner width of the rectangular waveguide. In order to achieve efficient coupling, the ceramic section near the coupling iris is tapered to serve as an impedance transformer. The tapered angle was chosen to be 8° for initial convenience. Such tapered ceramic sections were machined using a custom-made diamond-coated mandrel. No other angles were tested, but the taper is assumed gradual enough. The optimized coupling between the rectangular waveguide and the dielectric-lined circular waveguide is governed by the interaction of two geometric factors: the dimension of the coupling aperture and the taper angle of the ceramic. Further engineering study of various tapered sections is very important, but it is beyond the immediate goals of the current research program.

The picture shown in Figure 3.1 displays the parts fabrication of the testing accelerating structure. The vacuum flanges for WR-90 waveguide sections were provided by the SLAC Klystron Department. Figure 3.2 and 3.3 show the assembly of the prototype accelerating structure viewed from different directions. The important bench measurement parameters are the reflection coefficient s_{11} at the input port and the transmission coefficient s_{21} between the input and output ports. The measurement configuration is shown in Figure 3.4.

The optimized coupling slot dimensions are 4.7 mm (axial) $\times$ 5.69 mm (transverse), which were arrived at through experiments. At the same time the relative position of the tapered dielectric section to the coupling slot is also a determining factor for the coupling. The measurements of such positions of the tapered dielectric sections at the input and output ports are critical to the choice of the total length of ceramics needed for the

Figure 3.1 The Parts Display Of The 11.4GHz Testing Dielectric Loaded Traveling-wave Accelerating Structure

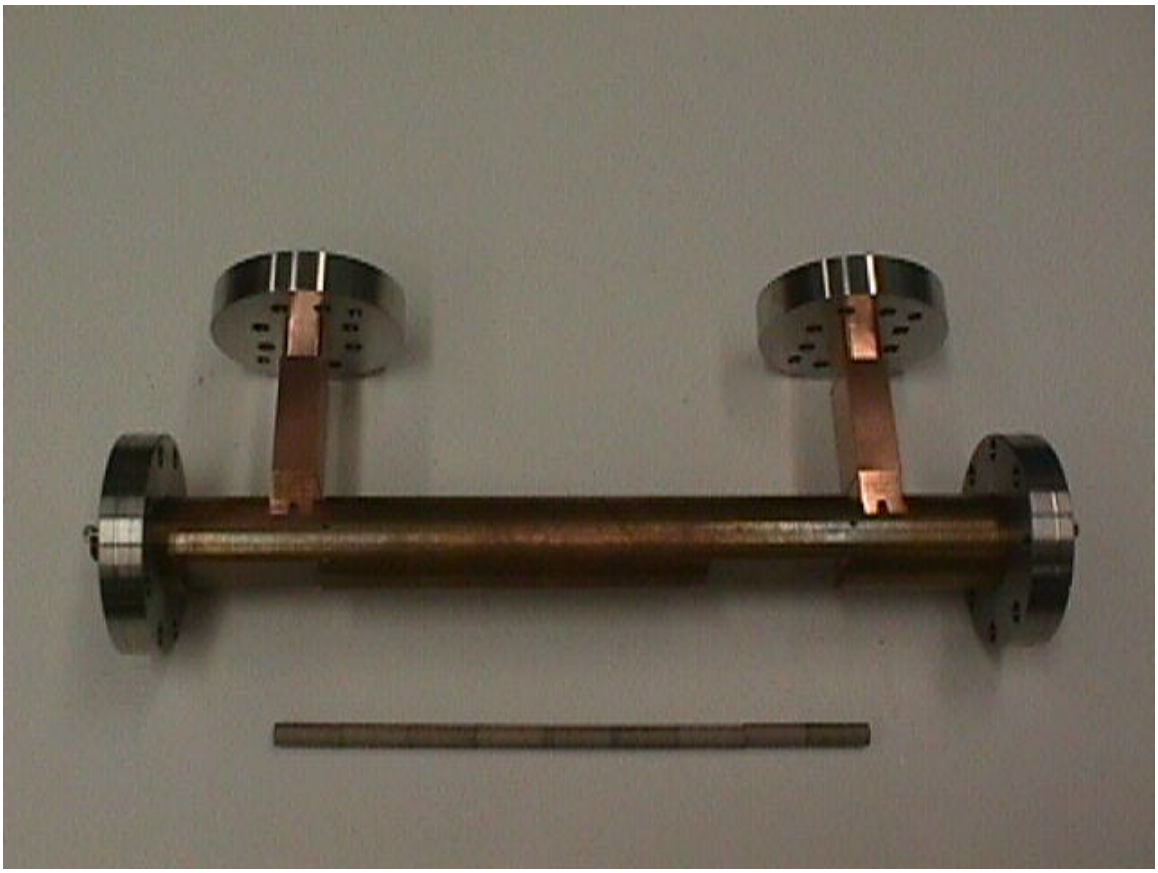

Figure 3.2 The Assembly Of The Dielectric Loaded Accelerating Structure (I)

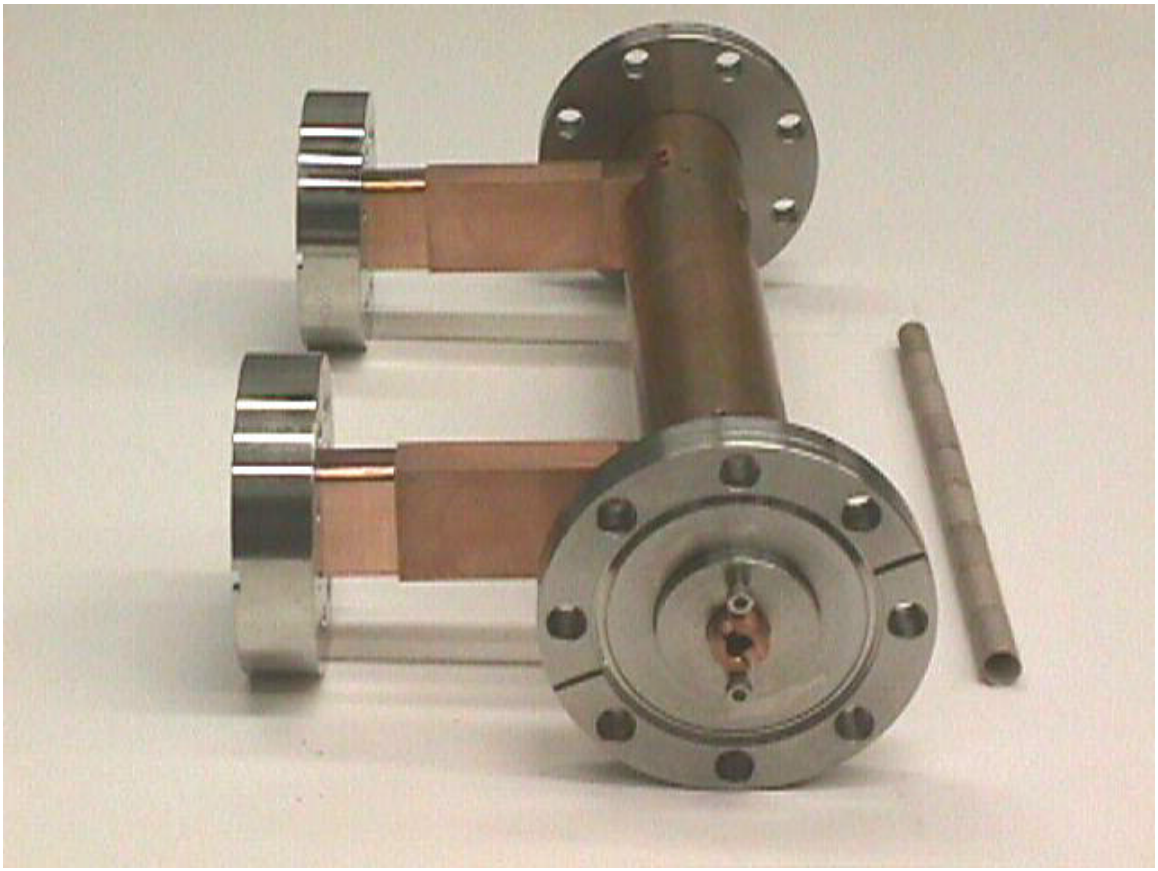

Figure 3.3 The Assembly Of The Dielectric Loaded Accelerating Structure (II)

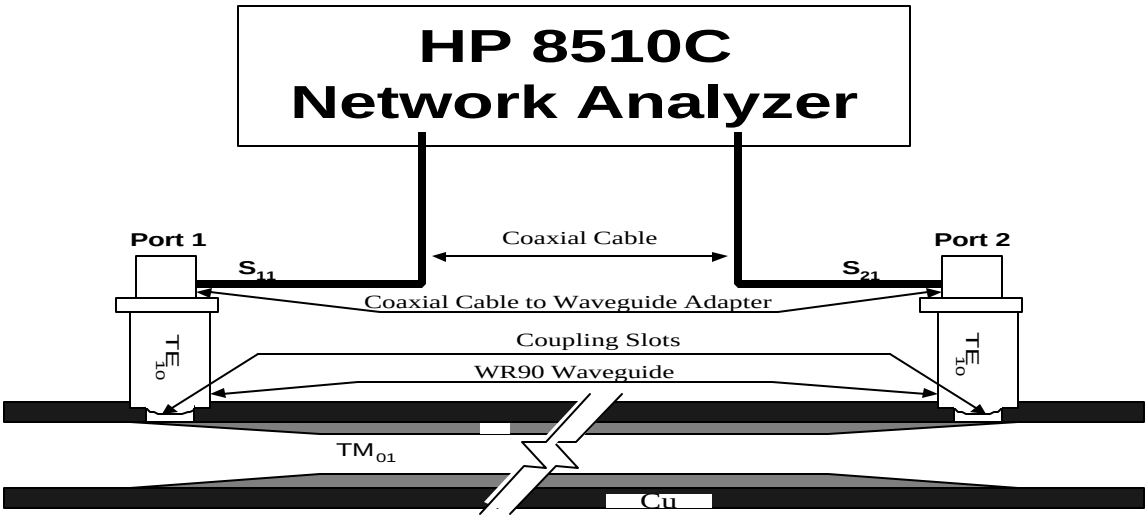

Figure 3.4 The Configuration of Bench Measurement for the Dielectric Loaded Accelerating Structure

optimized coupling, if the positions of the two coupling apertures are fixed. A procedure was designed to measure the optimal position of the tapered dielectric section. Figure 3.5 shows such measurement scheme. In this method, we use s_{11} measurement to optimize the coupling, equivalent to impedance matching, between the rectangular waveguide and the dielectric loaded circular waveguide. The microwave-absorbing cone functions as the matched loaded to the dielectric-lined waveguide. Thus there is no wave reflected from the other port. The reflection at the measured port is totally caused by the impedance mismatch at the corresponding waveguide junction. By adjusting the position of the ceramics, the optimized position of the tapered section can be found, for which s_{11} is minimum. Applying such a process to both coupling slots can lead to the required length of ceramic dielectric. Because of the slight dimensional differences in the tapered sections and the coupling apertures, both ports must be measured to find the optimal configuration.

Figure 3.6 is a picture of the actual bench measurement setup to test the dielectric loaded accelerating structure. Plots of the measured s_{21} and s_{11} with a frequency span of 100 MHz are shown in Figure 3.7 and 3.8, respectively. The maximum value of the transmission coefficient, s_{21} is -1.7 dB at 11.421 GHz. The reflection coefficient s_{11} at this frequency is less than -20dB. This means that less than 1 percent of RF power is reflected at the input port, and such minimized reflection makes the high RF power experiments possible.

3.2 Vacuum Testing

The vacuum techniques have significantly advanced since the first particle accelerator was constructed. It has been found in experiments that better vacuum conditions can lead

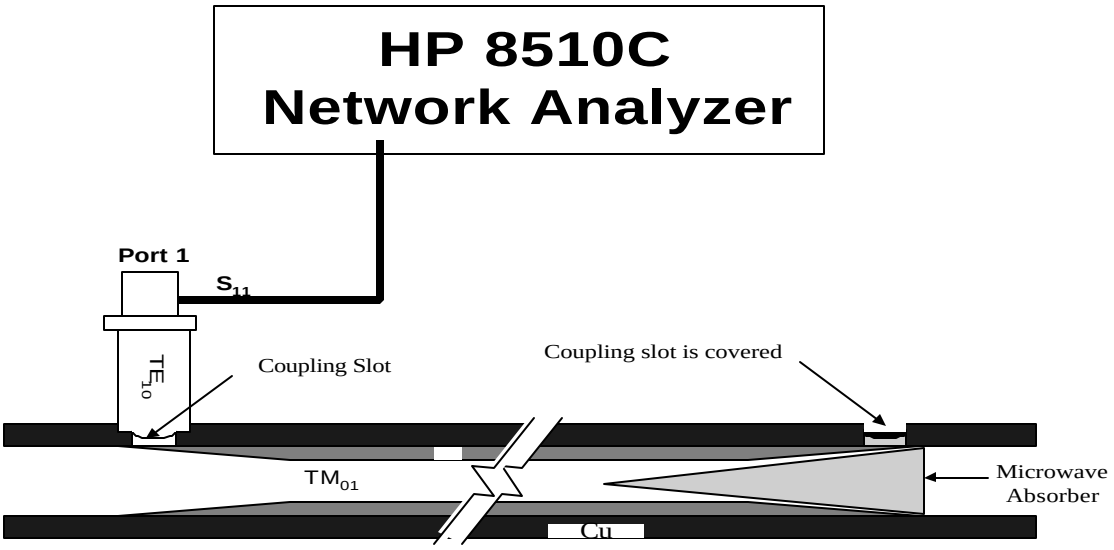

Figure 3.5 The Measurement Configuration to Find the Optimized Position of the Tapered Dielectric Section

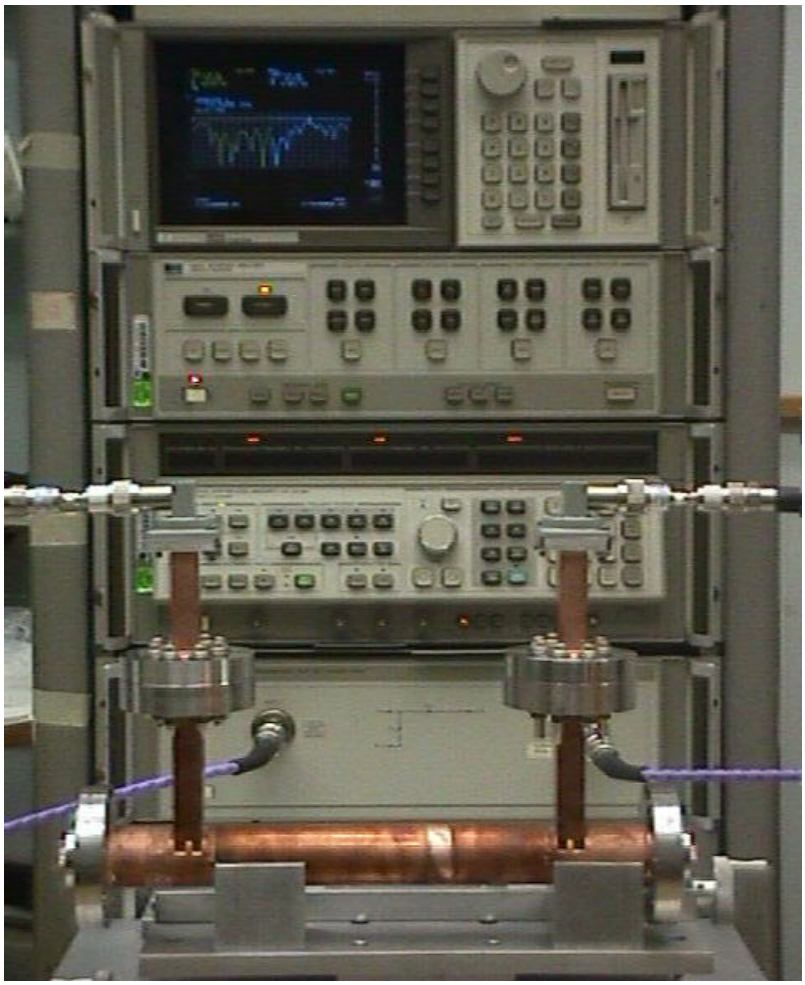

Figure 3.6 The Bench Measurement Setup of the 11.4 GHz Dielectric Loaded Accelerating Structure

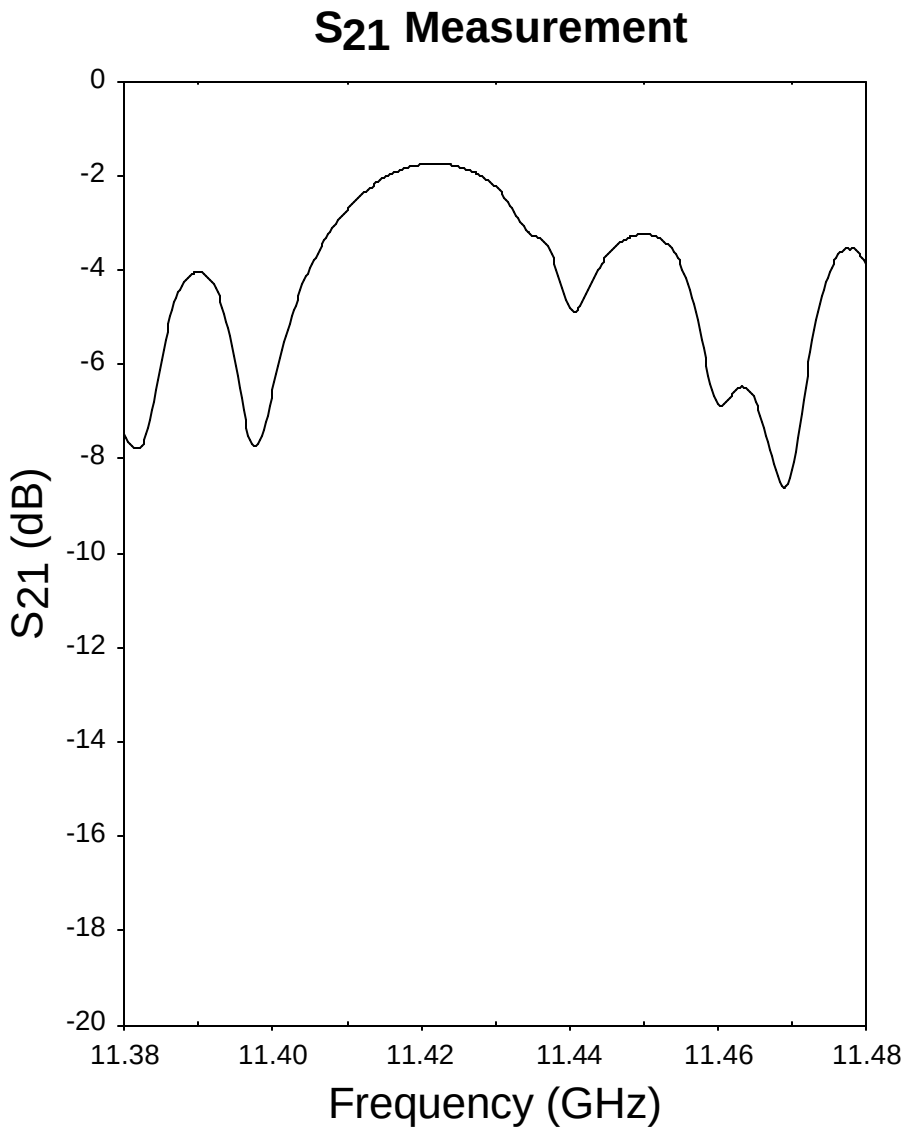

Figure 3.7 The s_{21} Measurement Obtained in the Bench Testing Shown in Figure 3.6

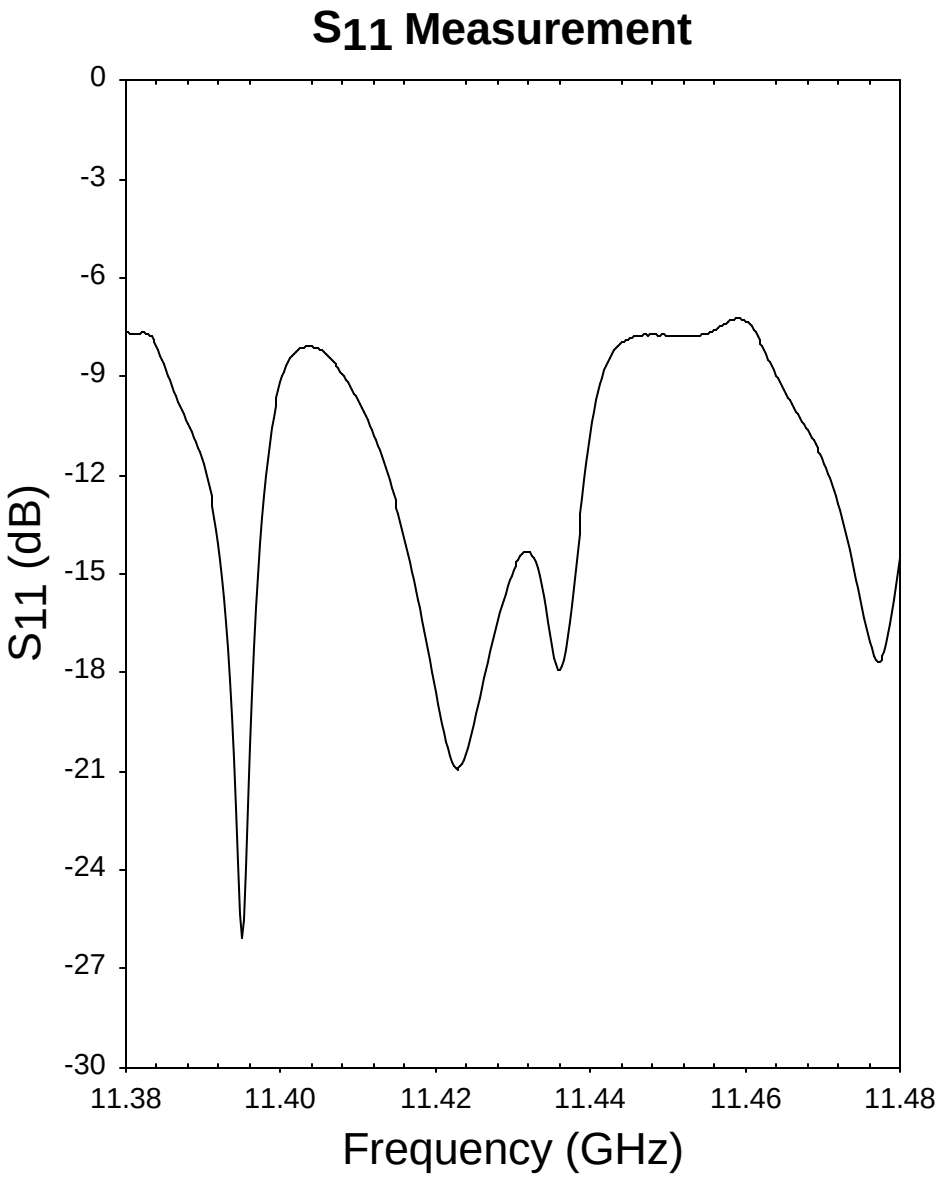

Figure 3.8 The s_{11} Measurement Obtained in the Bench Testing Shown in Figure 3.6

to higher breakdown limit. Therefore, an improvement in the vacuum in the accelerators will enhance the achievable accelerating gradient.

High RF power operation of the dielectric loaded accelerating structure requires that it be able to hold the ultra vacuum condition. If the vacuum condition is not sustained, the density of ions may be so high that breakdown will result. Thus the real breakdown limit of dielectric ceramic cannot be determined. This is a fundamental issue of any dielectric based accelerating structure. As mentioned earlier, dielectric ceramic is usually considered as a porous material, so that it can absorb gases and degrade the vacuum. An ultra-high vacuum testing system, shown in Figure 3.9, was built to test the dielectric loaded accelerator section. Such vacuum testing system consisted of a roughing pump, a turbo pump, an ion pump, and ion gauge meters. Figure 3.10 shows the pressure during a pump down exercise of the prototype dielectric loaded structure without vacuum baking-out. The corresponding pressure measurement of the same structure during high vacuum baking-out is shown in Figure 3.11. The result after vacuum baking-out is given in Figure 3.12. After one week of high vacuum baking-out at 150°C and one more week for pumping-out, the pressure level on the pump side indicated that 10^{-9} vacuum was achieved in such dielectric loaded structure, and no change of dielectric properties was observed. Figure 3.13 shows the vacuum measurement of the same structure without loading dielectric after vacuum baking-out. Based on these, we may arrive at the following conclusions:

— Loading with dielectric ceramic does not necessarily result in degradation of the vacuum.

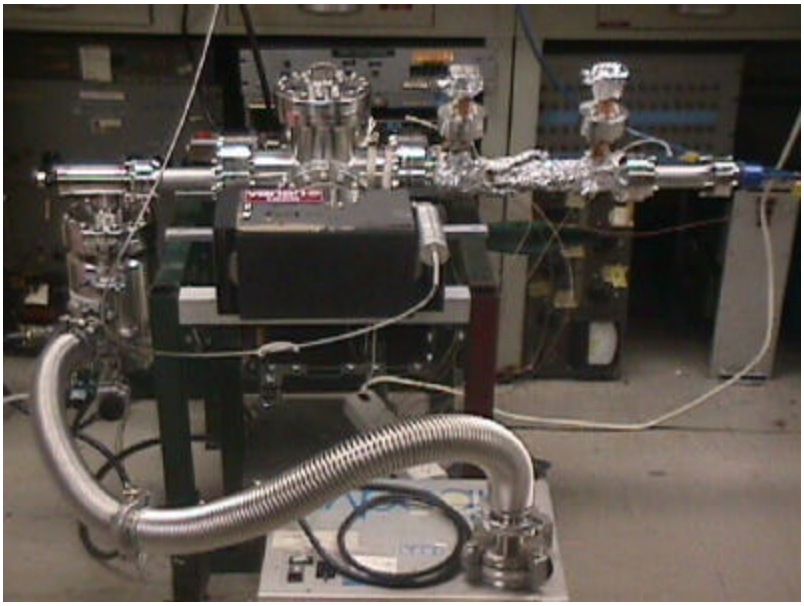

Figure 3.9 The Vacuum Testing System for the Dielectric Loaded Accelerating Structure

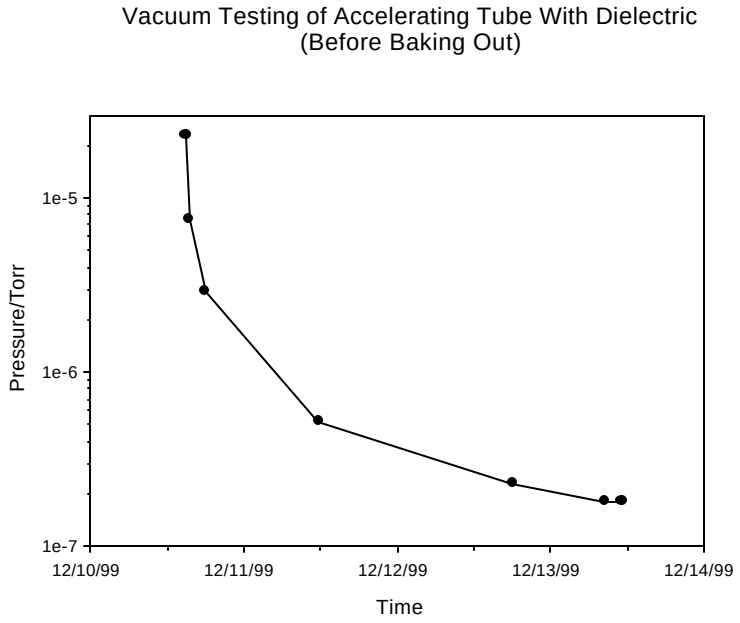

Figure 3.10 The Pressure in the Dielectric Loaded Structure before Vacuum Baking-out

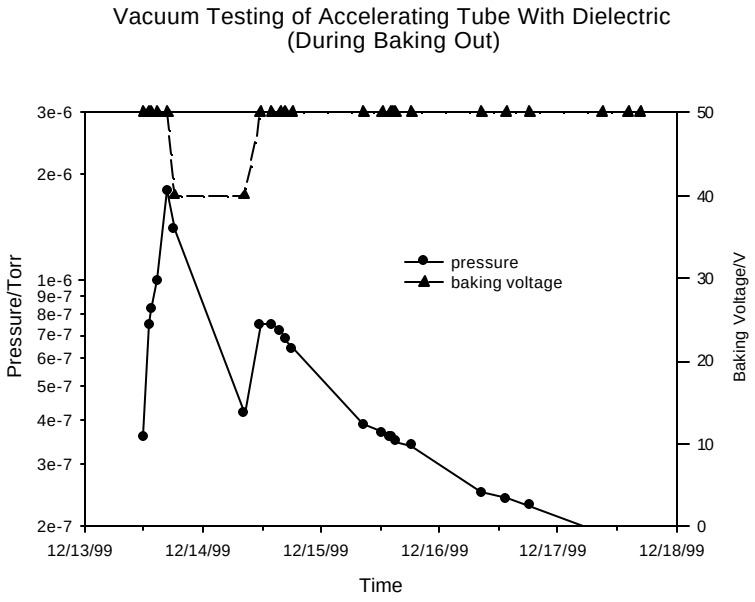

Figure 3.11 The Pressure in the Dielectric Loaded Accelerating Structure during Vacuum Baking-out

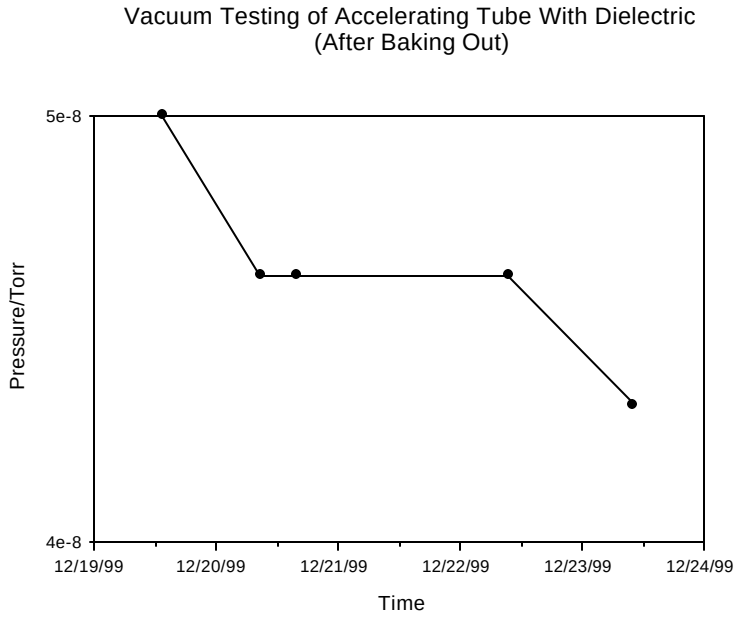

Figure 3.12 The Pressure in the Dielectric Loaded Accelerating Structure after Vacuum Baking-out

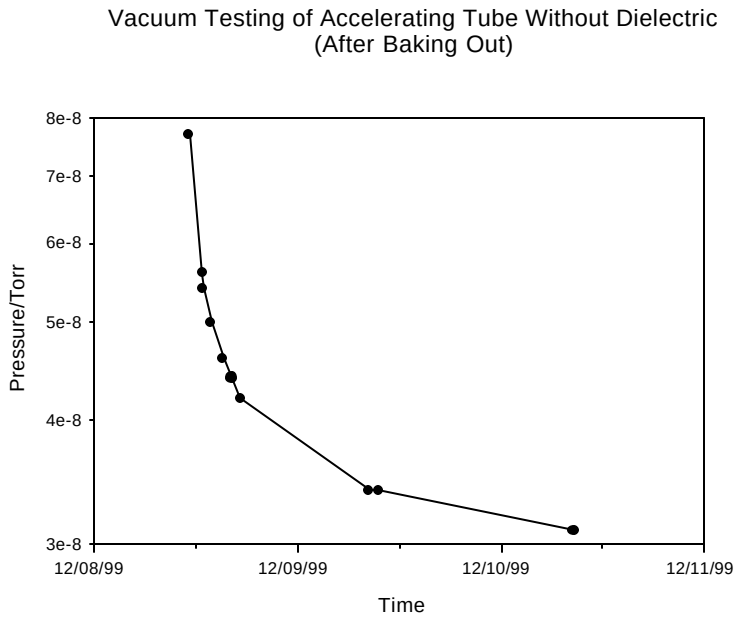

Figure 3.13 The Pressure in the Accelerating Structure without Loading Dielectric Ceramics

— High temperature vacuum baking-out can improve the vacuum by at least a factor of 10, and this procedure does not lead to any change of the dielectric properties.

Only one ion pump was used in such vacuum testing system, and it pumped through the small channel of the dielectric loaded accelerating structure, while two ion pumps will be mounted at the both ends of the accelerator section in actual operation. Thus better vacuum quality can be expected from the actual experimental setup. This ultra-high vacuum testing gave the promising proof that the dielectric loaded accelerating structure is capable of satisfying the requirements on vacuum for high power acceleration operation. However, the vacuum properties with high power RF pulses present should be further studied in the actual experiments.

3.3 High Power Experiment

The eventual goal of a high power testing on the prototype dielectric accelerator section is to investigate some fundamental issues such as RF breakdown limits, Joule heating, and vacuum properties of the dielectric loaded structure under high power RF. With 100 MW X-band RF power available at SLAC, we can test this structure at a 60 MV/m acceleration gradient, comparable to the desired acceleration gradient for the NLC structures [9, 10]. Figure 3.14 is the drawing of the high power experimental setup. The assembly for the high power experiment is shown in Figure 3.15. If RF breakdown happens in the dielectric loaded waveguide, it can be observed from the viewports, shown in Figure 3.14 and 3.15. The Faraday Cup is used to measure the dark current, if any.

The assembled testing structure shown in Figure 3.15 was shipped to SLAC for installation in June 2000. However, the delicate fastening parts holding the dielectric

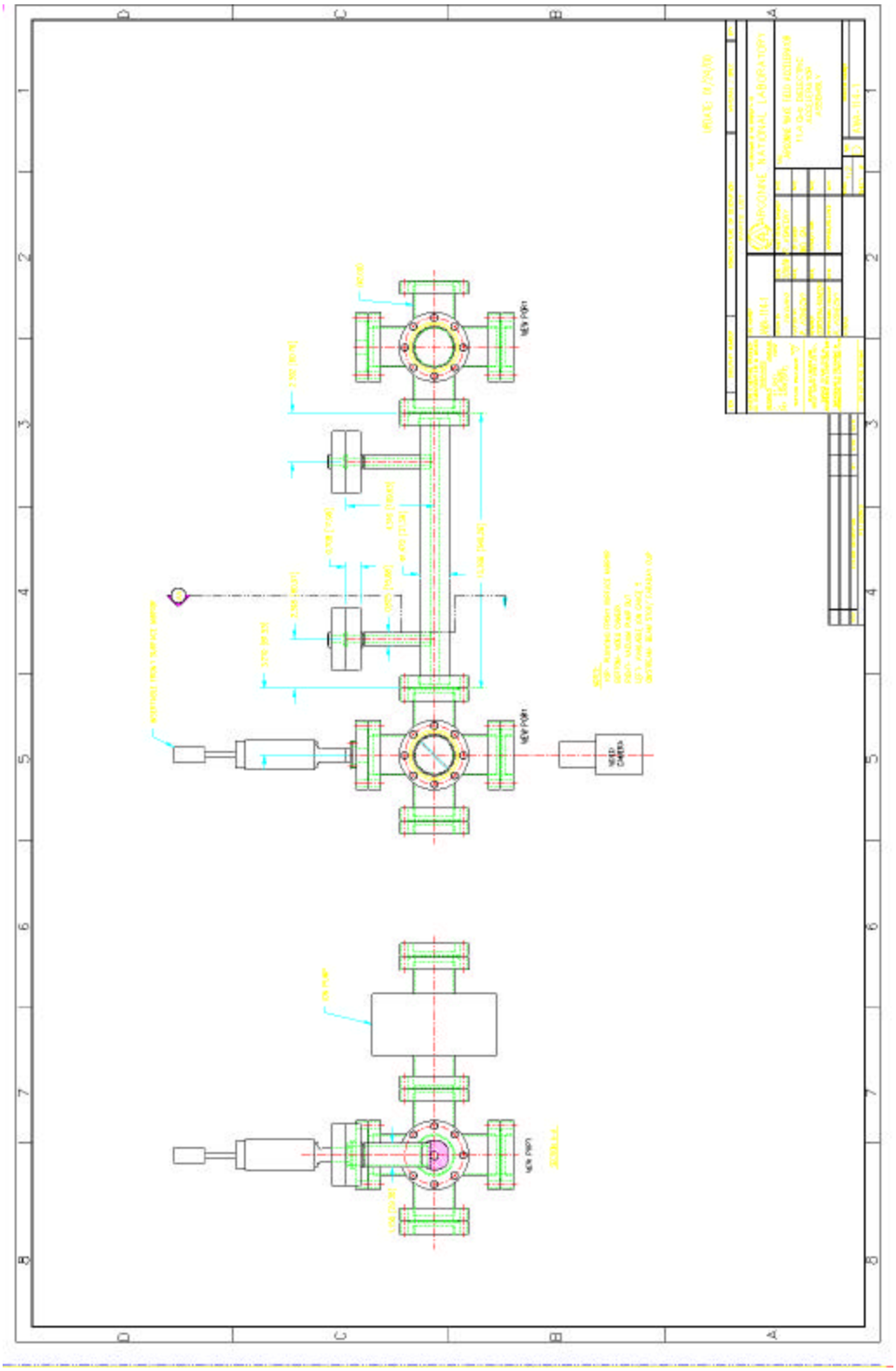

Figure 3.14 The Drawing of the High Power Experiment Setup of the Dielectric Loaded Accelerating Structure

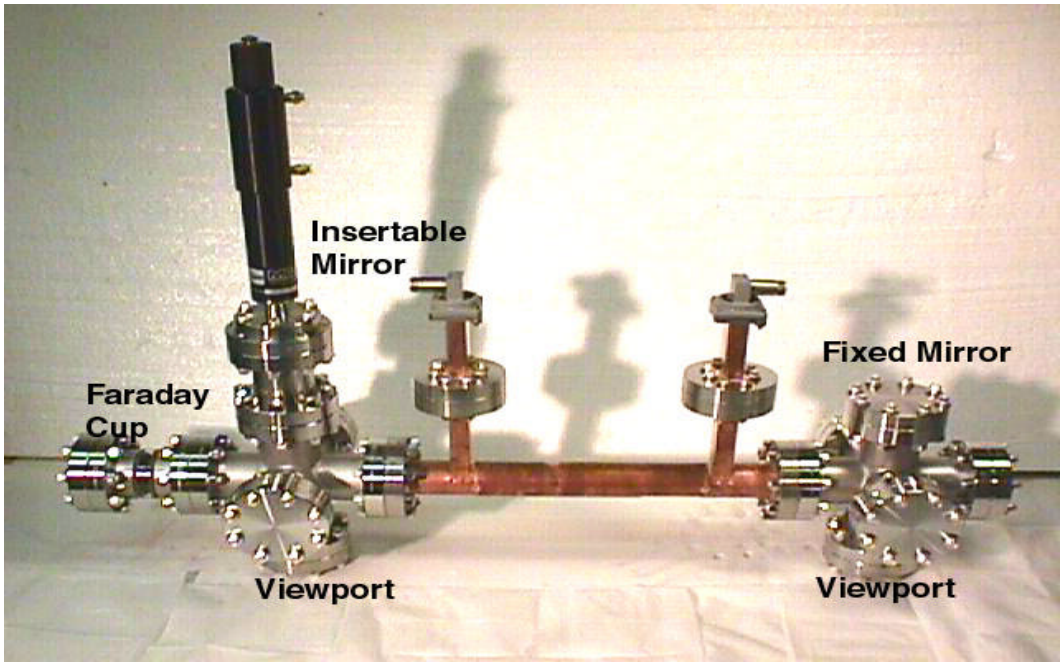

Figure 3.15 The Assembly of the High Power Experiment Setup

ceramics in position were not able to stand the vibration during the shipping and handling process. The transmission coefficient from port to port was changed seriously. Mechanical improvements on the fastening parts have been put in place, and readjustment on this dielectric loaded accelerator has also been completed.

The schedule of the high power experiment at SLAC is currently contingent upon when the X-band klystron facility is available. At the same time the preparation of a high power testing on this prototype X-band dielectric loaded accelerator is underway at Navy Research Laboratory (NRL) [54]. A testing facility for this experiment is currently under construction, and the Magnicon at NRL will be ready to provide 11.4 GHz RF power of 56 MW soon [55]. The NRL Magnicon possesses the same WR-90 waveguide and SLAC-style vacuum flange at the output port. Thus the dielectric loaded accelerator section can be easily installed and tested at NRL. The fundamental issues concerning the dielectric loaded accelerator will be studied in these imminent experiments at NRL and SLAC.

CHAPTER IV

ANALYSIS OF THE COUPLING SCHEME

4.1 Calculation Of The Coupling Scheme

The importance of efficient wave coupling to traveling-wave dielectric loaded accelerators has been discussed in the previous chapters. Efficient coupling must be achieved to limit the reflected power from the accelerating structure to the RF sources. It is also necessary to prevent deterioration of the overall power efficiency of the accelerator and to avoid arcing damage to the RF sources. The widely used method of protection is the installation of a ferrite device called circulator to isolate the RF source, such as the klystron, from the power reflected from the load impedance. However, circulators that can be used for peak RF power of over 100 MW are unavailable at X-band. Thus, efficient coupling is very important to the dielectric loaded traveling-wave accelerating structure.

The coupling scheme discussed in Chapter 2 has demonstrated good impedance matching between the rectangular waveguide and the dielectric-lined circular waveguide. The reflected power is limited to less than one percent of the input RF power. The wave-coupling problem is equivalent to the impedance matching between two transmission lines that have different cross sections and operate in different modes. How the desired TM_{01} mode is excited in the dielectric-lined circular waveguide using the given coupling scheme should be studied. Because dielectric-lined circular waveguides can support multiple propagating modes, when the operating mode is TM_{01}, the presence of other modes such as the HEM_{11} mode needs to be determined and eliminated.

The analysis of the coupling scheme is a very complicated problem. There is no universal method applicable to any coupling structure, even though this problem has been intensively studied for many years. Some widely used analytic and numerical methods used in the analysis of wave coupling will be briefly described in the following.

4.1.1 Bethe's Theory. Bethe [56-58] has developed a general perturbation technique for calculating the scattering of power by small apertures connecting one transmission line to another. The theory is applicable to the case of two transmission lines with different cross sections and operating in different modes. A condition of this theory is that it applies only to infinitesimally thin apertures whose dimensions are small in term of the operating wavelength. These apertures should be located far from any corners in a transmission-line wall whose radius of curvature is large compared to the wavelength. Collin [59] derived some of Bethe's results using a different approach. In Bethe's theory, a side coupling iris on a waeguide is assumed small so that it can be described by three lumped constants, namely two magnetic and one electrical polarizability M_1, M_2 and P. M_1 and M_2 are the magnetic polarizabilities in the two principal directions of the iris, and P is the electric polarizability. These constants determine the effect of the iris in any waveguide or cavity. When an electromagnetic field falls on an iris, the iris may be considered as a secondary source of radiation. The iris is then equivalent to an induced magnetic dipole moment and an induced electric dipole moment. Such magnetic dipole is composed of two components that are equal to the products of the tangential magnetic fields in the two principal directions and the

corresponding magnetic polarizabilities. Meanwhile, the electric dipole is the product of the normal electric field at the iris and the electric polarizability.

In the coupling scheme shown in Figure 2.23, there is only induced magnetic dipole moment, because the operating mode in rectangular waveguide is TE_{10}. According to Bethe's theory, the excited mode in the secondary dielectric-lined waveguide is thus expected as TM_{01} mode that has the tangential magnetic field component parallel to the magnetic dipole.

Bethe's theory can be applied to relatively simple coupling structures. However, to obtain the analytical solution based on this theory is not always straightforward. First, the premise of such approximation is that a coupling iris should be qualified as a small aperture without thickness. The thickness of the coupling aperture is not negligible in the practical cases, and the aperture may not be considered small in term of the operating wavelength. In some cases, the approximation corrections for large aperture can be added to Bethe's coupling formula, and the attenuation of transmission through a thick iris can also be corrected [53, 60]. Moreover, the prolarizabilities are only valid as the properties of a small coupling iris. In the junction of WR-90 rectangular waveguide and the dielectric-lined circular waveguide, the coupling aperture cannot be assumed to be small with respect to the dimensions of dielectric loaded waveguide. Further corrections to the formula are needed.

The prolarizabilities of the apertures with arbitrary shapes are in general difficult to obtain analytically. In the practical applications, the static field solutions are used instead.

Cohn has developed an electrolytic-tank method for measuring polarizabilities of arbitrary-shaped apertures that are difficult to calculate theoretically [61]. Nevertheless, such approximations are valid to small apertures. Gluckstern [62] developed a method to obtain the electric and magnetic polarizabilities of arbitrary-shaped aperture in a thin screen by solving the electrostatic and magnetrostatic problems. However, it is important to notice that the generality of this method has been challenged [63], and its results for rectangular apertures in a thin screen have 12-15% discrepancy, comparing with the available calculations and measurements [64].

Another difficulty is that Bethe's method needs the solutions of the normal modes in the secondary waveguide. Unfortunately, the analytical expressions of the normal modes in the tapered section would be too complicated to be arrived at, if such expressions exist.

4.1.2 Moment Method. There are also some recent analyses of electromagnetic fields radiated from rectangular apertures on the walls of waveguides [65-67], and of a junction of two waveguides coupled through a rectangular aperture [68-71]. Such analyses are based on the moment method formulation [72], and provide good agreement between numerical results and experimental measurements within small bandwidth and limitations of variations of aperture's dimensions. The difficult part of this method is to construct the Green's function in the secondary waveguide. Whether the Green's function in the dielectric-lined waveguide with the tapered section can be obtained or not is theoretically uncertain. Thus the applicability of the moment method to analyze the coupling scheme needs to be verified.

4.1.3 MAFIA Simulation (Using FDTD Method). From the above discussion, we can see the reasons why it is so difficult to calculate the coupling structure by the widely used techniques. The two methods discussed earlier are frequency-domain techniques. Now let us briefly visit the Cartesian mesh finite-difference time-domain (FDTD) method. This method was first described by K. Yee in 1966 [73], and has been found useful in numerous applications in electromagnetic radiation, scattering, and coupling. Several key attributes combine to make the FDTD method a powerful tool [74]. First is the method's simplicity; Maxwell's equations in differential form are discretized in space and time in a straightforward manner. Second, since the method tracks the time-varying fields throughout a volume of space, FDTD results in as a good scientific visualization method. These, in turn, provide the user with excellent physical insights on the behavior of electromagnetic fields. Finally, the geometric flexibility of the method permits the solution of a wide variety of radiation, scattering, and coupling problems.

The implementation of an electromagnetic solving program using FDTD is a large-scale project, and it is certainly beyond the scope of the current research program. Fortunately, we have access to MAFIA, one commercial electromagnetic field solver. The T3 module of MAFIA is a well-known 3-dimensional solver based on an alternate derivation of the FDTD method, which can be obtained by approximating the integral form of Maxwell's curl equations (Ampere's and Faraday's laws) [74].

We calculated a junction of WR-90 waveguide and dielectric-lined circular waveguide using MAFIA. The geometric parameters of such dielectric-lined waveguide and the tapered section are the same as those given in Table 2.1, and the dimensions of the coupling

aperture are the same as the actual parameters. The input geometry of the calculated waveguide junction is shown in Figure 4.1. The electric field distribution obtained from the computation is also given in the same figure. In the calculation, the incident wave was in the TE_{10} mode launched from the rectangular waveguide port. The output port was in the dielectric-lined waveguide. The boundary conditions at such two waveguide ports were set as having matched load for all the propagating modes. Figure 4.1 shows that TM_{01}-like waveguide mode is excited inside the dielectric-lined circular wavguide.

Figure 4.2 shows the reflection coefficient s_{11} given by the simulation at the rectangular waveguide port. Such coefficient is the ratio of the voltage of the reflected wave to the voltage of input wave, and it is equivalent to about 1% input power reflected back at the input port. The center frequency of the pass-band is around 11.45 GHz. The transmission coefficient of the TE_{10} mode in the rectangular waveguide to the TM_{10} mode in the dielectric-lined waveguide is given in Figure 4.3. Figure 4.1 also shows the small amount of hybrid mode component existing. The plot of the transmission coefficient of the TE_{10} mode to the HEM_{11} mode is given in Figure 4.4. The MAFIA simulation on such waveguide junction did shed light on the mode excitation of the coupling scheme used in the testing dielectric-loaded accelerator. The hybrid mode component may be caused by the asymmetric coupling configuration. If multiple coupling slots are symmetrically configured, the hybrid mode may be significantly cancelled. However, the incident waves at all input ports must maintain the identical amplitude and phase, then it is too complicated to be used for this research program.

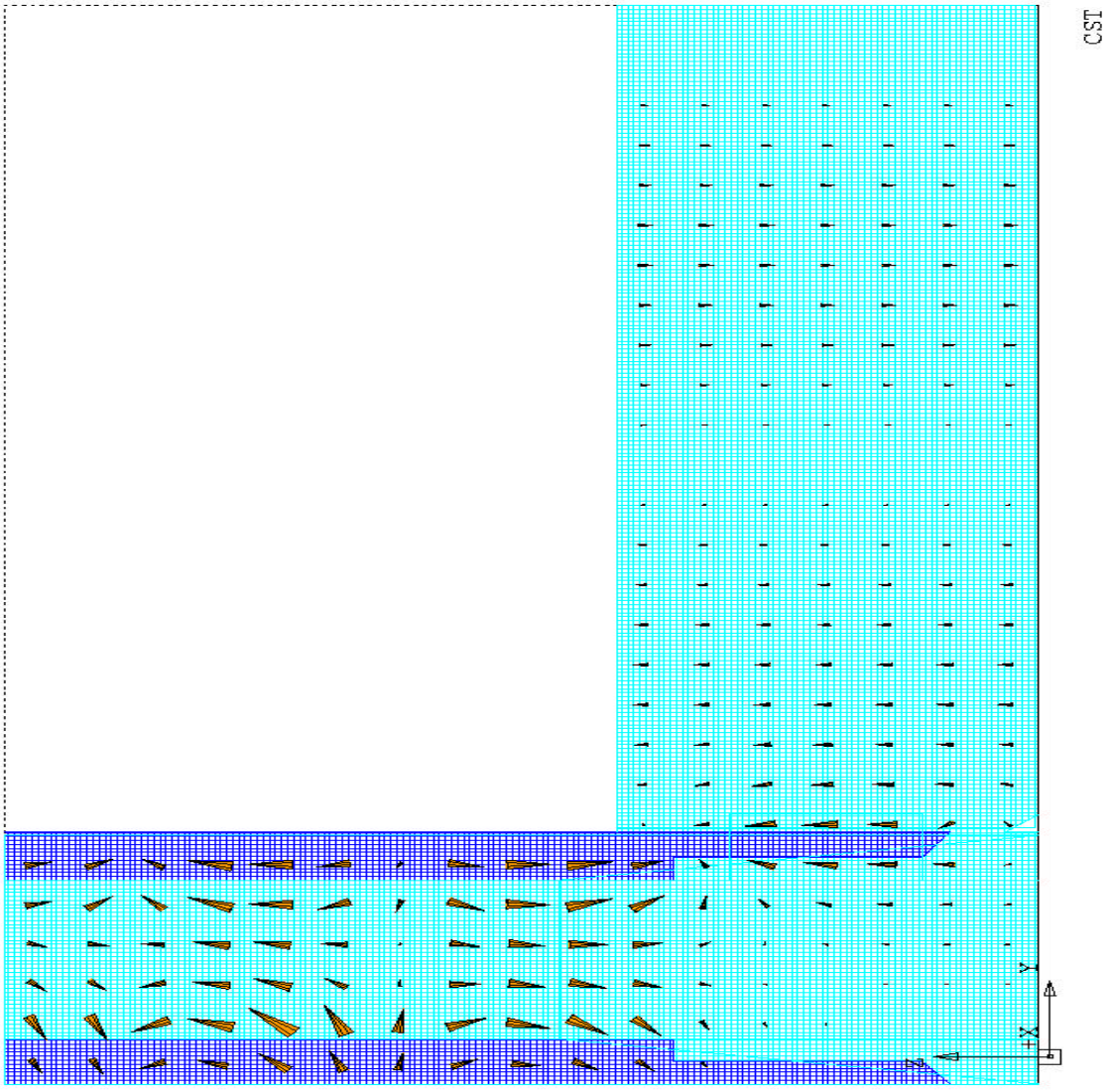

Figure 4.1 The Electric Field Distribution of the Junction of the Rectangular Waveguide and Dielectric-lined Waveguide

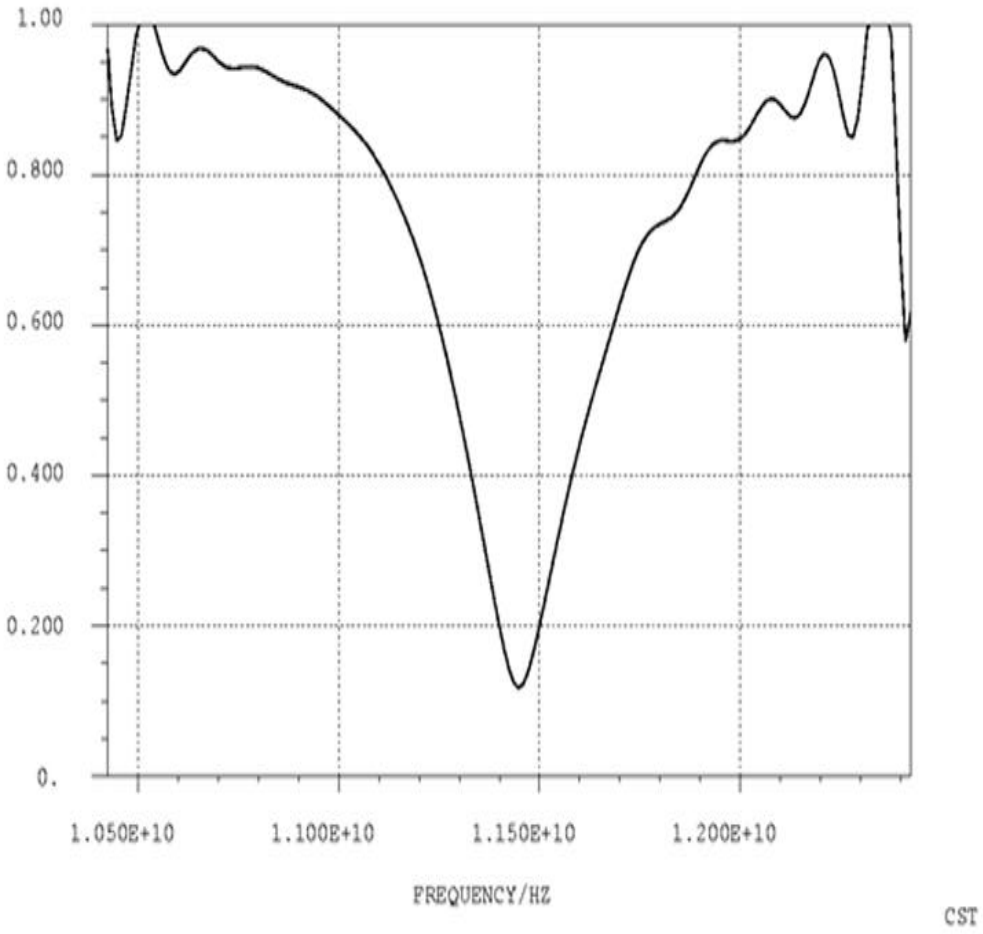

Figure 4.2 The Reflection Coefficient s_{11} at the Rectangular Waveguide Port

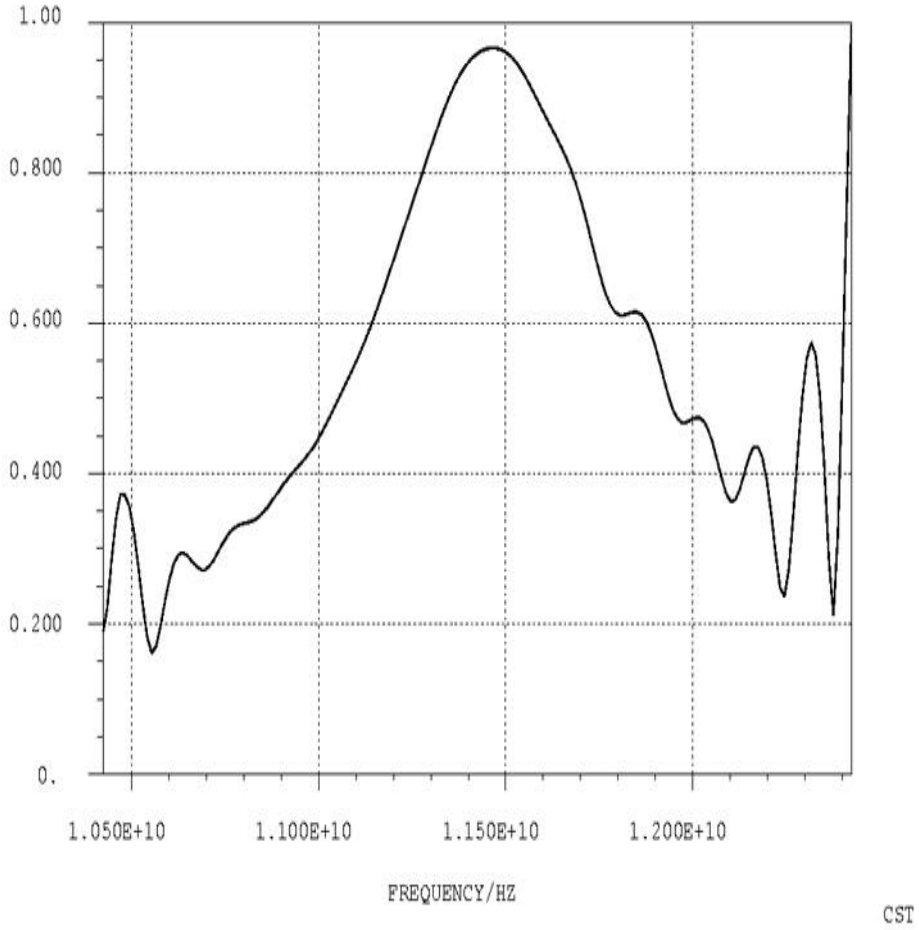

Figure 4.3 The Transmission Coefficient from the TE_{10} Mode to the TM_{01} Mode

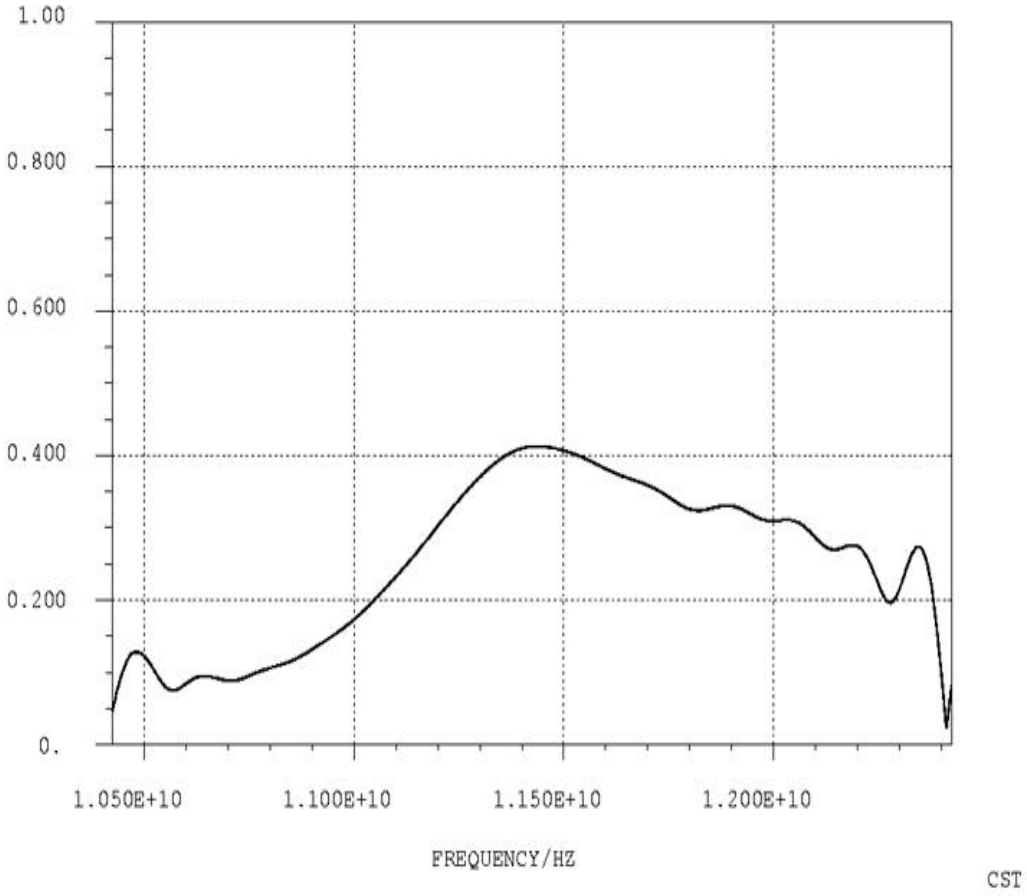

Figure 4.4 The Transmission Coefficient from the TE_{10} Mode to the HEM_{11} Mode

One can notice that the accuracy of the results of MAFIA simulation is not satisfactory. After intense calculations using MAFIA, there was little improvement resulted. There are several factors contributing to the problem.

First, the media in the calculated structure is not uniform. Large calculation errors may be induced at the interface of materials with differing material parameter. In the core FDTD algorithm of MAFIA, the continuous derivatives in both space and time are approximated by centered two-point finite differences, which result in second-order accuracy [74]. The higher order methods [76] have not been used in MAFIA, perhaps due to computational and programming complexity. In our case, the permittivity of the media is suddenly changed by a factor of 20 at the interface of dielectric and vacuum, the premise of using two-point finite differences may no longer hold. Therefore, suitable supporting algorithms for such dielectric-vacuum boundary conditions should be applied. As a commercial FDTD solver, MAFIA lacks provision for this class of special boundary conditions.

The second cause of the inaccuracy in this MAFIA simulation is how the boundary of the tapered dielectric section is represented in the mesh cells. One major limitation of the FDTD method is the use of the uniform orthogonal mesh. This restriction forces curved and diagonal boundaries to be represented by stair-cased approximations. Such approximations could be found in the generated mesh of our simulated waveguide junction. It is very demanding to accurately reproduce the curved boundary in the waveguide junction as shown in Figure 2.22, because the radius of the curvature is very small. Very-fine grids are expected to apply in this case. Because the tapered dielectric section has a

diagonal boundary, very fine grids should also be employed to represent such geometry in the thin dielectric layer. The total number of mesh cells needed is expected to be large, and the limited computation resources make very-fine mesh everywhere unpractical. Modified methods have been developed to allow greater geometric flexibility, but they also incur a higher computational cost [77-83]. However, the improvement can be achieved in a specially designed solver for the waveguide junction used in our dielectric loaded accelerator.

As described in the previous paragraph, the geometry of the waveguide junction imposes the challenges on the mesh generation for an accurate simulation. MAFIA allows employing grids of different sizes to represent the geometry. It is understandable that the mesh density in dielectric region should be very high, because the grid size needs to be very small. However, the large dimensional difference between the rectangular waveguide and the dielectric lined circular waveguide made it difficult to reach the optimal mesh generation. The input and output waveguide ports should be defined at the reference planes remote enough from the transit section, the coupling section, to obtain the stable solution that eliminates the effect from evanescent modes. Thus the actual coupling section only occupied a very small proportion of the whole calculated geometry. Another constraint on MAFIA's mesh generation is that the spatial ratio of the maximum grid to the minimum grid cannot exceed 10 for accurate computation [41, 74]. In the calculated structure, the thickness of dielectric region is equivalent to about 10 percent of the diameter of the circular waveguide, and 5 percent of the width of rectangular waveguide. To satisfy both requirements, it would still result in too many mesh cells to be handled in the available

memory space. Therefore, the calculations were carried out using the compromised mesh. Moreover, the time step would be relatively too small with respect to the large grids in the case of using different size grids in mesh generation. This could result in the increase of the numerical dispersion errors [75].

The sources of calculation inaccuracy of the MAFIA simulation for the coupling scheme have been discussed. MAFIA has been successfully applied to solve a large number of electromagnetic problems. Modified techniques for the FDTD methods are available to overcome such limitations of MAFIA in this simulation, which was designed to be applicable to most electromagnetic problems. Such improvement can be realized in a FDTD solving code written to target the coupling configuration with the tapered dielectric sections.

4.2 Experimental Evidence Of Mode Excitation In The Coupling Structure

The AWA step-up transformer experiment is introduced in this section, because it is not only a milestone in the development of dielectric based accelerating structures, but also it is an example of application for the efficient coupling scheme using a side-coupling iris and a tapered dielectric section. In addition, the experimental results can indirectly show the mode excitation problem of the coupling scheme. The waveguide modes excited in the dielectric-lined circular waveguide through the given coupling scheme can theoretically be identified using the bead-pull measurements. However, such measurements for X-band structures require special instrumentation.

As mentioned in Chapter 1, the AWA dielectric wakefield step-up transformer acceleration was proposed to overcome the constraint of collinear dielectric wakefield acceleration schemes in the transformer ratio [23]. The schematic drawing of the dielectric step-up transformer was given in Figure 1.3, consisting of a dielectric structure based two-beam acceleration scheme.

The experiment conducted on the AWA dielectric wakefield step-up transformer was to demonstrate two-beam acceleration and that the transformer ratio can be larger than 2. The implemented AWA step-up transformer extracts RF power from a relatively large diameter dielectric-lined waveguide (stage I) in which high intensity drive beams pass through and give out energy by Cerenkov radiation. The RF power is then fed into a small diameter dielectric-lined waveguide (stage II) where less-intensity witness beams can be accelerated by the greatly enhanced axial electric field. Field enhancement results both from a lower group velocity in stage II than in stage II (longitudinal compression), and from geometrical effects made possible by the use of the dielectric-lined waveguide (transverse compression).

The efficient wave coupling was also a major engineering challenge in implementing such step-up transformer, especially the coupling section of stage II waveguide that uses high-dielectric-constant ceramic to achieve a smaller group velocity. After the efficient wave coupling technique was demonstrated in the externally powered traveling-wave dielectric loaded accelerating structure discussed in Chapter 2 and 3, the prototype AWA step-up transformer that adopted the same coupling technique was constructed in March 2000. The actual two-beam experiment was conducted in May 2000 [36]. The actual

dielectric wakefield step-up transformer is shown in Figure 4.5. A directional coupler was mounted on the rectangular waveguide connecting two stages to monitor the forwarding (from stage I) and reflected (from stage II) RF power. The geometric parameters of stage I and stage II were chosen to satisfy that the phase velocity of TM_{01} mode is equal to the speed of light at 7.8 GHz. This scheme utilizes the superposition of wakefields of multiple drive beam bunches. Because the drive beam LINAC of the AWA test facility operates at 1.3GHz, the operating frequency of the step-up transformer should be a harmonic of 1.3GHz to achieve the correct superposition of wakefields whose phases are determined by the timing of the drive beam bunches. When drive electron beams pass through the stage I, the TM_{01} wave caused by Cerenkov radiation propagates at the speed of light, and thus has the center frequency at 7.8 GHz. If drive beams travel along the axis, the dominant wakefield mode is TM_{01} mode. Figure 4.6 shows the schematic drawing of the setup of the two-beam experiment. Figure 4.7 and 4.8 show the experimental installation of the step-up transformer in the beam line. The layout of two beam lines of the AWA test facility is given in Figure 4.9. The dielectric step-up transformer and energy spectrometer are mounted at the ends of the beam lines.

The spectrum measurement of the forward RF wave is given in Figure 4.10. The center frequency is at 7.8 GHz. The spectrum of the reverse RF wave is shown in Figure 4.11. The center frequency of the dominant mode is still at 7.8 GHz. From such two figures, we can see the dominant mode in both stage I and stage II waveguide is TM_{01} mode.

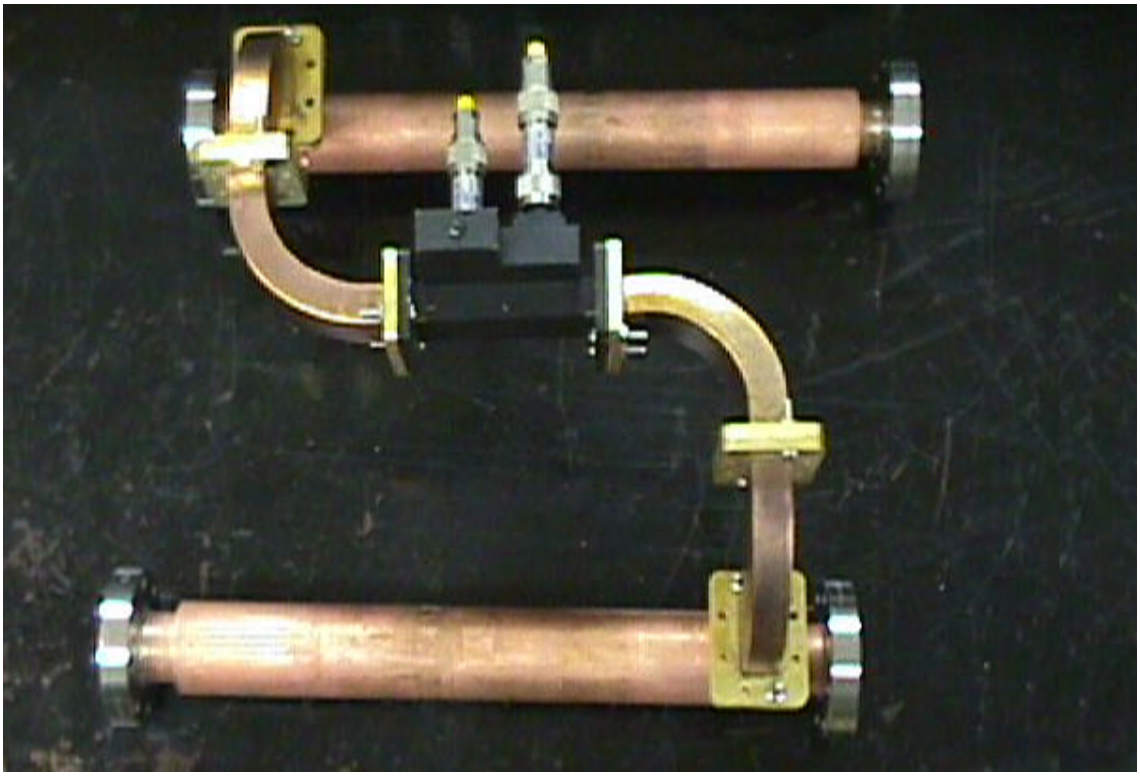

Figure 4.5 The AWA Dielectric Wakefield Step-up Transformer Accelerator

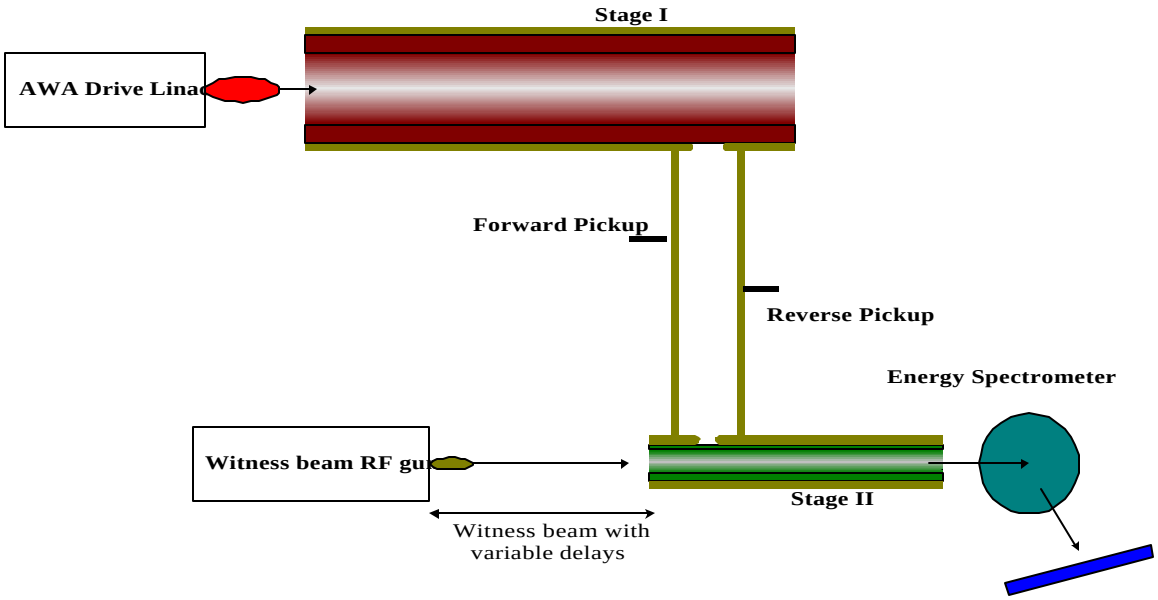

Figure 4.6 Two Beam Acceleration Experiment Setup of the AWA Dielectric Step-up Transformer

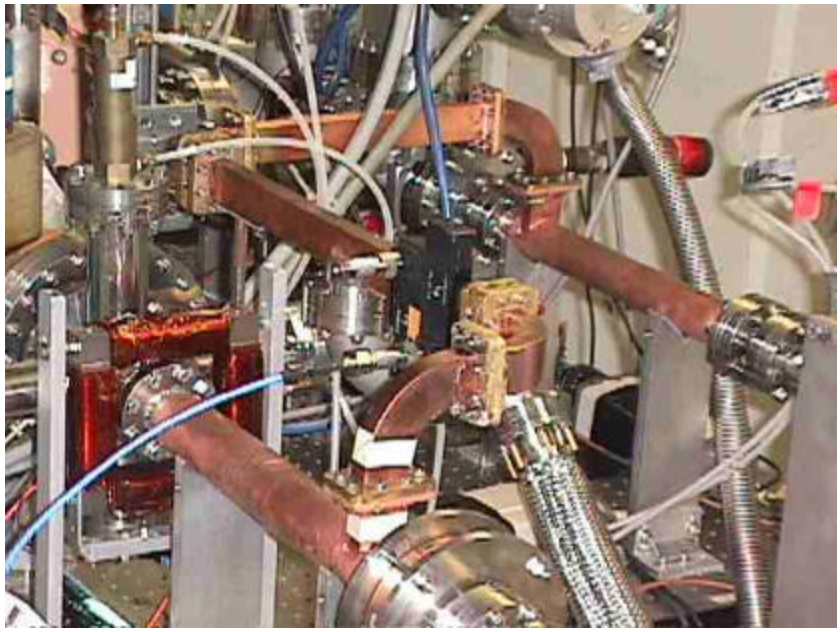

Figure 4.7 The Installation of The AWA Dielectric Wakefield Step-up Transformer Accelerator (I)

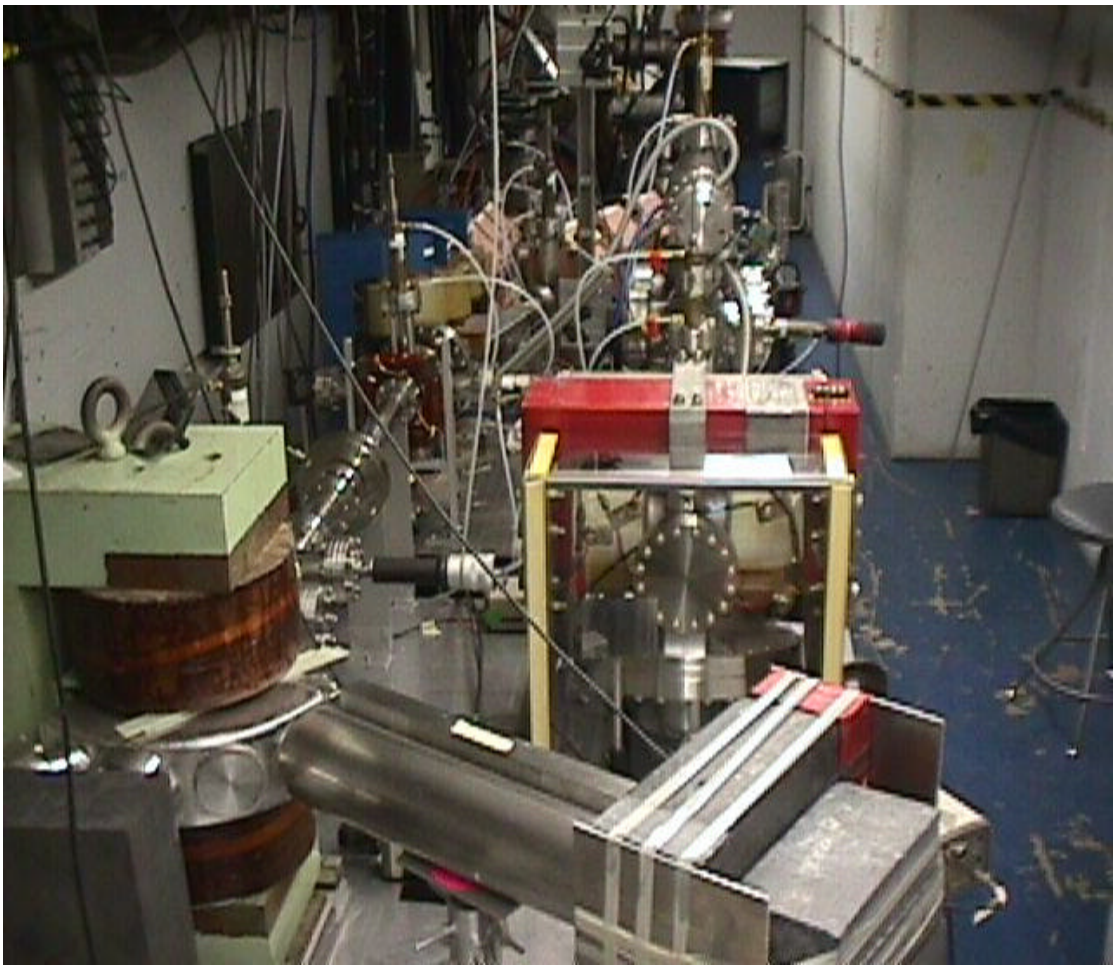

Figure 4.8 The Installation of The AWA Dielectric Wakefield Step-up Transformer Accelerator (II)

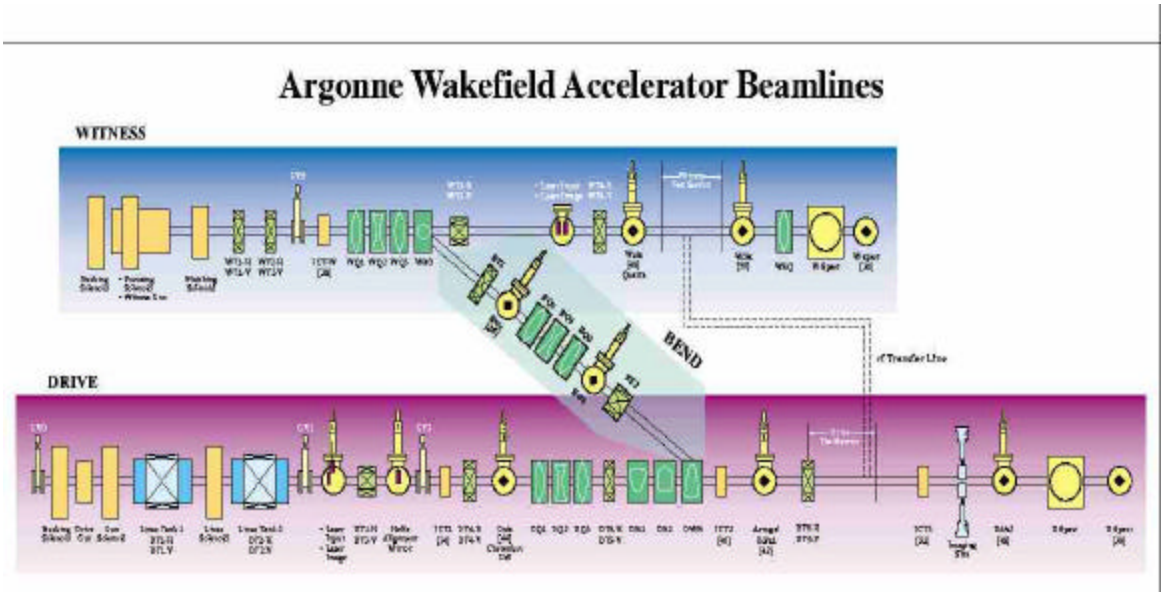

Figure 4.9 The Layout of The Beam Lines of the AWA Test Facility

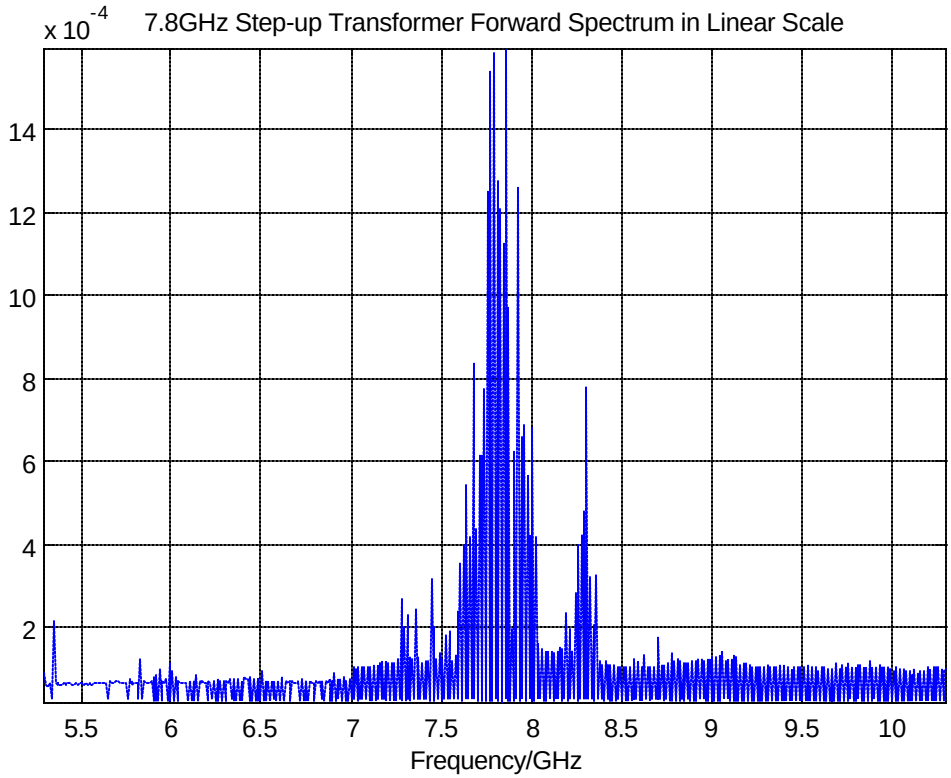

Figure 4.10 The Spectrum of the Forward RF Wave in Step-up Transformer

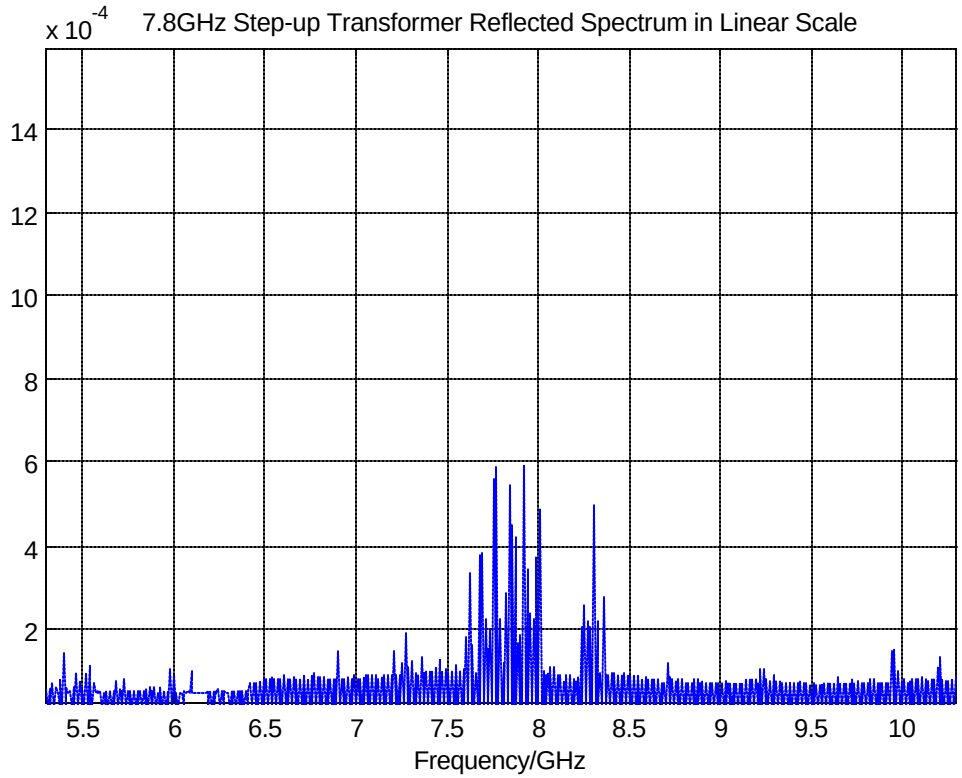

Figure 4.11 The Spectrum of the Reverse RF Wave in Dielectric Step-up Transformer

The energy spectrum of the witness beam is given in Figure 4.12. With adjusting the synchronization phase, the witness beam can be accelerated, or decelerated. The time difference between acceleration and deceleration is about a half cycle of 7.8 GHz TM_{01} wave. The important parameters of the step-up transformer are given in Table 4.1. The maximum energy gain of the witness beam is over 7.5 MeV. Considering the coupling coefficients of two stages and the RF power, in stage I, produced by the drive beams, the transformer ratio was proven greater than 2, and the experimental results perfectly agreed with the calculations.

The efficiency of the coupling technique was also demonstrated in this experiment, and the acceleration of the witness beam in stage II showed that such coupling configuration couples major portion of RF power into the TM_{01} mode.

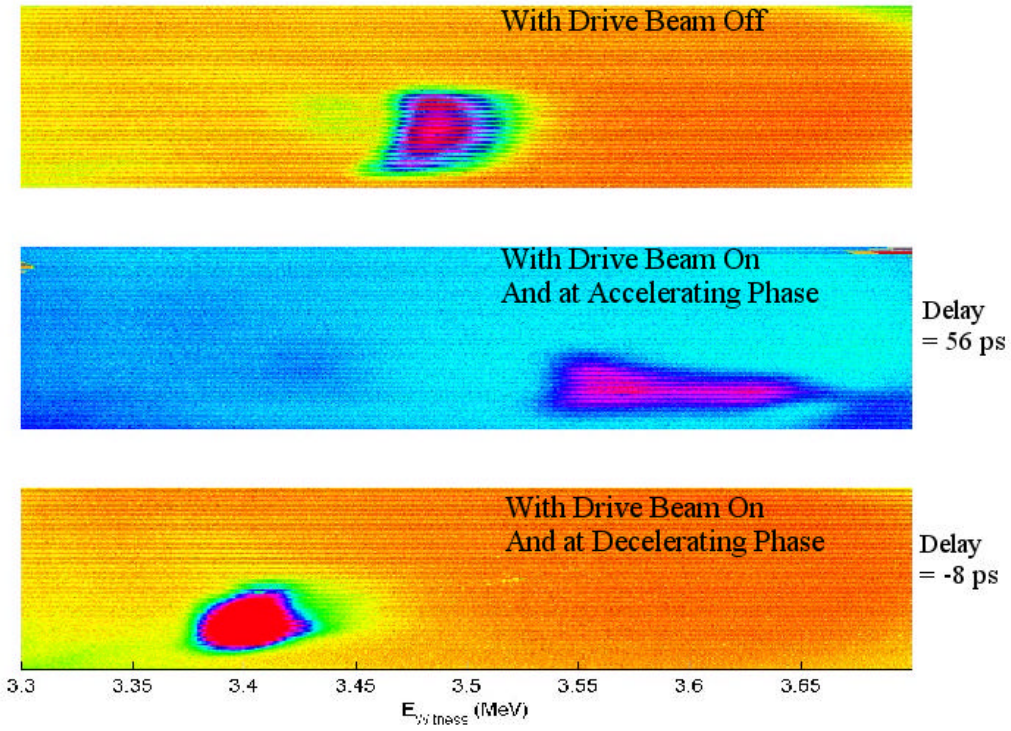

Figure 4.12 The Energy Spectrum Measurement of the Two-beam Acceleration

Table 4.1 Important Parameters Of The Dielectric Wakefield Step-up Transformer Acceleration Experiment

Coefficient	Value
Goal	To demonstrate the principle of the dielectric based two-beam acceleration. And to demonstrate the electric field step-up in stage II.
Drive Beam	20 – 25 nC, 1 pulse, 15 MeV
Stage I (driving stage)	Material: Corderite Inner radius = 6.00 mm Outer radius = 11.15 mm Dielectric constant $\varepsilon = 4.6$ Wakefield E_z = 3 – 3.5 MV/m Length = 30.0 cm RF pulse length ~ 3 ns RF peak power = 4 MW
Stage II (accelerating stage)	Material: E20 Inner radius = 3.00 mm Outer radius = 5.41 mm Dielectric constant $\varepsilon = 20$ Wakefield E_z = 8 MV/m Length = 30.0 cm Acceleration distance = 3 cm
Measured Gradient (in stage II)	7.5 MV/m
Measured Transformer Ratio	>2
Frequency of the TM_{01} Mode	7.8 GHz

CHAPTER V

A HYBRID DIELECTRIC-IRIS-LOADED PERIODIC ACCELERATION STRUCTURE

5.1 Introduction

One of the major challenges confronting future high energy linear accelerators is the development of high gradient accelerating structures. The most commonly studied structure is a conventional iris-loaded copper structure representing an evolution from those used at Stanford Linear Collider (SLC) to the proposed Next Linear Collider (NLC) and possibly CERN Linear Collider (CLIC) [38-40]. However, in all the iris-loaded structures, the peak surface electric field E_s can be an important constraint because it is in general found to be at least a factor of 2 larger than the axial acceleration field E_a [38-40]. Because the peak surface electric field causes electric breakdown of the structure, it represents a direct limitation on the maximum acceleration gradient that can be obtained. If the peak surface electric field exceeds the breakdown limit at the operating frequency, it can cause damage to the irises through arcing and detune the structure. Such phenomena were observed in the high acceleration gradient testing of NLC-type structures, with the axial acceleration gradient up to 50 MV/m [11, 84]. Permanent damage of copper surface resulted from the breakdown was identified. Thus the high ratio of E_s to E_a limits the achievable accelerating gradient, assuming the availability of high power RF sources is not a constraint. This case by far is true for the development of NLC structures. In this chapter, we propose a hybrid dielectric and iris loaded acceleration structure that has a lower ratio of E_s to E_a, and comparable shunt impedance per unit length r, and r/Q, to a conventional iris-loaded accelerating structure. Using this device, E_s/E_a can be reduced to

about 1, while maintaining reasonably good acceleration efficiency as measured by r and r/Q. The upper limit of the accelerating gradient can be increased, depending on the dielectric breakdown properties at high fields, which can be revealed through the high power experiment proposed in Chapter 3.

The use of uniform dielectric-lined circular waveguides as accelerating structures has been discussed in many previous studies [25, 27-29] and in Chapter 2. One distinct advantage is that the axial accelerating electric field is the maximum field in this class of structures. The acceleration mode used here is the TM_{01}. The group velocity is typically less than 10 percent of the speed of light. Such small group velocities can be obtained by the use of high dielectric constant ceramics, which however have the drawback of an enhanced surface magnetic field, which results in more power dissipation on the wall. The result is that the quality factor Q of a dielectric-lined waveguides is degraded compared to an iris-loaded structure with the same group velocity. Another disadvantage of accelerating structures based on uniform dielectric-lined circular waveguides is that this class of structure can support multiple propagating waveguide modes when they are operated in the TM_{01} mode. The results given in Chapter 2 and 4 show such property of uniform dielectric-lined circular waveguides. Even though this characteristic can reduce the single beam instability, it can also result in energy losses from mode conversion, and increase the difficulty to excite the correct waveguide mode at the side-coupling irises.

On the contrary, conventional iris-loaded accelerating structures have high quality factor that are almost constant with respect to different group velocities of the TM_{01} mode. At the same time, the TM_{01} mode is the lowest propagating mode in the iris-loaded

accelerating structure. However, its high peak surface electric field becomes the constraint of the achievable accelerating gradient.

Based on these observations we might consider a hybrid dielectric and iris loaded structure in order to produce a device which balances between high Q and reduced surface fields. This device is shown in Figure 5.1. Calculations of the properties of a hybrid traveling-wave acceleration structure at 11.4 GHz as a function of iris size and permittivity of the loading dielectric are performed. The results show that it is indeed possible to significantly reduce the ratio of the peak surface electric field to the accelerating field gradient without substantially diminishing the shunt impedance per unit length r and the ratio r/Q.

5.2 Numerical Method

Our calculations were limited to traveling-wave accelerating structures. The reasons why traveling-wave accelerating structures are preferred were discussed in the previous chapters. An iris-loaded periodic structure may be viewed as an array of pillbox cavities that are coupled through the irises. Therefore, one way to study a traveling-wave periodic structure is to use a numerical code such as SUPERFISH [85] or MAFIA [41], which provide accurate fields and other electromagnetic properties of a standing wave structure. Loew et al. [86] showed that by using RF properties of standing-wave structures, one could obtain RF properties of the corresponding traveling-wave structures. This conversion will be briefly outlined in the following.

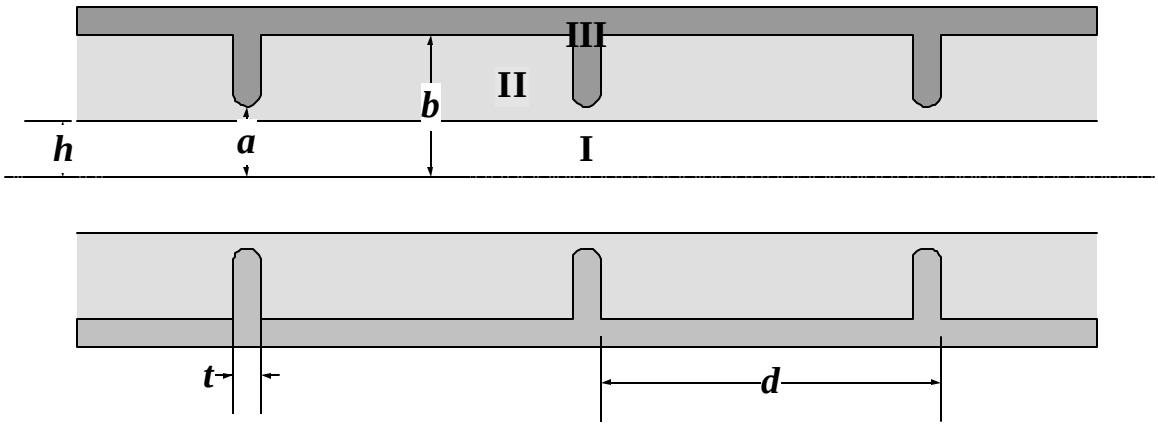

Figure 5.1 Schematic Drawing of a Hybrid Dielectric-iris-loaded Periodic Acceleration Structure. The function of the dielectric is to reduce the surface electric field at the iris relative to the axial, accelerating field. In the figure, region I is vacuum; region II is ceramic with dielectric constant ε; region III is copper. *a* is the iris radius, *b* is the outer radius, and *h* is the beam hole radius. *t* is the thickness of the iris and *d* is the length of one cell. In this paper, we use *a* to denote the iris radius for both hybrid dielectric-iris-loaded structures and pure iris-loaded structures.

Consider a periodic structure as shown in Figure 5.1. It is well known that the axial electric field E_z of the TM_{01} mode in the traveling-wave periodic structures can be expressed as

$$E_{z,TW} = \sum_{n=-\infty}^{n=+\infty} a_n(r) e^{j(wt - b_n z)} \tag{5.1}$$

where a_n is the amplitude of the space harmonic of index n,

$$b_n z = b_o z + \frac{2pnz}{d} \tag{5.2}$$

b_n is the propagation constant of the space harmonic of index n, and d is the spatial period (the length of one cell). The propagation constant of such a TM_{01} wave is the same as b_0.

With electric boundary conditions (E_t=0) applied at z=0 and z=λ (where $l = 2p / b_0$), the axial electric fields of the standing waves can be expressed as

$$E_{z,SW} = e^{jwt} \sum_{n=-\infty}^{n=+\infty} 2a_n \cos b_n z \tag{5.3}$$

The factor of 2 comes from the summation of two traveling waves of amplitude a_n. This equation takes the same form for the other field components.

Using MAFIA, one can calculate resonant frequencies, stored energies and power dissipation of resonant modes in an array of cavities. The standing wave field components output by the code can be analyzed as follows to obtain the traveling wave components.

If two traveling waves of the proper phase can add up to a standing wave (Equation 5.3), there must conversely be two appropriately phased standing waves that add up to a traveling wave. Assuming the first standing wave is $\vec{A}$, and the second standing wave $\vec{B}$ is obtained by shifting $\vec{A}$ to the left by d, then

$$\vec{B} = e^{jwt}\sum_{-\infty}^{+\infty} 2a_n \cos b_n(z+d)$$
$$\vec{A} = e^{jwt}\sum_{-\infty}^{+\infty} 2a_n \cos b_n z \tag{5.4}$$

Both of these standing waves are made up of one traveling wave going left and one going right. It is possible to add them with the proper phases to have the traveling waves going left canceled and those going right added. Thus, we can obtain the traveling wave field component in such structure. This can be achieved by multiplying $\vec{A}$ by $e^{j(b_0 d - p/2)}$ and $\vec{B}$ by $e^{jp/2}$

$$\vec{B} = e^{jwt}\sum_{-\infty}^{+\infty} 2a_n \cos b_n(z+d) = e^{jwt}\sum_{-\infty}^{+\infty} a_n(e^{-jb_n(z+d)} + e^{jb_n(z+d)})$$
$$\vec{A} = e^{jwt}\sum_{-\infty}^{+\infty} 2a_n \cos b_n z = e^{jwt}\sum_{-\infty}^{+\infty} a_n(e^{-jb_n z} + e^{jb_n z}) \tag{5.5}$$

$$\vec{B}e^{jp/2} = e^{jwt}e^{jp/2}\sum_{-\infty}^{+\infty} a_n(e^{-jb_n(z+d)} + e^{jb_n(z+d)})$$
$$\vec{A}e^{j(b_0 d - p/2)} = e^{jwt}e^{j(b_0 d - p/2)}\sum_{-\infty}^{+\infty} a_n(e^{-jb_n z} + e^{jb_n z}) \tag{5.6}$$

$$b_n z = b_0 z + 2pnz/d$$
$$b_n d = b_0 d + 2pn \tag{5.7}$$

Substituting Equation 5.7 into Equation 5.6, we have

$$\vec{B}e^{jp/2} = e^{jwt}\sum_{-\infty}^{+\infty} a_n(je^{jb_n z}e^{jb_0 d} + je^{-jb_n z}e^{-jb_0 d})$$
$$\vec{A}e^{j(b_0 d - p/2)} = e^{jwt}\sum_{-\infty}^{+\infty} a_n(-je^{jb_n z}e^{jb_0 d} - je^{-jb_n z}e^{jb_0 d}) \tag{5.8}$$

Adding up the two equations in (5.8), we have

$$\vec{B}e^{jp/2} + \vec{A}e^{j(b_0 d - p/2)} = 2\sin b_0 d\sum_{-\infty}^{+\infty} a_n e^{j(wt - b_n z)} \tag{5.9}$$

The amplitude and phase of the field components of traveling waves can be obtained by the following equations

$$|TW|^2 = \frac{A^2 + B^2 - 2AB\cos b_0 d}{4\sin^2 b_0 d}$$
$$\tan q(z) = \frac{B - A\cos b_0 d}{A\sin b_0 d} \tag{5.10}$$

where A and B are functions of z.

Thus the field solutions of a traveling-wave periodic accelerating structure can be obtained using the conversion given in Equation 5.10. Such conversion is applicable to all field components if the corresponding standing-wave structure has electric boundary conditions (E_t=0) applied at z=0 and z=λ (where $l = 2p / b_0$). The RF properties of the traveling-wave periodic accelerator, such as group velocity and shunt impedance, can subsequently be calculated.

The method to compute the RF properties of traveling-wave accelerating structures has been visited in Chapter 2. Here a different method will be used to calculate the shunt impedance of such structure. Because the field solutions of the standing-wave structure are already known, it will be easier to compute the shunt impedance of the standing-wave structure, and then derive that of the traveling-wave structure. The concept of such computation will be visited in the following.

As described earlier, the shunt impedance, a figure of merit that is independent of the excitation level of the cavity and measures the effectiveness of producing an axial voltage V_0 for a given power dissipated, is defined by [87]

$$r_s = \frac{V_0^{\,2}}{P_{diss}} \tag{5.11}$$

where P_{diss} is the power dissipated in the wall.

In an accelerating structure we are really more interested in maximizing the particle energy gain per unit power dissipation. The energy gain of an arbitrary particle with charge q traveling through the gap on axis of a standing-wave cavity is

$$\Delta W = q\int_{-L/2}^{L/2} E(0,z)\cos[wt(z)+f]dz \tag{5.12}$$

For the given accelerating gap with a length of L, and the electric field on the axis experienced by this particle with velocity v is

$$E_z(r=0,z,t) = E(0,z)\cos[wt(z)+f] \tag{5.13}$$

where $t(z) = \int_0^z dz/v(z)$ is the time when the particle is at position z. At t=0, the phase of the field relative to the crest is f.

The use of a common trigonometric identity allows us to write the energy gain as

$$\begin{aligned} \Delta W &= q\int_{-L/2}^{L/2} E(0,z)[\cos wt\cos f - \sin wt\sin f]dz \\ \Delta W &= qV_0T\cos f \end{aligned} \tag{5.14}$$

where V_0 is an axial RF voltage, defined by

$$V_0 \equiv \int_{-L/2}^{L/2} E(0,z)dz \tag{5.15}$$

The transit-time factor T is defined by

$$T \equiv \frac{\int_{-L/2}^{L/2} E(0,z)\cos wt(z)dz}{\int_{-L/2}^{L/2} E(0,z)dz} - \tan f\,\frac{\int_{-L/2}^{L/2} E(0,z)\sin wt(z)dz}{\int_{-L/2}^{L/2} E(0,z)dz} \tag{5.16}$$

The phase f=0 if the particle arrives at the origin when the field is at a crest. It is negative if the particle arrives at the origin earlier than the crest, and positive if it arrives later. Maximum energy gain occurs when f=0, which is often the choice for relativistic electrons. The phase and the transit-time factor depend on the choice of the origin. It is convenient to

simplify the transit-time factor, and remove its dependence on the phase, by choosing the origin at the electrical center. E(z) is usually approximately an even function about a geometric center of the gap. We will choose the origin at the electrical center of the gap, then

$$0 = \int_{-L/2}^{L/2} E(0,z)\sin wt(z)dz \tag{5.17}$$

When E(z) is an even function about the geometric center of the gap, the electrical center and the geometric center coincide. The transit-time factor simplifies to

$$T \equiv \frac{\int_{-L/2}^{L/2} E(0,z)\cos wt(z)dz}{\int_{-L/2}^{L/2} E(0,z)dz} \tag{5.18}$$

The transit-time factor expression in this equation is the average of the cosine factor weighted by the field. The transit-time factor increases when the field is more concentrated longitudinally near the origin, where the cosine factor is largest. In most practical cases the change of particle velocity in the gap is small compared to the initial velocity. If we ignore the velocity change, we have

$$wt \approx \frac{wz}{v} = \frac{2pz}{b\,l} \tag{5.19}$$

where $b=v/c$ and $b\,l$ is the distance the particle travels in an RF period. Then, the simplified form of the transit-time factor most often used is defined by

$$T \equiv \frac{\int_{-L/2}^{L/2} E(0,z)\cos(2pz/b\,l)dz}{\int_{-L/2}^{L/2} E(0,z)dz} \tag{5.20}$$

The average axial electric-field amplitude is defined by $E_0=V_0/L$, where V_0 is the voltage gain that would be experienced by a particle passing a constant dc field equal to the field in

the gap at time t=0. The effective acceleration gradient is the quantity E_0T. In terms of E_0, the energy gain can be expressed by the Panofsky equation [88] as

$$\Delta W = qE_0T\cos\phi L \tag{5.21}$$

The physics contained within the transit-time factor is that the energy gain of a particle in a harmonically time-varying field is always less than the energy gain in a constant dc field equal to that seen by the particle at the center of the gap. The transit-time factor T is the ratio of the energy gained in the time-varying RF field to that in a dc field of voltage $V_0\cos\phi$.

From the above, it is clear that the peak energy gain of a particle occurs when ϕ=0 and is $\Delta W_{\phi=0}=qV_0T$. The effective shunt impedance of a cavity is defined by

$$r' = \left(\frac{\Delta W_{\phi=0}}{q}\right)^2 \frac{1}{P_{diss}} = \frac{(V_0T)^2}{P_{diss}} = r_sT^2 \tag{5.22}$$

This parameter measures the effectiveness per unit power loss for delivering energy to a particle. For a given field, both $V_0=E_0L$ and P increase linearly with cavity length, as do both r' and r_s. For long cavities we often use a figure of merit that is independent of both the field magnitude and the cavity length. Thus the shunt impedance per unit length Z is expressed as

$$Z \equiv \frac{r_s}{L} = \frac{E_0^{\,2}}{P_{diss}/L} \tag{5.23}$$

Similarly, the effective shunt impedance per unit length ZT^2 is

$$ZT^2 \equiv \frac{r}{L} = \frac{(E_0T)^2}{P_{diss}/L} \tag{5.24}$$

Z and ZT^2 are usually tens of megohms per meter. One of the main objectives in accelerating cavity design is to choose the geometry to maximize effective shunt

impedance per unit length. This is equivalent to maximizing the energy gain in a given length for a given power loss.

The shunt impedance per unit length r of the traveling-wave accelerating structure can obtained from the effective shunt impedance per unit length of the corresponding standing-wave structure by the following equation [89]

$$r = 2ZT^2 \equiv \frac{2(E_0 T)^2}{P_{diss} / L} \tag{5.25}$$

Using the method described in this section, one can obtain the field solutions and the accelerator properties of a traveling-wave hybrid dielectric-iris-loaded periodic acceleration structure.

5.3 Numerical Results and Analysis

In this chapter, we specialize our investigation to consider only the $2\pi/3$ mode of the propagated wave, whose wavelength l is equal to the total length of 3 cells when the phase velocity is the speed of light as required for the acceleration of ultra-relativistic particles. The reason of choosing $2\pi/3$ mode for traveling-wave accelerating structures is that it has the maximum shunt impedance per unit length. First, we calculated a resonator with 3 cells (with electric boundaries E_t=0 at z=0 and z=l) using MAFIA. The field solutions and mesh coordinates were output to ASCII data files. A post-processing program was written to extract the field solutions and mesh information of the standing wave solution, and then carry out the conversion from standing-wave solutions to traveling-wave solutions using the method outlined in previous section.

Figures 5.2 and 5.3 show the MAFIA simulation results for the electric field pattern of the $2\pi/3$ mode in an iris-loaded structure and a hybrid dielectric-iris-loaded structure, respectively. Because of the axial symmetry, only the upper half part of the longitudinal cross-section is plotted.

The conversion of standing waves to traveling waves according to Equation 5.10 was carried out. Figure 5.4 shows the amplitude and phase of the axial electric field of the resulting traveling wave in a hybrid dielectric-iris-loaded structure (with a=5.5 mm, b=6.923 mm, and h= 4 mm). Other field components can be obtained through a similar procedure. These results show the characteristics of the field components in the periodic accelerating structure.

5.3.1 Calculation of Pure Iris-loaded Traveling-wave Structures. The corresponding traveling wave parameters of Figure 5.2 structure were calculated and given below in Table 5.1. In a pure iris-loaded structure, the group velocity of the TM_{01} wave and shunt impedance per unit length are determined by the radius of the irises. At the same time, the outer radius of the cylinder has to be adjusted to maintain the phase velocity of the TM_{01} wave synchronized with the beam velocity c. Thus the iris radius is the governing geometric parameter for the RF properties of a pure iris-loaded accelerating structure. For the structure with iris radius a=5.6 mm, resulting in a group velocity of 0.088c. The shunt impedance per unit length r is 75 MΩ/m, and the quality factor Q is 7251. The RF properties of the calculated pure iris-loaded structure are similar to those of the typical NLC structures [39].

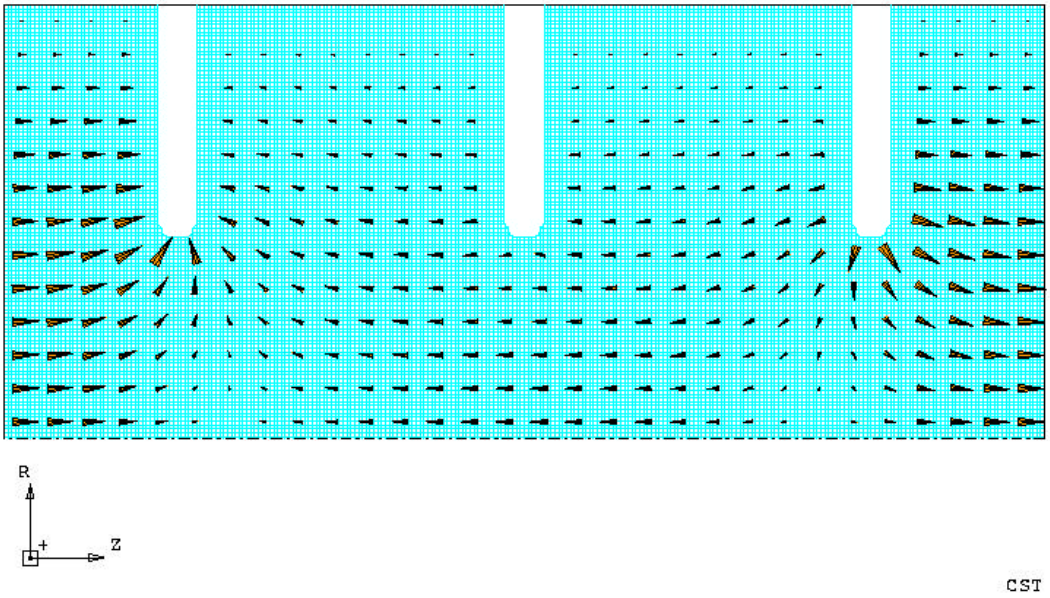

Figure 5.2 Electric Field Pattern of the $2\pi/3$ Mode in an Iris-loaded Acceleration Structure. The iris radius a=5.6 mm, the iris thickness t=1.0 mm, and outer radius b= 11.1254 mm. Here E_s/E_a=2.4.

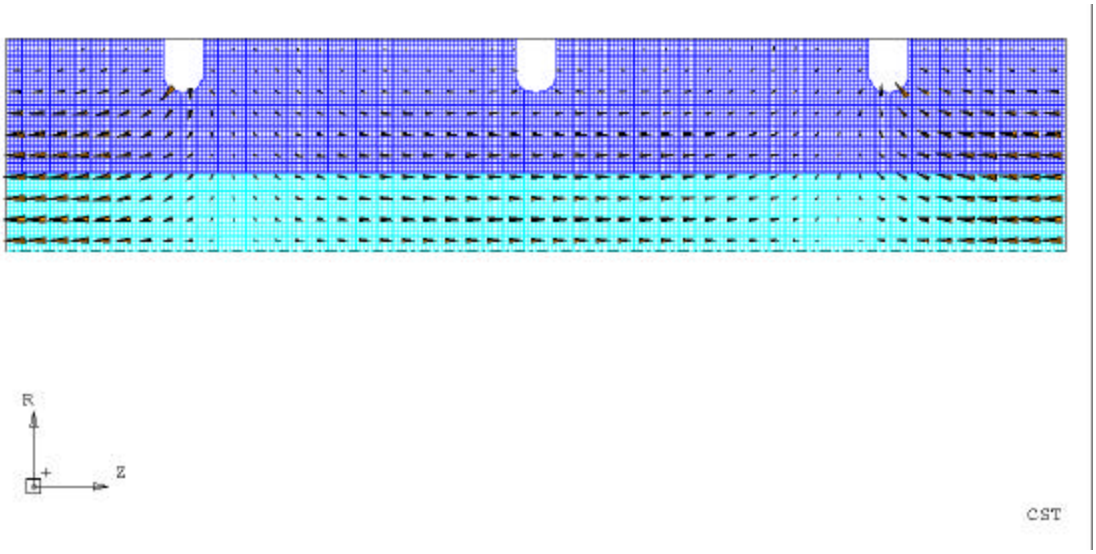

Figure 5.3 Electric Field Pattern of the $2\pi/3$ Mode in a Hybrid Dielectric-iris-loaded Acceleration Structure. The e=6, a= 4.0 mm, b= 5.361 mm, and the beam hole radius h= 2.0 mm. E_s/E_a=1.01.

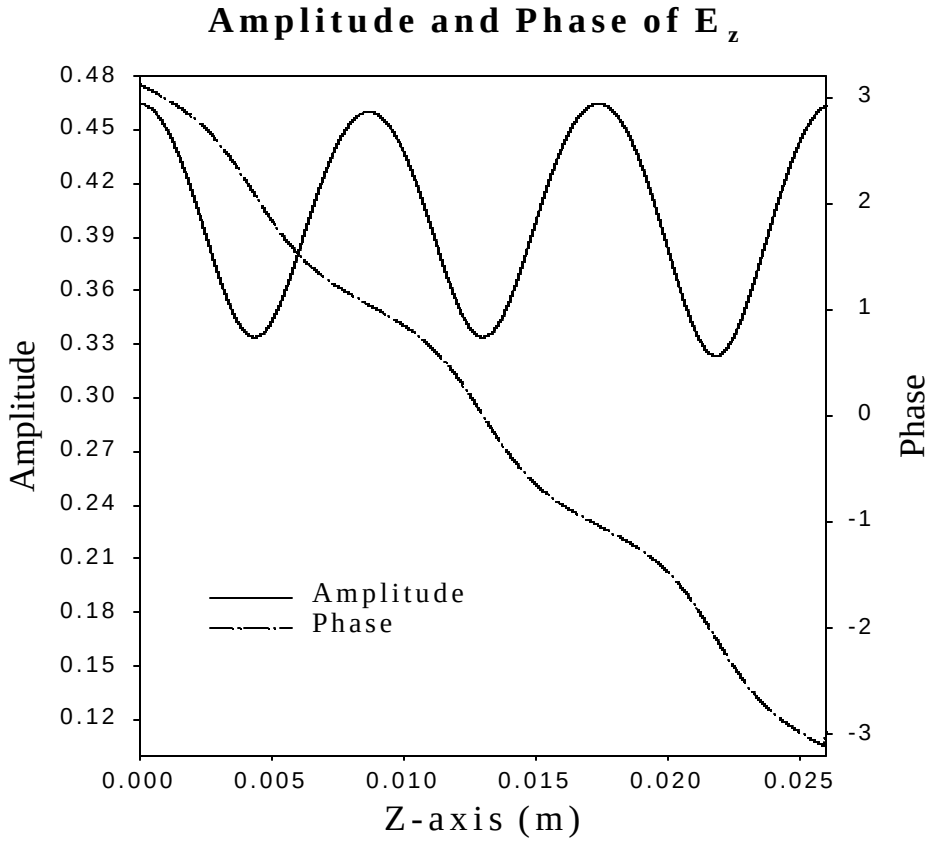

Figure 5.4 Amplitude and Phase Plots of E_z at r=0 in a Hybrid Dielectric-iris-loaded Traveling-wave Structure. The geometric parameters of this structure are given in Figure 5.3.

Table 5.1 11.424 GHz Iris-loaded Traveling-wave Structure

a (mm)	b (mm)	t (mm)	d (mm)	E_s/E_a	r (MW/m)	Q	r/Q (W/m)	v_g (c)
5.6021	11.1254	1.0	8.7535	2.4	75.6	7251	10343	0.088

The contour plot and surface plot of the distribution of electric field amplitude are shown in Figure 5.5. We can easily identify that the peak surface electric field occurs at the edge of the iris, and E_s/E_a is about 2.4.

5.3.2 Calculation on the Hybrid Dielectric-Iris-Loaded Traveling-wave Structures. Unlike the iris-loaded structure, the group velocity and shunt impedance per unit length r of acceleration TM_{01} mode in a hybrid dielectric-iris-loaded structure is not only the function of beam aperture radius, but also the iris radius and the dielectric constant. For a given group velocity, the outer radius of the cylinder b is determined to synchronize the phase velocity with the beam velocity. In this section, we describe a self-consistent calculation of hybrid structures with a fixed iris radius and a range of dielectric constant e, and also varying the beam hole radius.

To illustrate our point, we have chosen e=6 as our first example. Figure 5.6 shows the ratio E_s/E_a as the function of beam aperture radius. Its value ranges from 0.8 to 1.5, significantly lower than the iris-loaded structure case described in Figure 5.2. Figure 5.7 shows the effect of the beam hole radius on the group velocity of the TM_{01} mode for the same structure parameters. In order to have a fair comparison for all the parameters studied here, we have chosen the group velocity to be nearly the same as in the pure iris loaded case. Table 5.2 gives the geometric parameters and RF properties of a hybrid structures for two different beam aperture sizes. The first case, with beam aperture radius

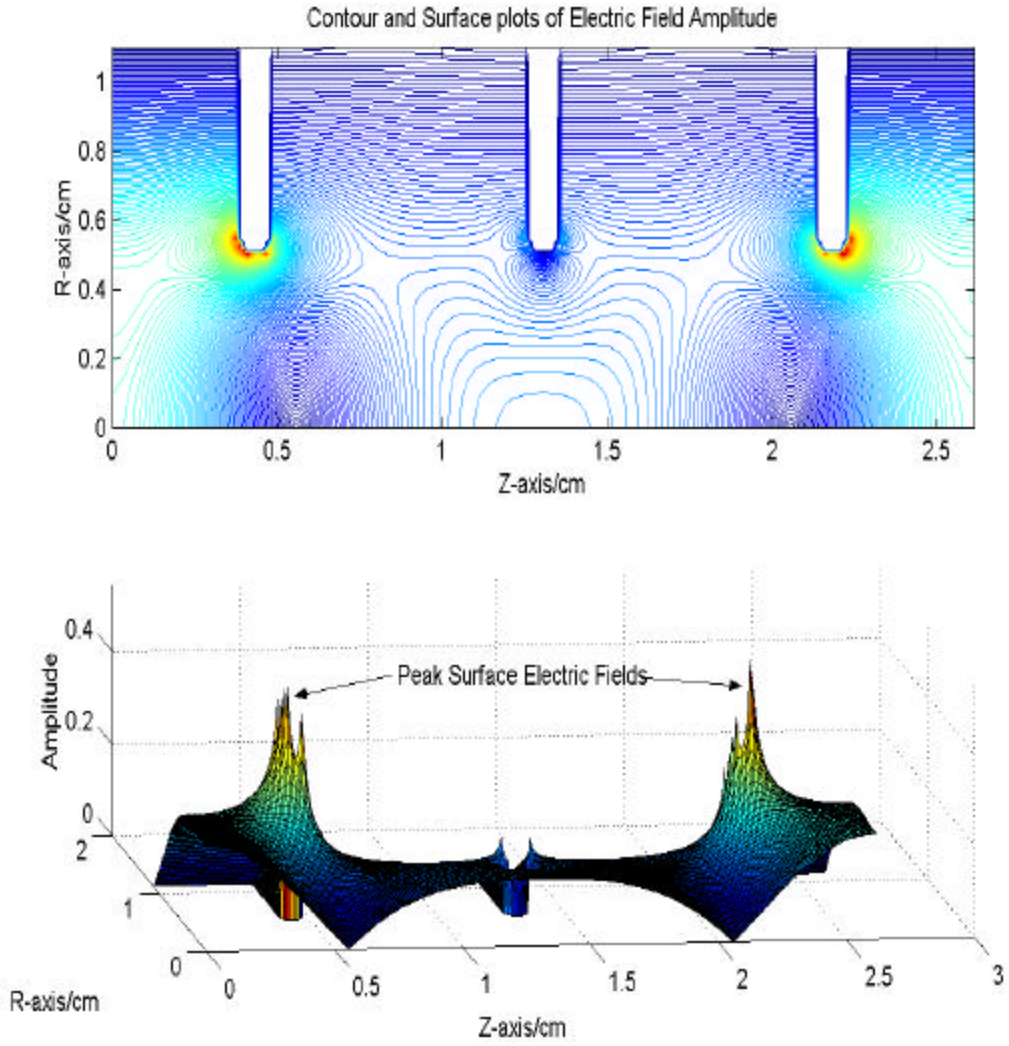

Figure 5.5 The Contour Plot and Corresponding Surface Plot Showing the Distribution of Electric Field Amplitudes in an Iris-loaded Traveling-wave Structure. The geometric parameters of this structure are given in Figure 5.2. In both contour plot and surface plot, the dark red indicates the strongest field amplitude. We observe that the strongest electric field occurs at the edge of the iris. In this case, E_s/E_a is about 2.4.

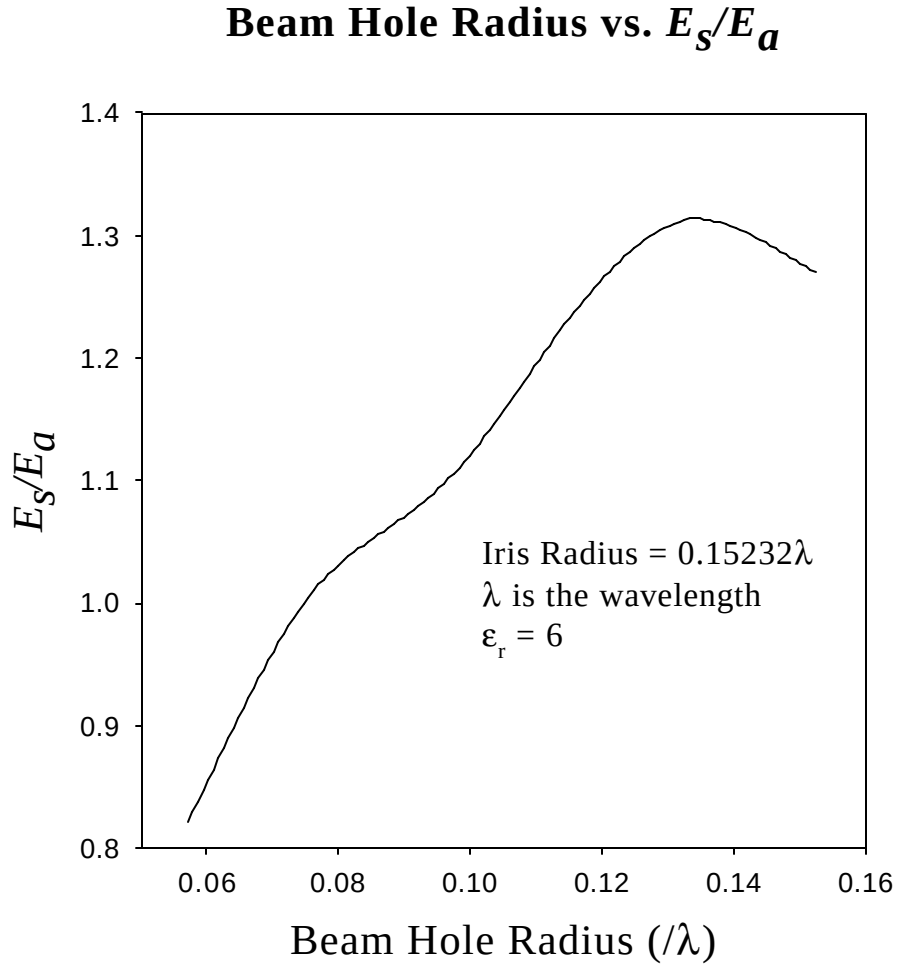

Figure 5.6 Beam Aperture Radius *h* vs. E_s/E_a in a Hybrid Dielectric-iris-loaded Structure. Here e=6, and the iris radius a is fixed as 4.0 mm. The wavelength λ is equal to the total length of 3 cells, and is 26.2605 mm. In all calculations, the iris thickness t is fixed as 1.0 mm. The outer radius b is adjusted accordingly to have the phase velocity of TM_{01} mode equal to c.

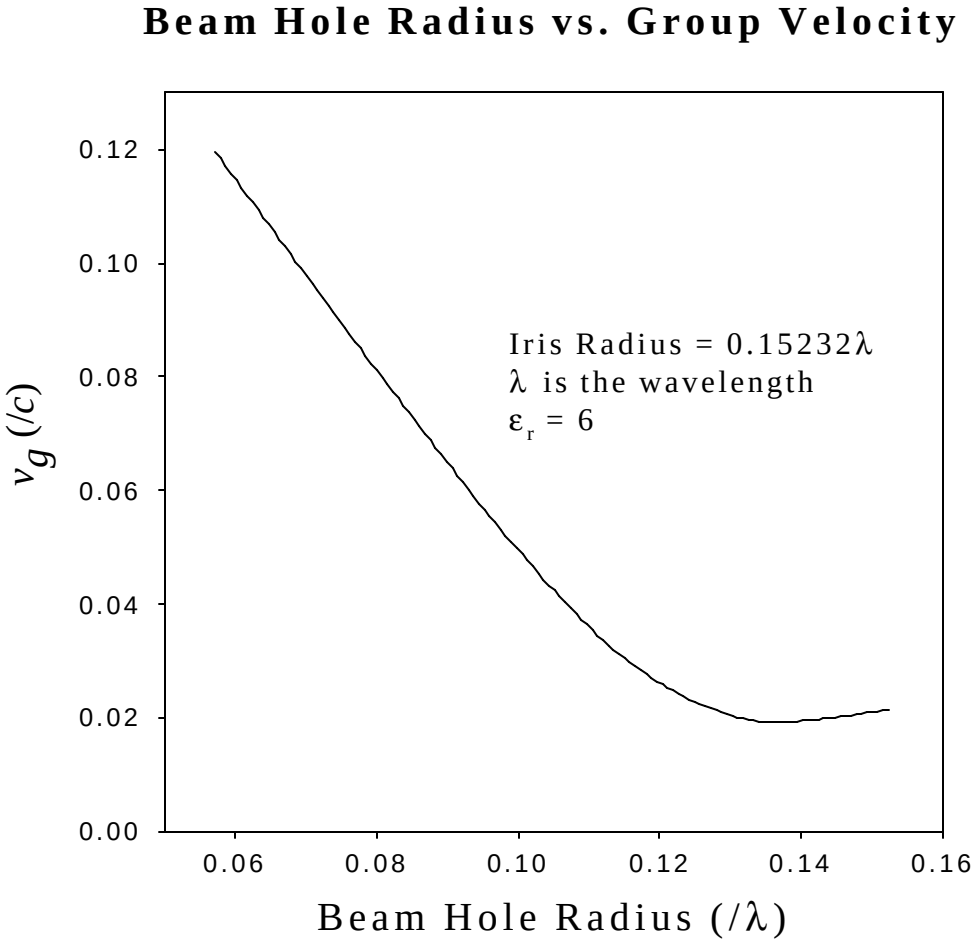

Figure 5.7 Beam Aperture Radius vs. Group Velocity of the TM_{01} mode in a Hybrid Dielectric-iris-loaded Structure with Geometry as in Figure 5.6

of 4 mm and iris radius of 5.5 mm, gives a shunt impedance of 38 MΩ/m with Q=4506. One could decrease the beam hole to increase the shunt impedance and Q as shown in the second case of Table 5.2. The ratio E_s/E_a=1.01 is obtained. For a beam aperture radius = 2 mm and adjusting the other parameters accordingly, we obtain r = 66MΩ/m, slightly lower than that of the iris-loaded structure listed in Table 5.1. At the same time, the quality factor Q =4899 is about 30% lower than the iris loaded case, due to the increased surface magnetic fields. However, the acceleration efficiency measured by r/Q is also improved by 30% and $E_s/E_a \approx 1$. Figure 5.8 shows the contour plot and surface plot of electric field distribution in the hybrid structure given in Table 5.2. It shows that the peak surface electric field is reduced to the same magnitude as the peak axial electric field. Therefore, hybrid dielectric-iris-loaded structures reduce the peak surface electric field with comparable r/Q as the iris-loaded structures. However, one should notice that the contact between the irises and the dielectric must be as close as possible. One might expect that if there is a large gap existing between a metallic iris and dielectric resulting from fabrication, and then the electric fields on the irises could be enhanced. From qualitative analysis, the surface electric field at the iris will go up, as the gap increases. Detail study of this effect should be investigated in the future, and also other engineering issues should be addressed.

Table 5.2 11.424GHz Hybrid Dielectric-iris-loaded Traveling-wave Structures (e=6, t=1.0 mm)

a (mm)	b (mm)	h (mm)	d (mm)	E_s/E_a	r (MΩ/m)	Q	r/Q (Ω/m)	v_g (c)
5.5	6.923	4.0	8.7535	1.1	38.0	4506.0	8433.2	0.089
4.0	5.361	2.0	8.7535	1.01	66.8	4899.0	13635.4	0.087

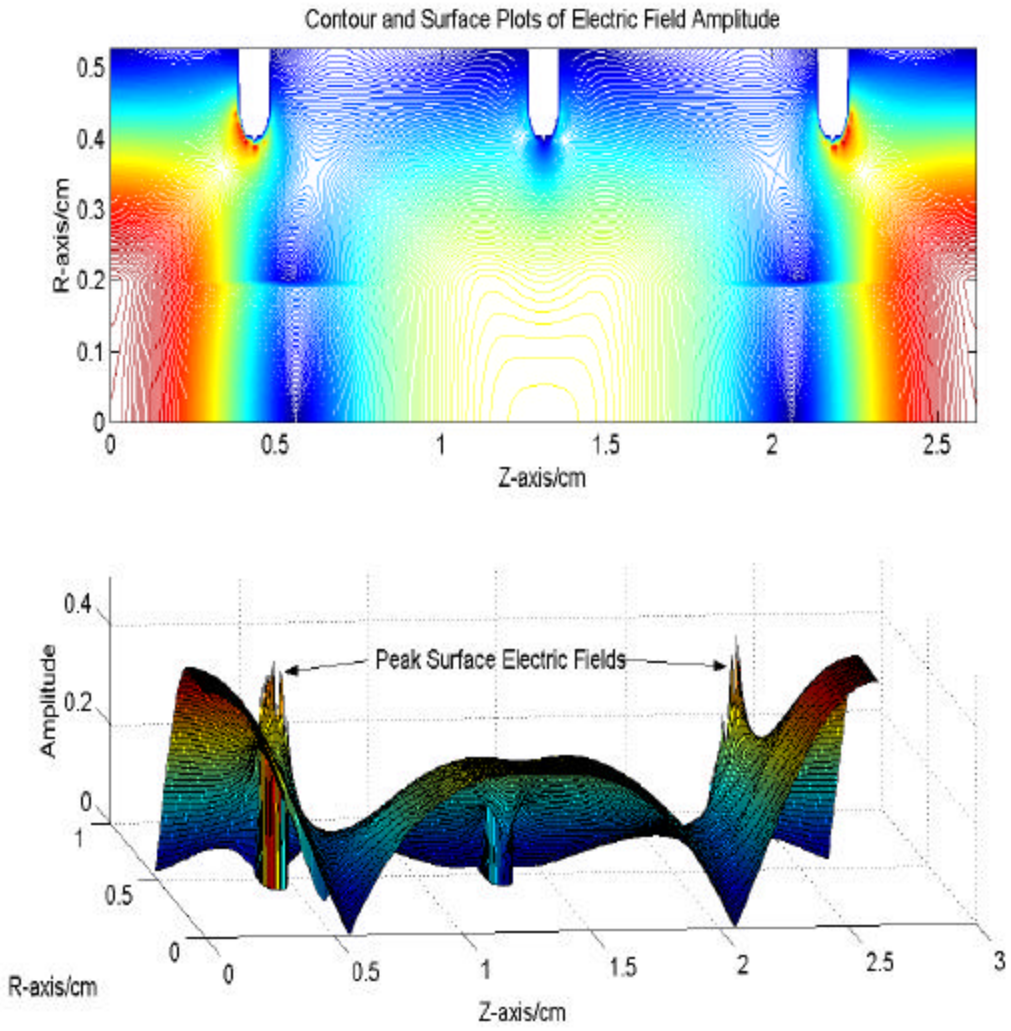

Figure 5.8 Contour and Surface Plots Showing the Distribution of the Electric Field Amplitude in a Hybrid Dielectric-iris-loaded Traveling-wave Structure. The parameters of this structure are given in Figure 5.3. In both plots, the dark red indicates the strongest field amplitude. We can see the strongest electric field on the iris surface is about the same as the axial electric field in this case: E_s/E_a is about 1.01.

Although we could lower the E_s/E_a by introducing dielectric loading into the structure, we have to encounter another unknown problem: dielectric breakdown under high frequency RF fields. The dielectric breakdown limit becomes the constraint of the maximum achievable accelerating gradient instead of the surface breakdown limit of copper in pure iris-loaded structures. Dielectric breakdown at various frequencies has been studied in wakefield acceleration experiments [90], and showed no sign of breakdown up to 20 MV/m at 15 GHz. Besides dielectric breakdown limit, other mostly unknown factors, such as Joule heating and vacuum properties of dielectric loaded structures under high RF power, should also be weighed in to evaluate this type of hybrid dielectric-iris-loaded structure. With a recently proposed experiment [15], breakdown phenomena can be explored at 50 - 70 MV/m field strengths, approaching the NLC desired gradient. Moreover, Joule heating and vacuum properties will also be investigated. If dielectrics can maintain these field gradients, then the scheme we analyzed in the paper would provide an alternate approach that lowers the peak field on the iris by more than a factor of two. This may be an important factor for realizing accelerating structures for very high gradient accelerators.

Figure 5.9 shows the contour plot and surface plot of electric field distribution of the first hybrid structure given in Table 5.2. In this case, the shunt impedance per unit is a little smaller and E_s/E_a is about 1.1. The reason to investigate the case with a larger beam hole is that the beam dynamics puts constraints to choose the beam hole size. This calculation shows that a hybrid structure is capable of simultaneously satisfying the requirements on E_s/E_a and beam stability. Nevertheless, this is hard to be achieved in a conventional iris-

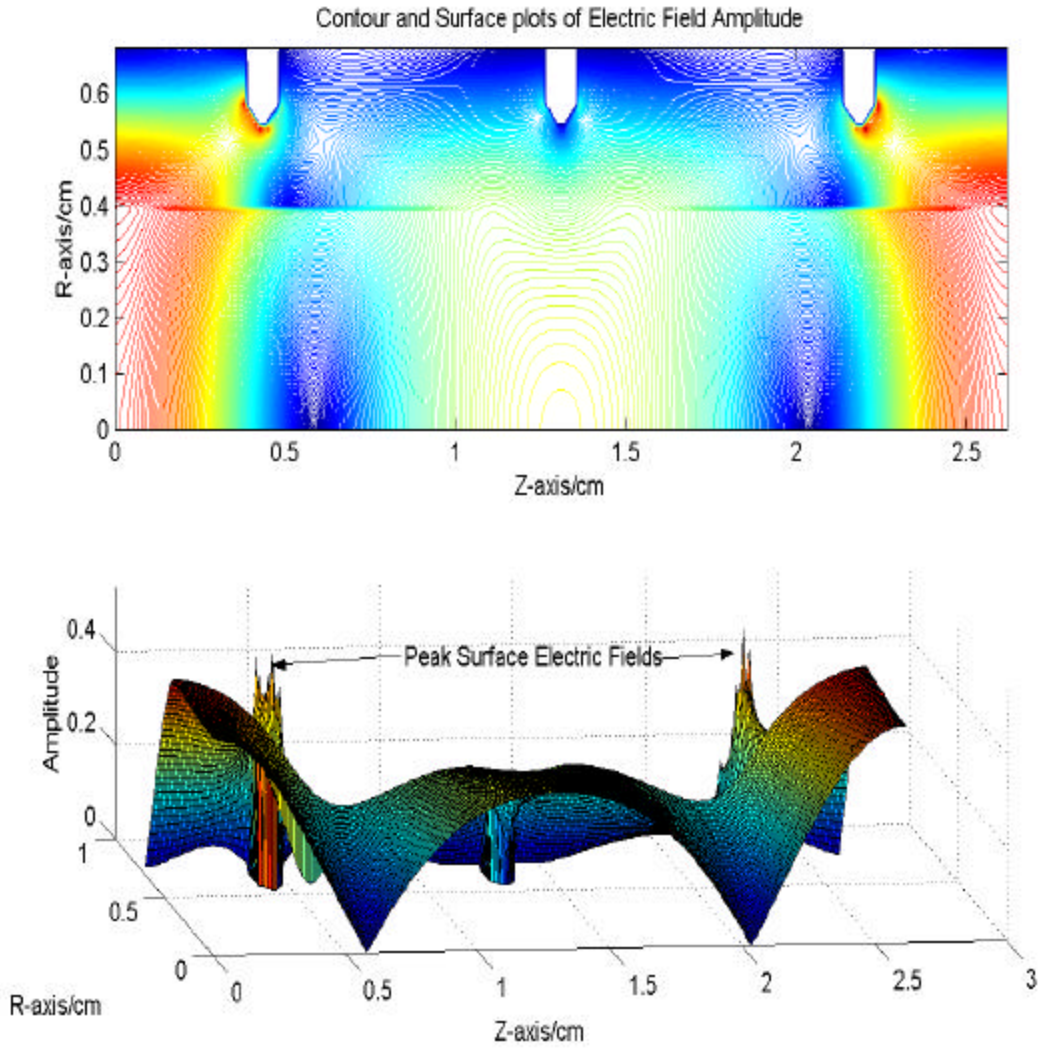

Figure 5.9 Contour and Surface Plots Showing the Distribution of the Electric Field Amplitude in a Hybrid Dielectric-iris-loaded Traveling-wave Structure. The parameters of this structure are given in the first case of Table 2.2. In both plots, the dark red indicates the strongest field amplitude. We can see the strongest electric field on the iris surface is about the same as the axial electric field in this case: E_s/E_a is about 1.1.

loaded accelerating structure, because the iris radius is the only variable to determine such two conflicting parameters.

The variation of shunt impedance per unit length r, r/Q and the quality factor Q as the functions of the beam hole radius are shown in Figure 5.10. For fixed iris radius and dielectric constant, a smaller beam hole radius is preferred for achieving higher acceleration efficiency and less power dissipation on the wall.

The overall optimization of the parameters is complicated because we have to consider three variables: e, a and b. The iris thickness, t, and the beam aperture radius are assumed fixed for the following calculation. The beam aperture radius was chosen as $0.15l$ or 4 mm. Figure 5.11 shows iris radius versus group velocity for several dielectric constants. The results indicate the group velocity is mostly determined by the size of iris, not ε. Figure 5.12 and 5.13 show r and Q as a function of a and e. A higher dielectric constant e gives a lower quality factor Q. Therefore, the optimal e for this structure is in the range of 4 to 6.

The variation of the ratio of the peak surface electric field to the peak accelerating gradient in these cases is shown in Figure 5.14. As shown, a high e can reduce the ratio E_s/E_a significantly as expected. The r/Q plots are given in Figure 5.15. If the dielectric constant is chosen between 4 and 6 for the given geometric parameters, r/Q can be maintained at relatively high constant value.

The analysis of hybrid dielectric-loaded periodic accelerating structures shows that the peak surface electric field can be reduced to levels comparable to the axial accelerating

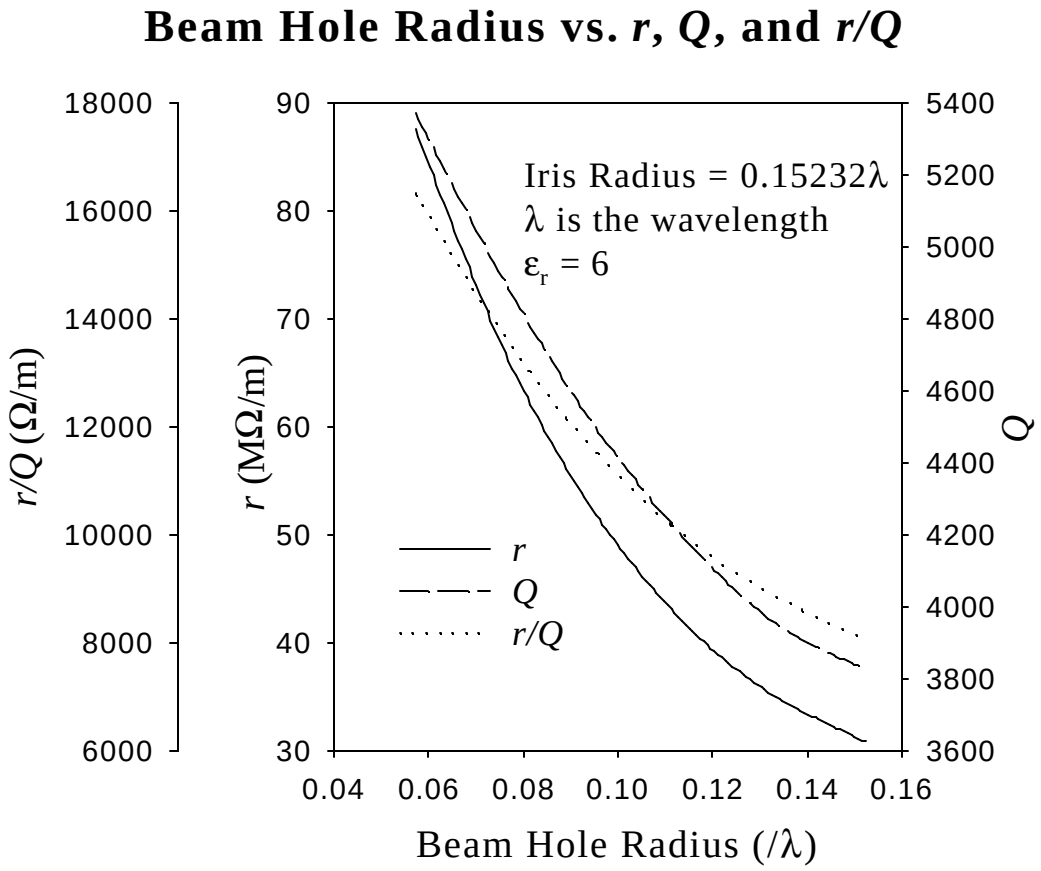

Figure 5.10 Shunt Impedance, the Ratio *r/Q*, and the Quality Factor of a Hybrid Dielectric-iris-loaded Structure as Functions of the Beam Aperture Radius *h*. Device geometry is the same as in Figure 5.6.

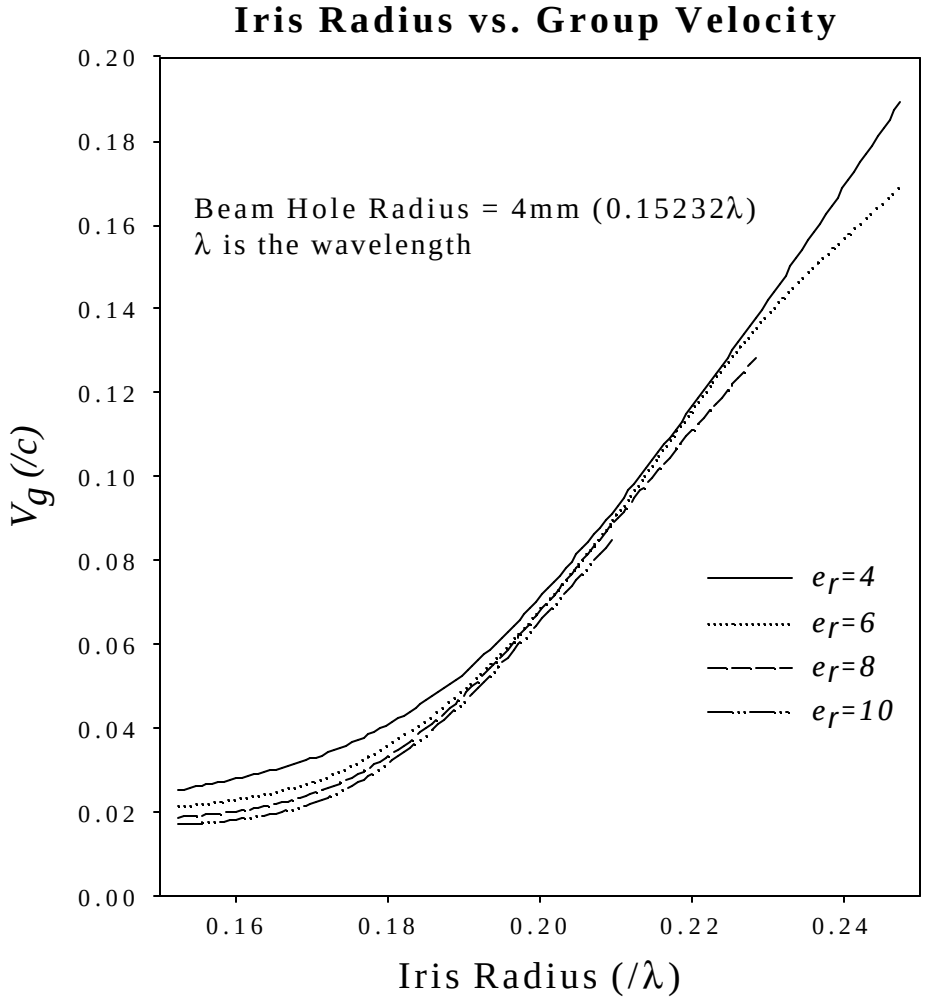

Figure 5.11 Iris Radius a vs. the Group Velocity v_g of the $2\pi/3$ Mode in the Hybrid Dielectric-iris-loaded Structure, When the Beam Aperture Radius h is Fixed as 4.0 mm, and the Wavelength λ is 26.2605 mm. Varying the dielectric constant of the loading ceramics e and iris radius a, the outer radius b is adjusted accordingly to have the phase velocity of TM_{01} mode synchronized with the speed of light c.

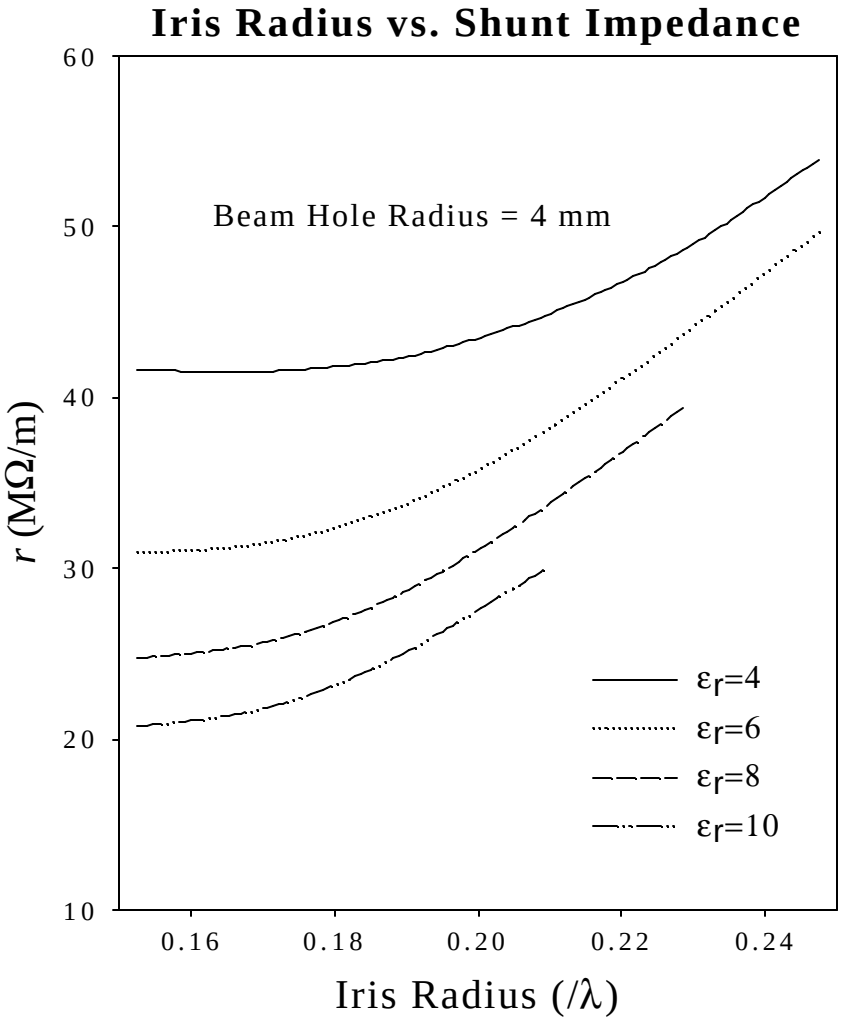

Figure 5.12 The Shunt Impedance Per Unit Length r of the $2\pi/3$ Luminal Mode in a Hybrid Dielectric-iris-loaded Structure as a Function of the Iris Radius a and the Dielectric Constant e. In this case, the beam hole radius h is fixed as 4.0 mm, and the wavelength λ is 26.2605 mm.

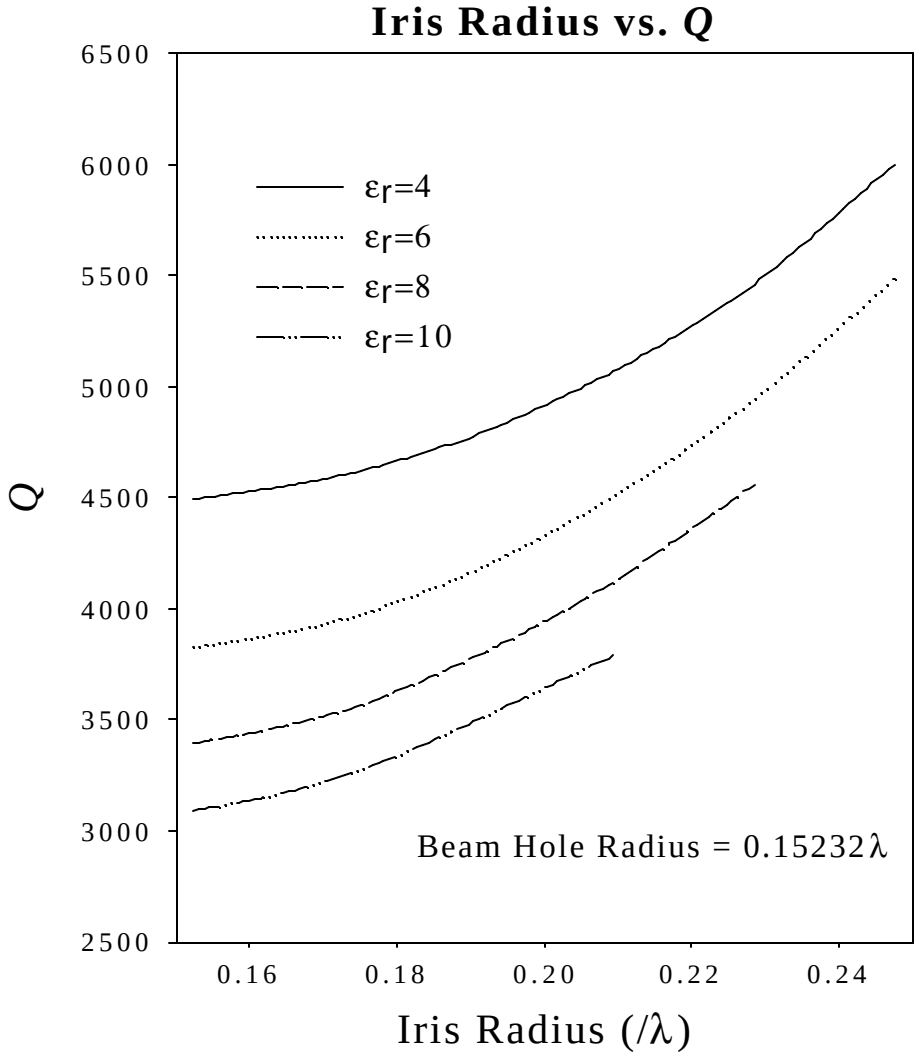

Figure 5.13 The Quality Factor *Q* of the $2\pi/3$ Luminal Mode as a Function of the Iris Radius *a* and the Dielectric Constant *e* in the Hybrid Dielectric-iris-loaded Structure. In this case, the beam aperture radius *h* is fixed as 4.0 mm, and the wavelength λ is 26.2605 mm.

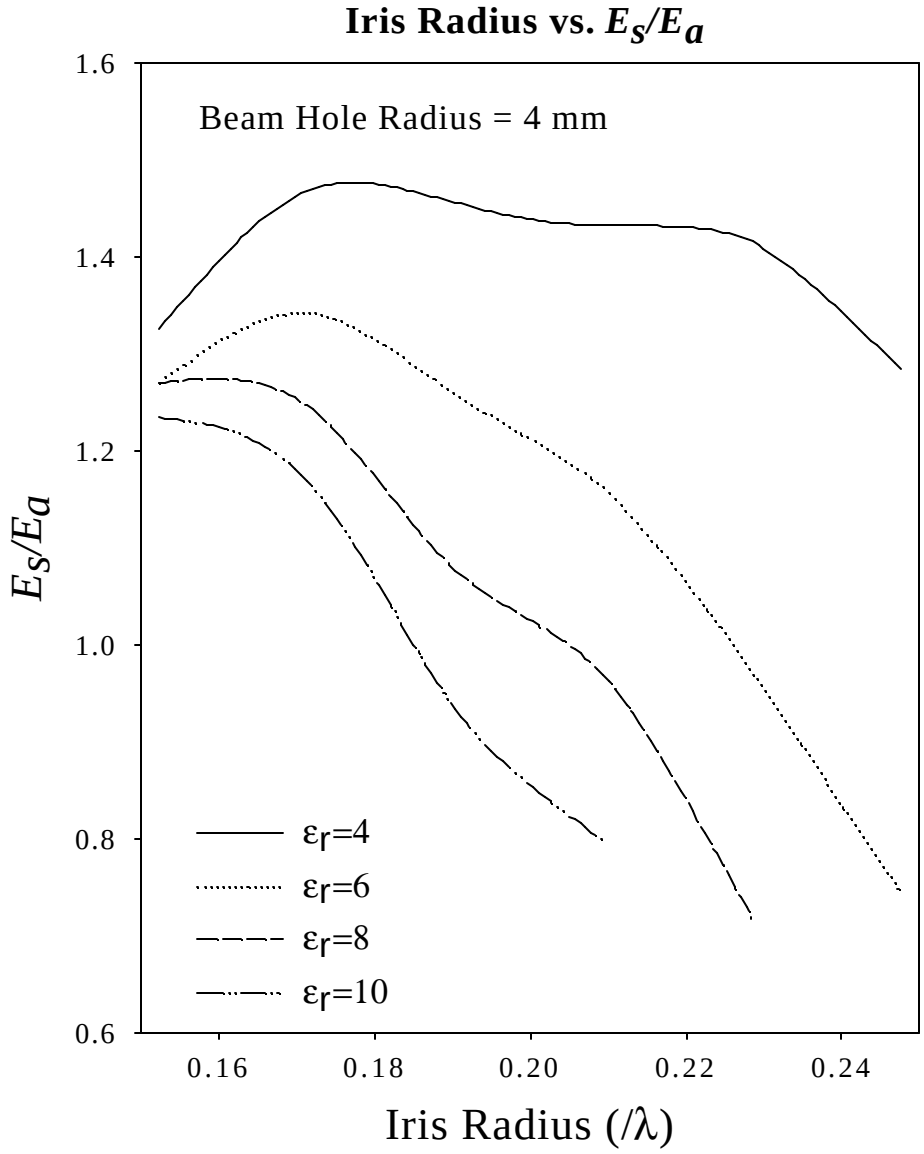

Figure 5.14 The ratio E_s/E_a of the Luminal $2\pi/3$ Mode as a Function of the Iris Radius a and the Dielectric Constant e in the Hybrid Dielectric-iris-loaded Structure. All other structure parameters are the same as in previous figures.

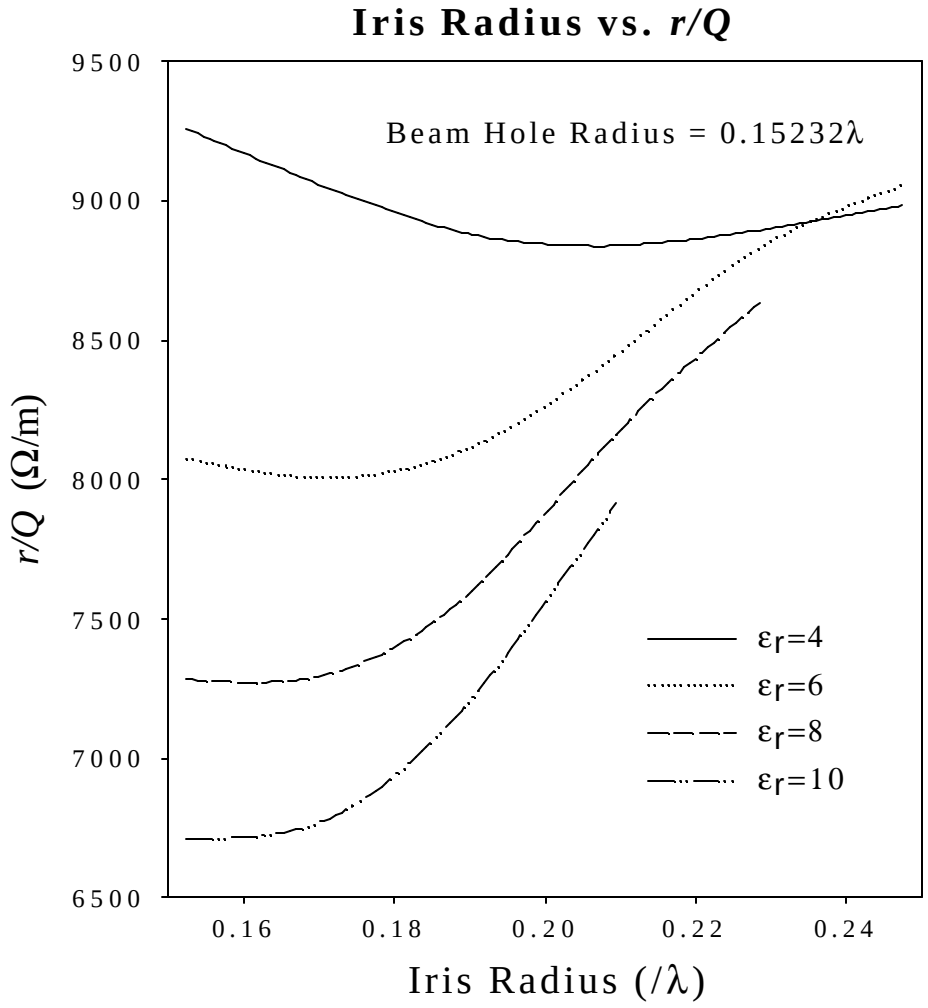

Figure 5.15 The ratio *r/Q* of the 2π/3 Mode as a Function of the Iris Radius *a* and the Dielectric Constant *e* in the Hybrid Dielectric-iris-loaded Structure

field gradient, while the acceleration efficiency measures, such as *r*, *r/Q* and *Q*, are comparable to conventional iris-loaded accelerating structures. Therefore, such hybrid dielectric-iris-loaded structures can significantly increase the upper limit of the accelerating gradient. Such improvement of the ratio E_s/E_a is achieved at the expense of more power dissipation.

If the designed E_a is large, the total length of the designed accelerator can be small. Thus it will lead to a lower capital cost that scales in proportion to the length of the accelerator [91]. At the same time, E_a cannot be too large, since it will push the RF power costs too high. However, in the development of NLC structures, the problem is that the expected E_a is too large for reliable operation for the available RF power [11]. Using the proposed hybrid dielectric-iris-loaded accelerating structure, we may be able to achieve the desired accelerating gradient of NLC structures, with the current available RF sources. Because the peak surface electric field is significantly reduced, higher accelerating gradient may be achieved.

The analysis of hybrid dielectric-loaded periodic accelerating structures shows that the peak surface electric field can be reduced to levels comparable to the axial accelerating field gradient. However, this scheme also reduces the acceleration efficiency measures such as r and *Q*, although *r/Q* can be comparable to conventional iris-loaded structures. Although the numerical examples of X-band structures are only presented here, we expect that this scheme of reducing ratio of E_s to E_a in a conventional iris-loaded structure at any frequency band can be used by employing partially loaded dielectrics. The fundamental issues about using dielectric loaded structure for particle acceleration, such as dielectric

breakdown, Joule heating and vacuum property, determine if hybrid dielectric-iris-loaded periodic structures can be the alternatives for future linear collider acceleration structures. The experimental investigations on these issues are underway, and the advancement in material science also makes this class of structures very promising.

CHAPTER VI

CONCLUSIONS

The advancement of affordable high gradient accelerator technology is essential to the realization of the next-generation linear collider with a center-of-mass energy of 0.5 TeV. To achieve this energy under feasible construction cost, several widely different designs have been proposed for the main accelerator, ranging from a 1.3-GHz superconducting linac to a 30-GHz two-beam accelerator. Within the ongoing R&D projects in Japan, Europe, and the United States, the TESLA and the 11.4-GHz NLC/JLC design are currently among the strongest contenders. However, the future success of TESLA will be highly dependent on the advancement of the technology of superconducting cavity, which is by far immature. The cost is also one of the key constraints that determine the feasibility of such design. The NLC/JLC structures have not reached the desired acceleration gradient without arcing damages caused by the strong surface electric field that is an intrinsic characteristic of pure iris-loaded accelerating structures. Moreover, the fabrication cost of such X-band structures has not been reduced to a considerable level. Because the ongoing major designs have not demonstrated the necessary breakthrough toward the final realization of a next-generation linear collider for more than a decade, new approaches should be looked into. Therefore, dielectric based accelerating structures have been recognized as possible alternatives for the major designs that were described in Chapter 1.

The advantages of dielectric loaded accelerating structures are very attractive. The thorough studies of two classes of dielectric loaded structures described in this thesis show that the accelerator parameters of them are comparable, or even better in some aspects, with

those of conventional iris-loaded accelerator. Structures based on dielectric-lined circular waveguides are capable of achieving higher shunt impedance that merits the acceleration efficiency than iris-loaded structures, but it is at the expense of a lower quality factor. The hybrid dielectric-iris-loaded accelerating structure discussed in Chapter 5 demonstrates a possible way to combine advantages of dielectric-loaded structures and metallic iris-loaded structures. The most significant advantage of such structure is the capability of lowering the peak surface electric field without diminishing the acceleration efficiency. Although it is not at all certain that this approach will be the eventual choice to solve the breakdown problem of the NLC/JLC structures, it provides one possible solution.

However, the fundamental concerns about using dielectric loaded structures in particle acceleration have not been answered. Dielectric breakdown limit is the first of them. Because the electric breakdown of the conducting wall is not a constraint in a dielectric loaded accelerating structure, the maximum achievable accelerating gradient may be limited by the dielectric breakdown. Joule heating of dielectric loaded structure under high power RF power pulses is also an unknown factor. High RF power experiments are necessary to investigate these issues. An externally powered X-band dielectric loaded accelerating structure was designed and realized to conduct such high power testing. The planned experiments will eventually answer the fundamental questions.

The implementation of the dielectric-loaded accelerator prototype produced a crucial technique to achieve the efficient wave coupling that was a big hurdle for realizing dielectric based accelerators such as the AWA step-up transformer accelerator. The calculations of such coupling structure can be improved by specially designed

electromagnetic field solving code based on the FDTD method. Partially filled high-dielectric-constant material and tapered geometry caused the errors in the results obtained with commercial field solving codes such as MAFIA. It is important to study the coupling structure in the further studies, because it can in-depth reveal the mode excitation of such coupling method, and it is useful to the design of similar dielectric loaded accelerators.

One disadvantage of a dielectric-lined circular waveguide based accelerating structure is that it supports multiple propagating waveguide modes at the operating frequency. Mode conversion is consequently one cause of energy losses and induced deflecting modes in such structure, but it has not been discussed. The extent of the effect from this factor in acceleration performance need be studied.

The discussion on the hybrid dielectric-iris-loaded accelerating structure did not include the study of the interaction between particle beams and such structure. The longitudinal and transverse wakefields induced by particle beams traversing the hybrid dielectric-iris-loaded structure must be studied. Such knowledge is necessary in accelerator design in term of beam stability. Furthermore, it may lead to a new wakefield accelerating structure based on such hybrid structure.

The experimental and theoretical studies in this thesis result in useful knowledge in implementing a dielectric-lined circular waveguide based accelerating structure and a novel hybrid dielectric-iris-loaded structure. The high RF power experiment on the testing dielectric accelerating structure may answer the fundamental question as to whether it is feasible to realize a high-energy accelerator.

Considering the history of the evolution of low loss dielectric materials, and the diversity of such materials, it is reasonable to believe that dielectric loaded accelerating structures are the promising candidates for a next-generation linear collider. More importantly, the studies of dielectric loaded accelerating structures provide a new perspective to seek a feasible accelerator technology for next-generation linear colliders.

BIBLIOGRAPHY

[1] Wilson, P.B., "Application of High-Power Microwave Sources to TeV Linear Colliders," Applications of High-Power Microwaves, editors: A.V. Gaponov-grekhov, V.L. Granatstein; Artech House, Boston, Chapter 7, pp. 229-317, 1994.

[2] Wangler, T.P., RF Linear Accelerators, John Wiley & Sons, Inc., Chapter 1, pp. 1-31, 1998.

[3] Gaponov-Grekhov, A.V., Granatstein, V.L., "High-Power Microwave Electronics: A Survey of Achievements and Opportunities," Applications of High-Power Microwaves, editors: A.V. Gaponov-grekhov, V.L. Granatstein; Artech House, Boston, Chapter 1, pp. 1-24, 1994.

[4] Smith, C.L., "The Large Hardon Collider," Scientific American, pp. 71-77, July 2000.

[5] Wyss, C., "The LEP Energy Upgrade Project," 1991 IEEE Particle Accelerator Conference, Conference Record 91 CH3038-7, New York, pp. 150, 1991.

[6] Fry, D.W., "Traveling-wave Linear Accelerator for Electrons," Nature, Vol. 160, 351-353, Sep., 1947.

[7] Seeman, J.T., "The Stanford Linear Collider," Annual Review of Nuclear Particle Science, vol. 41, pp. 389-428, also in SLAC-PUB-5494, SLAC, Stanford, 1991.

[8] Pekeler, M. for the TESLA Collaboration, "Experience with Superconducting Cavity Operation in the TESLA Test Facility," Proceedings of 1999 Particle Accelerator Conference, New York, pp. 245-249, 1999.

[9] Ruth, R.D., Adolphsen, C., Bane, K., Boyce, R.F., Burke, D.L., Callin, R., Caryothkis, G., Cassel, R., Clark, S.L., Deruyter, H., Fant, K., Fuller, R., Heifets, S., Hoag, H., Humphrey, R., Kheifets, S., Koontz, R., Kroll, N.M., Lavine, T., Loew, G. A., Menegat, A., Miller, R.H., Nantista, C., Paterson, J.M., Pearson, C., Phillips, R., Rifkin, J., Spencer, J., Tantawi, S., Thompson, K.A., Vlieks, A., Vylet, V., Wang, J.W., Wilson, P.B., Yeremian, A., and Youngman, B., "The Next Linear Collider Test Accelerator," Proceedings of 1993 Particle Accelerator Conference, Washington, D.C., pp. 543-545, May, 1993.

[10] Urakawa, J., KEK Preprint 93-113, 1993.

[11] Adolphsen, C., Baumgartner, W., Jobe, K., Loewen, R., McCormick, D., Ross, M., Smith, T., and Wang, J.W., "RF Processing of X-Band Accelerator Structures at the NLCTA,", SLAC-PUB-8573, Stanford Linear Accelerator Center, Stanford University, August 2000.

[12] Baconnier, Y., "The CERN Linear Collider Test Facility (CTF)," 1992 Linear Accelerator Conference Proceedings, AECL-28, AECL Research, Chalk River, Ontario, Canada, pp. 329, 1992.

[13] Kilpatrick, W.D., "Criterion for Vacuum Sparking Designed to Include Both RF and DC," Review of Scientific Instruments, vol. 28, No. 10, pp. 824, 1957.

[14] Wangler, T.P., RF Linear Accelerators, John Wiley & Sons, Inc., Chapter 5, pp. 160-161, 1998.

[15] Wang, J.W., "RF Properties of Periodic Accelerating Structures for Linear Colliders," SLAC-Report-339, July, 1989.

[16] Ruth, R.D., Adolphsen, C., Allison, S., Akemoto, M., Atkinson, R., Baumgartner, W., Bong, P., Brown, V., Browne, M., Caryotakis, G., Cassel, R., Cisneros, G., Clark, S.L., Constant, T., Corvin, C., Dean, T., Eichner, J., Fuller, R., Gold, S., Grippe, J., Hanna, S., Hoag, H., Holik, P., Holmes, S., Humphrey, R., Jones, R., Ko, K., Koontz, R., Kroll, N., Lavine, T., Loew, G.A., Loewen, R., Miller, R.H., Nesterov, V., Nantista, C., Paterson, J.M., Pearson, C., Phillips, R., Pierce, W., Pope, R., Porter, T., Rifkin, J., Roster, W., Seidel, M., Smith, H., Smith, S., Spencer, J., Spencer, N., Sprehn, D., Tantawi, S., Thompson, K., Tilghman, A., Vlieks, A., Vylet, V., Wang, J.W., Wilson, P.B., Wilson, Z., Wright, E., Yeremian, D., Zelinski, J., and Zomek, C., "Status and Results from the Next Linear Collider Test Accelerator," SLAC-PUB-7386, Stanford Linear Accelerator Center, Stanford University, California, August 1996.

[17] Katsouleas, T., "Overview of Plasma Accelerators," The Proceedings of Advanced Accelerator Concepts 8th Workshop, AIP Conference Proceedings 472, Baltimore, pp. 19-26, 1998.

[18] Plettner, T., Spencer, J.E., Huang, Y.C., Byer, R.L., Siemann, R.H., and Smith, T.I., "The Laser Driven Particle Accelerator Project: Theory and Experiment," The Proceedings of Advanced Accelerator Concepts 8th Workshop, AIP Conference Proceedings 472, Baltimore, pp. 118-127, 1998.

[19] Zhang B., "Microwave Inverse Cerenkov Accelerator," Proceedings of 7th Advanced Accelerator Concept Workshop, AIP Proceedings No. 398, 1996.

[20] Schoessow, P., "High Gradient Dielectric Wakefield Device Measurements at the Argonne Wakefield Accelerator," Proceedings of 1997 Particle Accelerator Conference, Vancouver, pp. 639-641, May, 1997.

[21] Gai, W., "Performance of the Argonne Wakefield Accelerator Facility and Initial Experimental Results," Proceedings of 7th Advanced Accelerator Concept Workshop, AIP Proceedings No. 398, 1996.

[22] Fang, J., Marshall, T.C., Hirshfield, J.L., LaPointe, M.A., Zhang, T.-B., and Wang, X.J., "An Experimental Test of the Theory of the Stimulated Dielectric Wake-field Accelerator," Proceedings of 1999 Particle Accelerator Conference, New York, pp. 3627-2630, 1999.

[23] Chojnacki, E., "Accelerating Field Step-Up Transformer in Wake-field Accelerators," Proceedings of 1997 Particle Accelerator Conference, Vancouver, pp. 2557-2559, 1997.

[24] Gai, W., Konecny, R., Simpson, J., "Externally Powered Dielectric Loaded Waveguides as Accelerating Structures," Proceedings of 1997 Particle Accelerator Conference, Vancouver, pp. 636-638, 1997.

[25] Zou, P., Gai, W., Konecny, R., Sun, X., Wong, T., and Kanareykin, A., "Construction and Testing of an 11.4 GHz Dielectric Structure Based Traveling Wave Accelerator," Review of Scientific Instruments, vol. **71**, No. **6**, pp. 2301-2304, 2000.

[26] Amiranoff, F., Baton, S., Bernard, D., Cros, B., Descamps, D., Dorchies, F., Jacquet, F., Malka, V., Marquès, J.R., Matthieussent, G., Miné, P., Modena, A, Mora, P., Morillo, J. and Najmudin, Z., "Laser Wakefield Acceleration of Electrons at Ecole Plolytechnique," The Proceedings of Advanced Accelerator Concepts 8th Workshop, AIP Conference Proceedings 472, Baltimore, pp. 303-314, 1998.

[27] Flesher, G., and Cohn, G., "Dielectric Loading for Waveguide Linear Accelerators," AIEE Transactions, 70, pp. 887-893, 1951.

[28] Zhang, T-B., Hirshfield, J., Marshall, T., and Hafizi, B., Physical Review E, **56,** pp. 4647, 1997.

[29] Chjonacki, E., Gai, W., Ho, C., Konecny, R., Mtingwa, S., Norem, J., Rosing, M., Schoessow, P., and Simpson, J., Journal of the Applied Physics, **69**, pp. 6257, 1991.

[30] Gai, W., Ho, C.-H., "Modeling of the Transverse Mode Suppressor for Dielectric Wake-Field Accelerator," Journal of the Applied Physics, Vol. 70, pp. 3955-3957, 1991.

[31] Trans-Tech., Catalog, 5520 Adamstown, Adamstown, MD 21710.

[32] Bolotovskii, B.M., "Theory of Cerenkow Radiation (III)," Soviet Physics Uspekhi, Volume 4, No. 5, pp. 781-782, 1962.

[33] Gai, W., Schoessow, P., Cole, B., Konecny, R., Norem, J., Rosenzweig, J., and Simpson, J., "Experimental Demonstration of WakeField Effects in Dielectric Structures," Physical Review Letters, vol. 61, pp. 2756, 1988.

[34] Conde, M., Gai, W., Konecny, R., Power, J., Schoessow, P., and Zou, P., "RF Power Generation and Coupling Measurements for the Dielectric Wakefield Step-up Transformer," Advanced Accelerator Concepts Eighth Workshop, AIP Conference Proceedings 472, Baltimore, pp. 626-634, 1998.

[35] Power, J.G., Conde, M.E., Gai, W., Konecny, R., Schoessow, P., and Kanareykin, A., "Measurements of Wakefields in a Multimode, Dielectric Wakefield Accelerator Driven by a Train of Electron Bunches," Phyical Review Special Topic: Accelerator and Beam Physics, vol. 3, 2000.

[36] Gai, W., Conde, M., Konecny, R., Power, J. G., Schoessow, P., Sun, X., and Zou, P., "Experimental Demonstration of Dielectric Structure Based Two Beam Acceleration," Proceedings of Advanced Accelerator Concepts 9th Workshop, Santa Fe, NM, June 2000.

[37] Conde, M.E., Gai, W., Konecny, R., Power, J. G., Schoessow, P., and Sun, X., "A High-Charge High Brightness L-Band Photocathode RF Gun," The Proceedings of the ICFA Advanced Accelerator Workshop, Los Angeles, November 1999.

[38] Wilson, P.B., RF-Driver Linear Colliders, Proceedings of 1987 IEEE Particle Accelerator Conference, Washington, D.C, pp. 53-58, 1987.

[39] Wang, J.W., Adolphsen, C., Bane, K.L., Bowden, G.B., Burke, D.L., Deruyter, H., Cornuelle, J., Farkas, Z.D., Fowkes, W.B., Hanna, S., Hoag, H.A., Irwin, J., Jones, R.M., Ko, K., Kroll, N., Li, Z., Loew, G.A., Loewen, R.J., Miller, R.H., Ng, C.K., Paterson, J.M., Pearson, C., Raubenhemer, T.O., Rifkin, J., Ruth, R.D., Tantawi, S.G., Thompson, K.A., Vaillancourt, K.W., Vlieks, A.E., Wilson, P.B., Asano, K., Funahashi, Y., Higashi, Y., Higo, T., N. Hitomi, Suzuki, T., Takata, K., Takatomi, T., Toge, N., Watanabe, Y., Elmer, J., Klingmann, J., Mugge, M., Van, K., "Accelerator Structure R&D for Linear Colliders," Proceedings of 1999 Particle Accelerator Conference, New York, pp. 3423-3425, 1999.

[40] Dehler, M., Jones, R.M., Kroll, N.M., Miller, R.H., Wilson, I., and Wuensch, W., "Design of A 30 GHz Damped Detuned Accelerating Structure," Proceedings of the 1997 IEEE Particle Accelerator Conference, Vancouver, pp. 518-520, 1997.

[41] MAFIA Version 4.0 User's Manual, Gesellschaft fur Computer-Simulationstechnik, Lauteschlagerstrabe 38, D-64289, Darmstadt, Germany.

[42] Loew, G.A., and Neal, R.B., Linear Accelerators, Chapters B.1.1 and B.1.4, North-Holland Publishing Co., 1970

[43] Garyotakis, G., Callin, R., Eppley, K., Lee, T., Fant, K., Fowkes, R., Hoag, H., Pearson, C., Phillips, R., Tantawi, S., Vlieks, A., Wright, E., Lien, E., and Miram, G., "Development of Multimegawatt Klystrons for Linear Colliders," . Proceedings of 1993 Particle Accelerator Conference, Washington, D. C., pp. 1106-1108, May, 1993.

[44] Ng, K.-Y., "Wake Fields in a Dielectric-lined Waveguide," Physical Review D, pp. 1819-1828, 1990.

[45] Rosing, M., and Gai, W., "Longitudinal- and Transverse-wake-field Effects in Dielectric Structures," Physical Review D, pp. 1829-1834, 1990.

[46] Wangler, T.P., RF Linear Accelerators, John Wiley & Sons, Inc., Chapter 11, pp. 314-353, 1998.

[47] Tang, C.C.H., "Mode Conversion in Tapered Waveguides At and Near Cutoff," IEEE Transactions on Microwave Theory and Techniques 14, pp. 233-239, 1966.

[48] Unger, H.-G., "Circular Waveguide Taper of Improved Design," Bell System Technical Journal 37, pp. 899-912, 1958.

[49] Tang, C.C.H., "On the Wave Propagation and Mode Coversion in a Helically Corrugated Multimode Circular Waveguide," IEEE Transactions on Microwave Theory and Techniques 14, pp. 275-285, 1966.

[50] Albersheim, W.J., "Propagation of TE_{01} Waves in Curved Wave Guides," The Bell System Technical Journal, vol. 28, pp. 1-30, January 1940.

[51] Wangler, T.P., RF Linear Accelerators, John Wiley & Sons, Inc., Chapter 3, pp. 57-86, 1998.

[52] MathCAD User's Guide, MathSoft, Inc., Cambridge, Massachusetts, 2000.

[53] Matthaei, G., Young, L., Jones, E.M.T., Microwave Filters, Impedance-Matching Networks, and Coupling Structures, Chapter 5, Artech House, 1990

[54] Gold., S., Private Communications, 2001.

[55] Nezhevenko, O.A., Yakovlev, V.P., Hirshfield, J.L., Kozyrev, E.V., Gold, S.H., Fliflet, A.W., Kinkead, A.K., True, R.B., and Hansen, R.J., "X-Band Magnicon Amplifier," Proceedings of 1999 Particle Accelerator Conference, New York, pp. 1049-1051, 1999.

[56] Bethe, H.A., "Lumped Constants for Small Irises," Report 43-22, MIT Radiation Laboratory, Cambridge, Massachusetts, 1943.

[57] Bethe, H.A., "Theory of Side Windows in Waveguide," Report 43-27, MIT Radiation Laboratory, Cambridge, Massachusetts, 1943.

[58] Bethe, H.A., "Formal Theory of Wave Guides of Arbitrary Cross Section," Report 45-26, MIT Radiation Laboratory, Massachusetts, 1943.

[59] Collin, R.E., Field Theory of Guided Waves, McGraw-Hill Book Company, Chapter 7, 1960.

[60] Cohn, S.B., "Microwave Coupling by Large Apertures," Proceedings of IRE, vol. 40, pp. 696-699, June 1952.

[61] Cohn, S.B., "Determination of Aperture Parameters by Electrolytic Tank measurements," Proceedings of IRE, Vol. 39, pp. 1416-1421, November 1951.

[62] Gluckstern, R.L., Li, R., and Cooper, R.K., "Electric Polarizability and Magnetic Susceptibility of Small Holes in a Thin Screen," IEEE Transactions on Microwave Theory and Techniques, vol. 38, No. 2, pp. 186-191, 1990.

[63] Lee, K.S.H., Comments on "Electric Polarizability and Magnetic Susceptibility of Small Holes in a Thin Screen", IEEE Transactions on Microwave Theory and Techniques, vol. 38, No. 10, 1529, 1990.

[64] Gluckstern, R. L., Li, R. and Cooper R.K., Corrections to "Electric Polarizability and Magnetic Susceptibility of Small Holes in a Thin Screen", IEEE Transactions on Microwave Theory and Techniques, vol. 38, No. 10, pp. 1529, 1990.

[65] Gupta, S., Chakrabarty, A., and Das, B.N., "Admittance of Waveguide Feed Slot Radiators," Antennas and Propagation Society International Symposium, 1989, AP-S. Digest, vol. 2, pp. 968-971, 1989.

[66] Datta, A., Chakraborty, A., and Das, B.N., "Analysis of a Strip Loaded Resonant Longitudinal Slot in the Broad Wall of a Rectangular Waveguide," IEE Proceedings H, vol. 140, No. 2, pp. 135-140, 1993.

[67] Datta, A., Das, B.N., and Chakraborty, A., "Moment Method Formulation of Thick Diaphragms in a Rectangular Waveguide," IEEE Transactions on Microwave Theory and Techniques, vol. 40, No. 3, pp. 592-595, 1992.

[68] Das, B.N., Somasekhar Rao, P.V.D., and Chakraborty, A., "Narrow Wall Axial-Slot-Coupled T Junction between Rectangular and Circular Waveguides," IEEE Transactions on Microwave Theory and Techniques, vol. 37, No. 10, pp. 1590-1596, 1989.

[69] Das, B. N., and Somasekhar Rao, P.V.D, "Moment Method Analysis of a Slot Coupled Junction between Dissimilar Rectangular Waveguides," IEE Proceedings H, vol. 137, No. 6, pp. 406-410, 1990.

[70] Das, B.N., Somasekhar Rao, P.V.D, "Analysis of a Transition between Rectangular and Circular Waveguides," IEEE Transactions on Microwave Theory and Techniques, vol. 39, No. 2, pp. 357-359, 1991.

[71] Sharma, S.B., Chakrabarty, S.B., and Das, B.N., "Analysis of a Slot-Coupled T-junction between Circular-to-Rectangular waveguide," IEEE Transactions on Microwave Theory and Techniques, vol. 46, No. 8, pp. 1173-1176, 1998.

[72] Harrington, R. G., Field Computation by Moment Method, McGraw-Hill Co., New York, 1968.

[73] Yee, K. S., "Numerical solution of initial boundary value problems involving Maxwell's equations in isotropic media," IEEE Trans. Antennas Propagation, vol. AP-14, pp. 302-307, May 1966.

[74] MAFIA Manual Version 3.2, Gesellschaft fur Computer-Simulationstechnik, Lauteschlagerstrabe 38, D-64289, Darmstadt, Germany.

[75] Peterson, A.F., Ray, S.L., and Mittra, R., Computational Methods for Electromagnetics, IEEE Press, New York, Chapter 12, 1998.

[76] Fang, J., Time Domain Finite Difference Computation for Maxwell's Equations, Ph.D. Dissertation, University of California at Berkeley, 1989.

[77] Holland, R., "Finite difference solutions of Maxwell's equations in generalized nonorthogonal coordinates," IEEE Transactions on Nuclear Science, vol. NS-30, pp. 4589-4591, December 1983.

[78] Jones, M., "Electromagnetic PIC codes with body-fitted coordinates," Proceedings of the 12th Conference on the Numerical Simulation of Plasmas, American Physical Society, Topical Group on Computational Physics, San Francisco, CA, Sept. 1987.

[79] Fusco, M., "FDTD algorithm in curvilinear coordinates," IEEE Transactions on Antennas Propagation, vol. AP-38, pp. 76-89, Jan. 1990.

[80] Madsen, N., and Ziolkowski, R.W., "A three-dimensional modified finite volume technique for Maxwell's equations," Electromagnetics, vol. 10, pp. 147-161, 1990.

[81] Madsen, N., "Divergence preserving discrete surface integral methods for Maxwell's curl equations using non-orthogonal unstructured grids," Journal of Computational Physics, vol. 119, pp. 34-45, 1995.

[82] Kunz, K.S., and Simpson, L., "A technique for increasing the resolution of finite-difference solutions of the Maxwell equations," IEEE Transactions on Electromagnetic Computation, vol. EMC-23, pp. 419-422, April 1981.

[83] Zivanovic, S.S., Yee, K.S., and Mei, K.K., "A subgridding algorithm for the time-domain finite-difference method to solve Maxwell's equations," IEEE Transactions on Microwave Theory and Techniques, vol. MTT-38, pp. 471-479, Mar. 1991.

[84] Loewen, R.J., Menegat, A., Vlieks, A.E., Wang, J.W., and Higo, T., "SLAC High Gradient Testing of a KEK X-Band Accelerator Structure," Proceedings of 1999 Particle Accelerator Conference, New York, pp. 3420-3422, 1999.

[85] The Los Alamos Accelerator Code Group, Reference Manual for the Poisson/Superfish, LA-UR-87-126, 1987.

[86] Loew, G.A., Miller, R.H., Early, R.A., and Bane, K. L., "Computer Calculations of Traveling-wave Periodic Structure Properties," IEEE Transactions on Nuclear Science, Vol. NS-26, No. **3**, pp. 3701-3704, 1979.

[87] Wangler, T.P., RF Linear Accelerators, John Wiley & Sons, Inc., Chapter 2, pp. 35-53, 1998.

[88] Panofsky, W.K.H., "Linear Accelerator Beam Dynamics," University of California Radiation Laboratory Report UCRL-1216, University of California, Berkeley, 1951.

[89] Miller, R.H., "Comparison of Standing-wave and Traveling-wave Structrues," SLAC-PUB-3935, Stanford Linear Accelerator Center, Stanford University, California, April 1986.

[90] Schoessow, P., Conde, M.E., Gai, W., Konecny, R., Power, J., and Simpson, J., "High Power Radio Frequency Generation by Relativistic Beams in Dielectric Structures," Journal of Applied Physics, vol. 84, no. 2, pp. 663-667, July 1998.

[91] Loew, G.A., "Linear Collider Systems and Costs," Proceedings of 1993 Particle Accelerator Conference, Washington, D.C., pp. 644-646, 1993.